ISSN 1349-6832

JEOL news

July2006 Vol.41 No.1

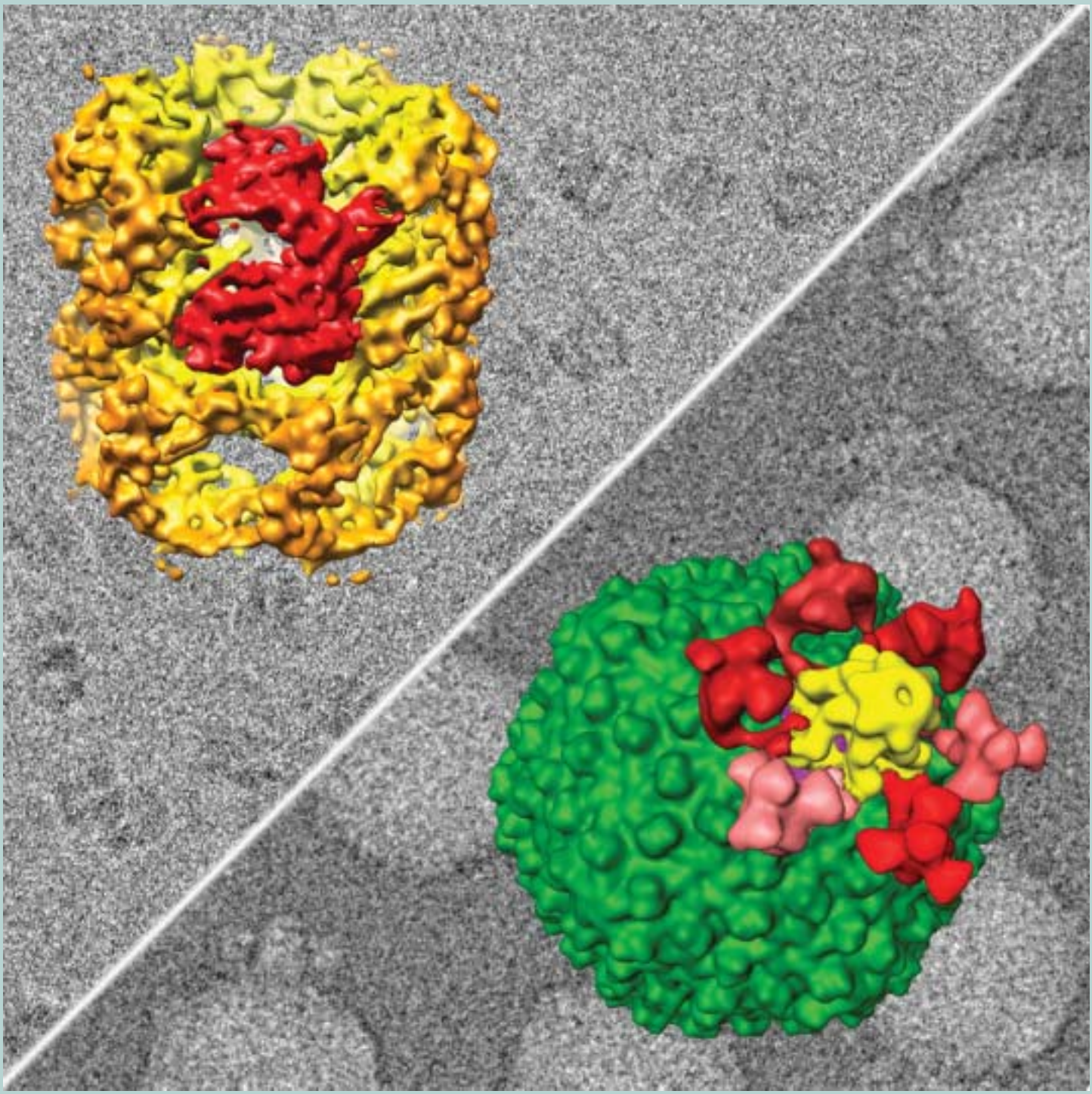

JEOL news

Volume 41 Number 1
July, 2006

Contents

Cover micrograph

3D structures of biological nano-machines including GroEL, a bacterial protein folding machine (left) and epsilon 15 bacteriophage (right) reconstructed by combining low dose electron images (background) of these nano-machines embedded in vitreous ice at different orientational views.
The images were recorded on a Gatan 4k × 4k CCD camera in a JEOL JEM-2010F electron cryomicroscope operated at a specimen temperature of -180°C. The red color in the GroEL photo annotates a single protein subunit in this 14mer nano-machine. Different colors in the epsilon 15 bacteriophage denote different proteins and DNA in a cut-away view to highlight the region for viral genome insertion and ejection.

The Aberration Corrected JEOL JEM-2200FS FEG-STEM/TEM Fitted with an Ω Electron Energy-Filter: Performance Characterization and Selected Applications

M. Watanabe†, D. W. Ackland†, C. J. Kiely†, D. B. Williams†, M. Kanno††, R. Hynes†† and H. Sawada†††

† Department of Materials Science and Engineering / Center for Advanced Materials and Nanotechnology, Lehigh University
†† JEOL USA.
††† JEOL Ltd.

A newly developed JEM-2200FS scanning transmission electron microscope (STEM) / transmission electron microscope (TEM) integrated with a CEOS aberration-corrector and an in-column Ω-filter has recently been installed at Lehigh University. For this instrument, all the microscope parameters, including room environment, have been optimized in order to achieve the best resolution in a STEM imaging mode while simultaneously allowing efficient analytical capabilities by electron energy-loss spectrometry (EELS). The STEM and TEM performances of the Lehigh JEM-2200FS are presented in this report as well as some initial results of atomic-column STEM-EELS analysis obtained from a Ni-base intermetallic alloy.

Introduction

The identification and quantification of the nature of individual atomic configurations are among the ultimate goals for the characterization of nano-structured materials. It is now possible to perform such advanced characterization in a scanning transmission electron microscope (STEM) equipped with a recently developed aberration corrector using electron energy-loss spectrometry (EELS) and X-ray energy dispersive spectrometry (XEDS). The primary improvement due to the aberration corrector is a significant reduction of the effects of spherical aberration, which has been one of the major limiting factors of electron lenses since the original development of transmission electron microscopes (TEMs). By employing aberration correction, the contrast delocalization effect can be significantly minimized for atomic-resolution phase-contrast imaging in static-beam TEM applications [e.g., 1, 2]. In addition, the STEM aberration-corrector can refine the incident probe dimensions significantly. In aberration-corrected STEMs, therefore, the resolution in high-angle annular dark-field (HAADF) imaging can reach sub-Ångstrom levels [3] and materials characterization at the atomic level can routinely be performed by EELS [4]. Additionally, it has also recently been demonstrated that both the spatial resolution and the analytical sensitivity of XEDS analysis can be significantly improved by a use of the aberration-corrected 300 keV dedicated STEM at Lehigh, which is optimized for XEDS analysis [5].

Recently, a state-of-the-art JEOL JEM-2200FS 200 keV STEM/TEM integrated with a CEOS aberration corrector and an in-column Ω energy-filter was installed at Lehigh. This instrument has been set up primarily to perform atomic-resolution HAADF-STEM imaging and simultaneous EELS analysis. In this report, the relevant microscope configurations are briefly described as well as the room modifications required to perform atomic-resolution characterizations on a routine basis. Then, the optimum probe forming parameters required to achieve atomic-scale characterization are theoretically discussed based on detailed probe simulations for the aberration-corrected STEM. Finally, the microscope performances both in the aberration-corrected STEM mode and in the TEM mode obtained in this instrument are demonstrated through some materials characterization studies.

5 E. Packer Ave., Bethlehem, PA 18015, USA.
E-mail: masashi.watanabe@lehigh.edu

The Microscope Configuration

Figure 1 shows the JEM-2200FS 200 keV STEM/TEM installed at Lehigh University. This instrument is equipped with a Schottky

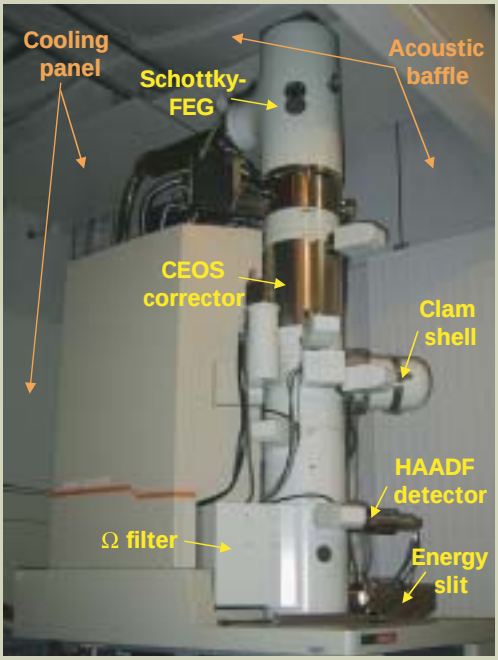

Fig. 1 An image of the JEM-2200FS STEM/TEM at Lehigh University. Installed acoustic baffles and water-cooling panels can also be seen on the ceiling and side walls in the microscope room.

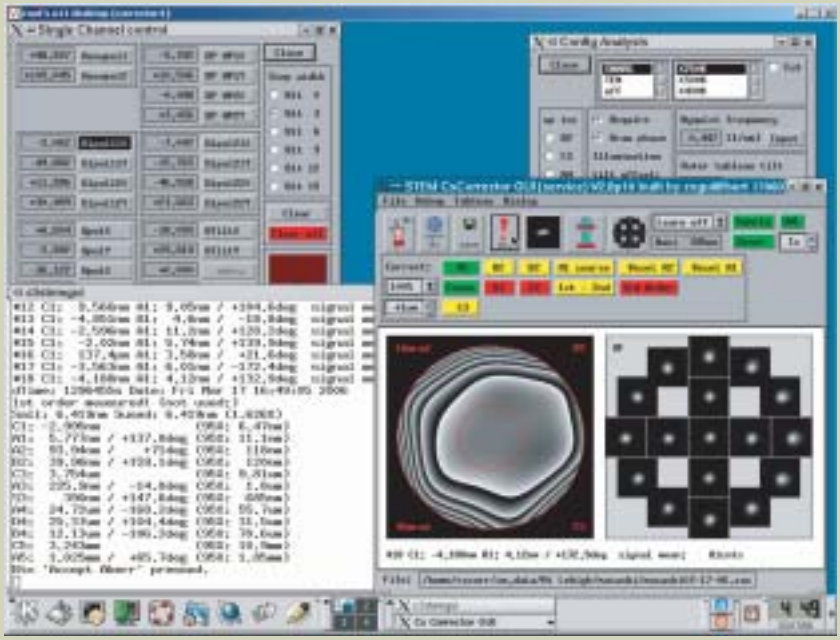

Fig. 2 A screen shot of the CEOS aberration-correction software after Zemlin tableau auto-tuning. The measured aberration coefficients and phase shift image calculated from the tuned results are also displayed.

field-emission gun (FEG) source and an in-column Ω-type electron energy-filter. In addition to the regular TEM functions such as bright/dark-field imaging, electron-diffraction analysis and atomic-resolution phase-contrast imaging, the Ω filter allows acquisition of zero-loss (fully elastic) images and elemental distributions in thin specimens using inelastically scattered electrons. In the previous JEOL Ω-filter microscopes, the illuminated area is significantly shrunk and distorted as the accelerating voltage is increased, which is required to acquire energy-filtering elemental maps. This change in the illuminated area is due to the strong pre-field above the specimen, which in combination with the change in the accelerating voltage made energy-filtering work more difficult. In the JEM-2200FS, however, the illuminated area in the energy-filtering TEM mode remains the same at any energy-loss region as a function of illumination compensation. In practical energy-filtering work, this illumination compensation feature is found to be a highly desirable and effective modification. Furthermore, this instrument is also equipped with a CEOS Cs-corrector in the illumination system (above the objective lens) for probe refinement.

In addition to these major distinct features, many upgrades have been made from previous JEOL Ω-filter instruments. The post-specimen column lens configuration have been modified so as to have as 4 and 2 post-specimen lenses at the pre- and post-Ω-filter positions, respectively. The additional post-specimen lens at the pre Ω-filter position inhibits any image or diffraction-pattern rotation as the magnification or camera length is changed. There is also a HAADF detector above the Ω filter, which makes STEM-EELS acquisition possible in combination with the additional post-specimen lens. This microscope is also equipped with another bright-field (BF) and ADF detectors positioned after all the lenses. In addition to the EELS functions facilitated by the Ω-filter, a Thermoelectron XEDS detector having a collection angle of 0.13 sr is also fitted to this microscope.

Microscope stabilities have also been improved. The specimen holder (which may be the most sensitive to influence by the external environment) is completely isolated by an o-ring sealed “clam shell” after loading into the microscope column. Due to the clam shell, stage drift is significantly reduced. The JEM-2200FS microscope is equipped with active suspensions at the four corners of the instrument base, which act to efficiently reduce high frequency vibrations.

The whole microscope is operated through different 5 computers (namely for (i) the major controls, (ii) STEM operation, (iii) image/EELS acquisition, (iv) XEDS acquisition and (v) aberration correction), which are linked via a local area network. Because all the controls, including apertures and energy-selection slit, can be accessed digitally, the instrument can also be operated remotely with the JEOL Sirius interface. For instance, the microscope has been operated remotely via a regular internet line from NASA Goddard, MD, USA, which is located ~280 km away from Lehigh University.

The Room Construction

To achieve 1 Å or sub-Å resolution in STEM imaging and analysis, the local environment surrounding the microscope needs to be carefully controlled. The key environmental factors that influence microscope performance can be summarized as: (i) stray electromagnetic fields, (ii) air flow, (iii) sudden air pressure changes, (iv) temperature drift and (v) residual noise (e.g. caused by fans in power supply units and computers). Some of these factors are strongly correlated with one another, and hence minimizing these environmental issues are essential requirement for advanced microscopy performance at atomic-column resolution levels. The microscope room for the JEM-2200FS at Lehigh has been modified from its previous configuration based largely on practical suggestions described by Muller and Grazul [6].

In order to reduce the electromagnetic fields, all metal parts such as ceiling grids, pipes, HEPA filters and duct work as well as metal raceways for wiring were removed. The major power supply units for the microscope were isolated in a separate air-conditioned room. All fluorescent lights were replaced with high intensity fluorescent bulbs and discrete sockets were installed for accessory power.

For the reduction of instabilities arising from air flow and air pressure changes, air conditioning filters and ducts were removed and a low-flow duct soc was installed on one of the walls at a distance of more than 3 m from the microscope column. In addition, an air-lock double door was installed and the microscope column has been surrounded with a curtain. The room temperature is controlled by 26 cooling panels mounted on the walls and ceiling as shown in **Fig. 1**. Since water circulated by a conventional chiller is used as coolant for the panels, no direct air flow is created for cooling unlike regular air conditioning. Using the cooling panels, the room temperature can be kept constant at 21°C with a temperature fluctuation of ~0.2°C per hour.

For acoustic noise reduction, water chillers and vacuum pumps were positioned outside of the microscope room and acoustic baffles were installed between the cooling panels and ceiling/side walls as well as at each corner in the

room. In **Fig. 1**, the cooling panels and the acoustic baffles can be clearly seen. Furthermore, fan silencers were mounted on selected power supply units and computers to reduce noise.

Characterization of Aberration-Corrected STEM Performance

CEOS aberration-correction system

The CEOS aberration-corrector for the illumination system is positioned in the column between the condenser and objective lenses as shown in **Fig. 1**. The corrector consists of 2 hexapoles and 2 pairs of transfer lens couples, which can be tuned automatically using the Zemlin tableau method for probe shape analysis. This method involves measuring a series of probe shapes as a function of the tilt angle based on the deconvolution technique between focused and over-/under- focused ADF images [7, 8]. After auto-tuning using the tableau technique, a series of probe shapes at different tilt angles is displayed with the phase shift image being calculated from the measured aberration coefficients up to 5th order (**Fig. 2**). Typical values of the measured aberration coefficients after auto-tuning are also summarized in **Table 1**. Since the JEM-2200FS at Lehigh is equipped with an ultra high resolution pole-piece, the original values of the spherical (C_s) and chromatic (C_c) aberration coefficients, which are the smallest obtainable in current available 200 keV instruments, are shown in Table 1 for comparison. After aberration correction, the C_s value is significantly reduced to ~3.8 µm (1/120 of the original value!) with a 5th-order aberration coefficient (C_5) of only 3.2 mm. Note that the C_c value in the corrected condition is slightly enlarged from the original value due to the presence of the aberration corrector. However, this enlargement in C_c has only a marginal effect on the fine probe formation in a 200 keV FEG instrument.

After the auto-tuning process, lower order aberrations such as the twofold astigmatism (A_1) and 2nd-order axial coma (B_2) can be adjusted manually by observing the Ronchigram (i.e. the defocused shadow image). **Figure 3** shows comparisons of the Ronchigrams obtained from Au nano particles on a thin Ge support film in the hexapole-off (a) and on (b) (i.e. aberration corrected) modes. It should be mentioned that the correction can be defeated by turning the hexapoles off even after corrector tuning. In both Ronchigrams, the intensity distribution becomes uniform at the center. It is usually considered that the lens aberrations no longer influence the incident probe formation within the region of uniform intensity within the Ronchigram. In the uncorrected mode with C_s = 0.5 mm, the uniform intensity area in **Fig. 3(a)** is only 11 mrad wide, and hence a smaller probe-forming aperture (which also limits the available probe current) must be used to avoid the influence of spherical aberration. Conversely, the uniform intensity region in the Ronchigram is expanded to over 34 mrad after corrector auto-tuning followed by the manual adjustments of A_1 and B_2, as shown in **Fig. 3(b)**. The expansion of the uniform intensity area means that a larger probe-form-

Table 1 Summary of aberration coefficients of the JEM-2200FS for (a) conventional and (b) typical aberration-corrected conditions.

(a) conventional condition	
Spherical aberration, C_s = 0.5 mm	Chromatic aberration, C_c = 1.1 mm
(b) aberration-corrected condition	
Twofold astigmatism, A_1 = 5.8 nm	4th-order axial coma, B_4 = 12 µm
2nd-order axial coma, B_2 = 40 nm	4th-order three lobe, D_4 = 25 µm
Threefold astigmatism, A_2= 94 nm	Fivefold astigmatism, A_4 = 25 µm
3rd-order spherical aberration, $C_s(C_3)$ = 3.8 µm	5th-order spherical aberration, C_5 = 3.2 mm
3rd-order star aberration, S_3 = 390 nm	Sixfold astigmatism, A_5= 1 mm
Fourfold astigmatism, A_3 = 226 nm	Chromatic aberration, C_c = 1.4 mm

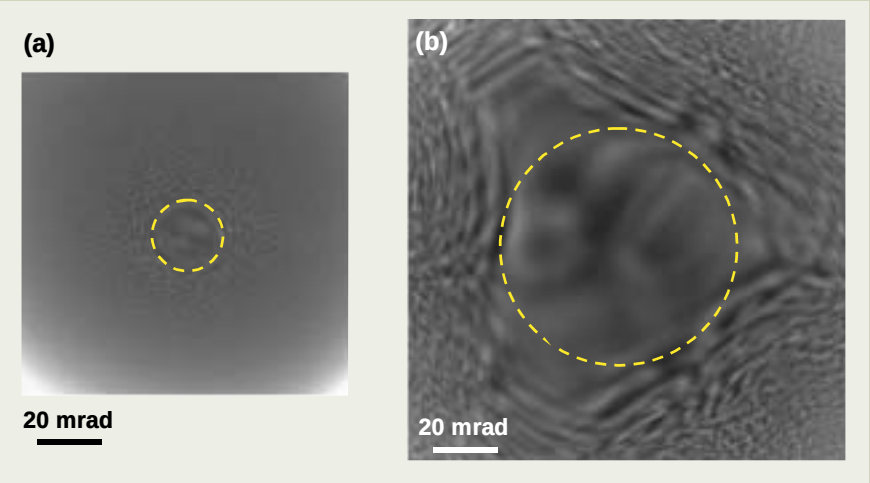

Fig. 3 Ronchigrams (defocused shadow images) recorded from a specimen of Au nano-particles on a Ge film at nearly focused conditions in the JEM-2200FS: (a) uncorrected mode with hexapole-off and (b) corrected mode with hexapole-on. The twofold astigmatism and 2nd–order axial coma were manually aligned.

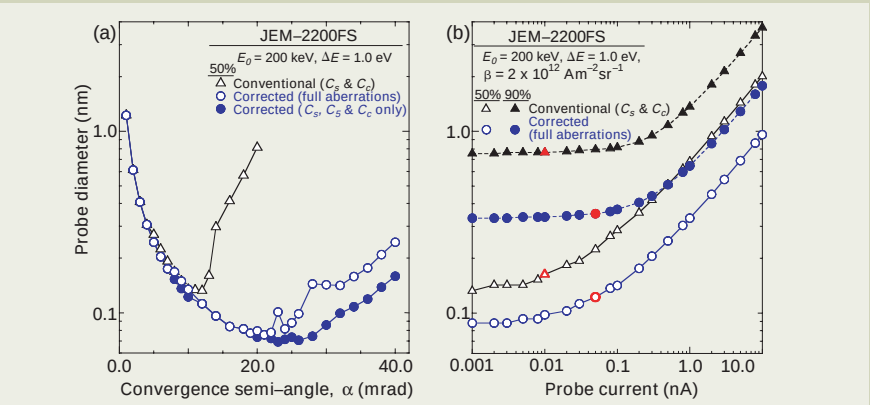

Fig. 4 (a) The probe diameters containing 50% of the total intensity simulated based on the polychromatic point source for the conventional (open triangle) and aberration corrected (full aberrations: open circles, main aberrations only: closed circles) JEM-2200FS, plotted as a function of the convergence semi-angle. (b) The overall probe diameters containing 50% and 90% of the total intensity simulated by convolving the polychromatic intensity distribution with the Gaussian intensity distribution, plotted against the probe current. The polychromatic intensity distributions at α = 12 and 25 mrad were used for the conventional (open & closed triangles) and aberration-corrected (open & closed circles) conditions, respectively.

Fig. 8 (a) An HAADF-STEM image of an $L1_2$-type γ' precipitate along <100> in the Ni-base superalloy X-750. This image is slightly distorted due to some instabilities during acquisition. (b) Intensity profiles extracted from atomic layers containing only face-centered atoms (A site) and both face-centered and corner atoms (A & B sites). (c) EELS spectra around the Ti $L_{2,3}$ edge measured from the A- and B-sites, respectively. (See the next page.)

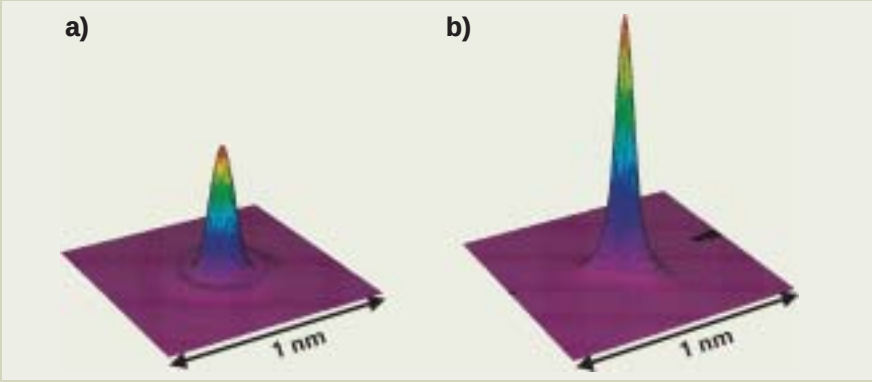

Fig. 5 The intensity distributions simulated in the conventional condition at α = 12 mrad with a probe current of 10 pA (a) and in the aberration-corrected condition at α = 25 mrad with α 50-pA probe current (b). Both the distributions were drawn with the same vertical intensity scale.

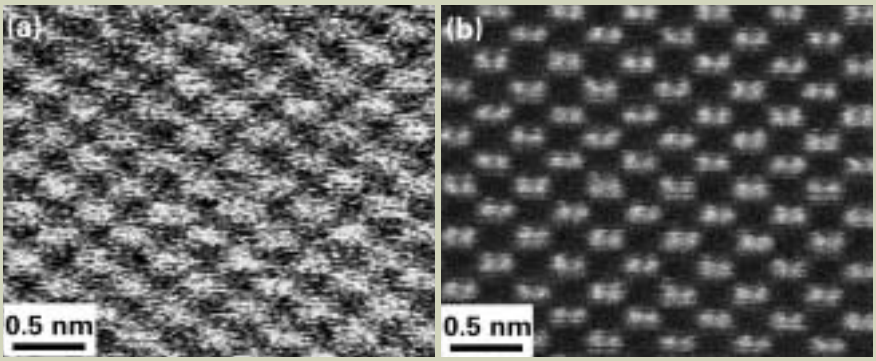

Fig. 6 HAADF-STEM images of Si <110> recorded in the conventional (a) and aberration- corrected (b) conditions using the JEM-2200FS.

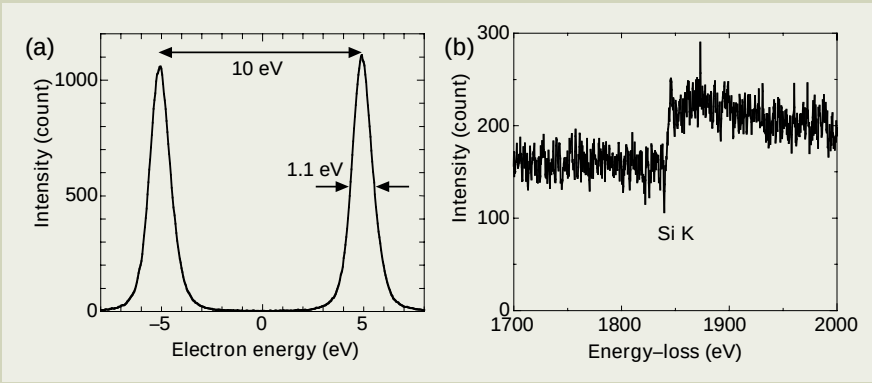

Fig. 7 (a) Zero-loss intensity distributions separated by a 10-eV energy shift for energy resolution measurement and (b) an EELS spectrum acquired in the vicinity of the Si K edge (1839 eV) recorded in aberration-corrected STEM mode with a 50-pA probe current.

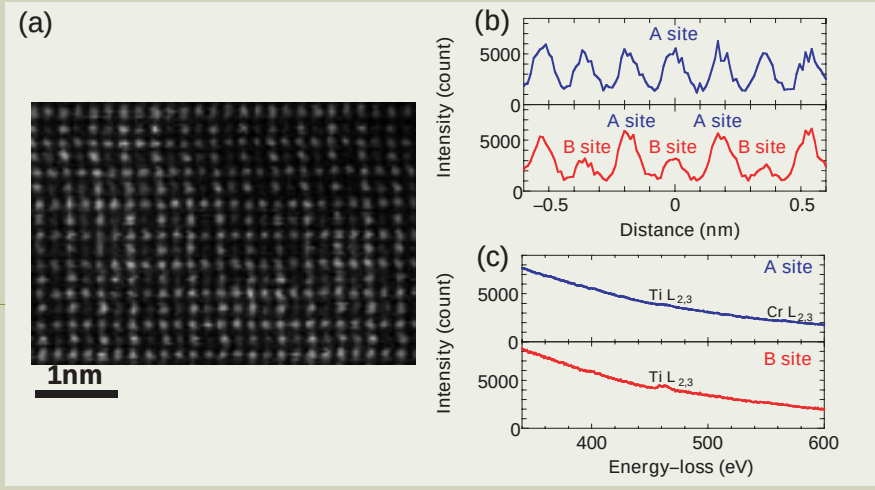

ing aperture can be used without suffering any influence of lens aberration. Therefore, the use of aberration correction for probe refinement can provide not only improved resolution in HAADF imaging, but also actual benefits for analysis via X-rays or energy-loss electrons due to the significantly increased probe currents (5-10 ×).

Theoretical evaluation of probe dimensions in aberration-corrected STEM

Both imaging and analytical performance in STEM (as exemplified by resolution and analytical sensitivity) are directly influenced by the incident probe dimensions (i.e. sizes and intensity distributions). The finest probe with the highest current is always preferable to achieve the best imaging and analytical performance. In order to perform STEM imaging and analysis with the highest possible resolution and sensitivities, it is essential to estimate the optimized probe forming conditions and the probe dimensions for appropriate applications. Since the uniform intensity area in the Ronchigram is expanded by the STEM aberration-correction as shown in **Fig. 3**, the optimized conditions in the aberration-corrected mode are very different from those encountered in the conventional situation. In general, the complete probe simulation can be performed via three steps: (i) calculation of the intensity distribution from a monochromatic point source that contains only geometrical aberrations and defocus, (ii) calculation of the intensity distribution from a polychromatic point source including chromatic aberration by adding a series of monochromatic intensity distributions with certain weights based on the electron energy spread function of the gun and (iii) calculation of the intensity distribution from an overall extended source by convolving the polychromatic distribution with the contribution of the probe current. The details of the probe simulation are summarized by Colliex and Mory [9]. In this study, the intensity distributions from the monochromatic and polychromatic point sources were simulated by following an approach described by Haider *et al.* [10].

Figure 4(a) shows probe diameters of the polychromatic intensity distributions containing 50% of the total intensity (which is usually considered as a suitable size for HAADF image resolution) in the conventional and aberration-corrected conditions of the JEM-2200FS, plotted as a function of the convergence semi-angle (α). For this simulation, the aberration coefficients summarized in Table 1 were used with the source energy spread of 1.0 eV. It should be noted that the probe diameters in the aberration-corrected conditions were simulated with only major aberration coefficients of C_s, C_5 and C_c (closed circles) and with full aberration coefficients up to 5th-order except for A_1 and B_2 (open circles). Hence, it can be considered that the probe diameters simulated using only the major aberrations are ideal limits in this particular aberration-corrected condition. In the conventional condition, the probe diameter becomes a minimum (optimum) at α = 11-12 mrad, which is consistent with the angular range of uniform intensity in the Ronchigram as shown in **Fig. 3(a)**. In contrast, the probe diameter in the

aberration-corrected conditions becomes a minimum at α = 20-26 mrad, which is higher than the optimum α in the conventional condition. However, the optimum α in the aberration-corrected condition is still smaller than the angle measured from the uniform intensity area (> 34 mrad) in the Ronchigram shown in **Fig. 3(b)**. The difference in the optimum angle between the simulated probe diameter and the experimentally obtained Ronchigram suggests that the uniform intensity area size may not simply be used as an estimate of the optimum aperture size, especially in the aberration-corrected condition. Further discussion concerning the optimum probe conditions will be published elsewhere [11].

The simulated probe diameters shown in **Fig. 4(a)** represent blurring of a point source due to the geometrical (monochromatic) and chromatic (polychromatic) aberrations. These probe diameters are useful to estimate the optimum conditions for obtaining ideal resolution of the HAADF-STEM imaging with limited probe currents. However, it is essential to take into account the contribution of the probe current in order to estimate spatial resolution for analysis via X-rays or energy-loss electrons, as pointed out by Brown [12] and Watanabe et al. [5]. Because the contribution of the probe current can be described by assuming an initial Gaussian diameter at the electron gun, the overall probe distribution from the extended source can be calculated by a convolution of the polychromatic intensity distribution with the Gaussian image of the electron gun [9]. For simulation of the Gaussian diameters, a brightness value of 2×10^{12} $Am^{-2}sr^{-1}$ was used for the Schottky FEG source [13]. The overall probe diameters simulated at the optimum α for the conventional and aberration-corrected conditions (12 and 25 mrad, respectively) are plotted against the probe current in **Fig. 4(b)**. Probe diameters containing 90% of the total intensity (closed symbols) are also plotted in addition to the 50% diameters (open symbols) since the 90% diameter is a more relevant definition for chemical analysis [5, 14]. In the conventional condition, the probe current is usually limited to ~10 pA for atomic resolution HAADF-STEM imaging and the 50% and 90% probe diameters are found to be ~1.6 and 7.6 Å, respectively (plotted in red in **Fig. 4(b)**). The simulated intensity distribution of the incident probe and a HAADF-STEM image of Si <110> recorded in the conventional condition are shown in **Figs. 5(a)** and **6(a)**, respectively. The image is very noisy due to the limited probe current available, and the projected Si-Si dumbbell spacing of 1.36 Å could not be resolved.

In the aberration corrected condition, the probe current can be increased to over 100 pA to obtain the same 50% probe diameter (1.6 Å) as in the conventional condition. This > 10× higher current can improve the analytical sensitivity in XEDS and EELS experiments. On the other hand, the 50% diameter can be made smaller than 1 Å up to a 20 pA probe current. In the probe current range between 10 -100 pA, all the microscope parameters such as the gun emission and gun/column lens setting were carefully chosen in order to achieve improved resolution in HAADF-STEM imaging *and* to gather sufficient signals for EELS analysis. Conversely, the energy resolution of the incident electrons needs to be kept as good as possible since the energy resolution is usually degraded as the gun emission increases to generate higher probe currents. Therefore, it has been found that the current at which the probe becomes compromised by the above conflicts is ~50 pA. According to the results of the probe simulation shown in red symbols in **Fig. 4(b)**, the diameters containing 50 and 90% of the total intensity are 1.2 and 3.5 Å, respectively. **Figures 5(b)** and **6(b)** show the simulated probe shape and a recorded HAADF-STEM image of Si <110> with 50 pA in the aberration-corrected condition. The peak intensity in the corrected probe is about twice that in the conventional probe. This enhancement can provide a better signal-to-noise ratio in imaging. It is however important to note that the aberration-corrected probe has threefold tails instead of the ring-shape tail typical of a spherically aberrated probe (**Fig. 5(a)**). The threefold tails in the corrected probe are caused by the residual higher-order aberrations in the hexapole-based corrector. In comparison with the conventional image in **Fig. 6(a)**, the ADF-STEM image of Si <110> (**Fig. 6(b)**) is greatly improved with higher contrast and the 1.36 Å spacing is now successfully resolved. **Figure 7** shows some EELS results obtained in this aberration-corrected STEM condition. **Figure 7(a)** presents the energy resolution in this particular condition determined by recording two zero-loss peaks separated with a 10-eV energy shift. **Figure 7 (b)** shows an EELS spectrum in the vicinity of the Si K edge (1839 eV) for a 10-s acquisition. It is possible to measure such an EELS spectrum at higher core-loss regions with a reasonable acquisition time while still maintaining the atomic-scale resolution (1.36 Å) and a reasonable energy resolution (~1.1 eV). Therefore, atomic-column characterization of materials can in practice be performed by EELS analysis in the aberration-corrected JEM-2200FS.

A demonstration of atomic-column characterization

Figure 8(a) shows an atomic-resolution HAADF-STEM image recorded from a <100> projection of an $L1_2$-type γ' precipitate (Ni_3Al) in a Ni-base superalloy (X-750). In this particular projection of the precipitate, the atomic separation is ~1.8 Å, which is clearly resolved in the HAADF image. Furthermore, there are two distinctly different intensities displayed by the major atomic columns in the HAADF image. Intensity profiles extracted from an atomic layer containing only brighter atomic spots and from a layer with both brighter and darker columns in the HAADF image are shown in **Fig. 8(b)**, respectively. The intensities in the darker columns are ~1/3 of that found in the brighter columns, which is indicative of the difference in average atomic number between the projected atomic columns. In comparison with the expected atomic configurations in the $L1_2$ structure, the brighter columns correspond to face-centered Ni (A site), whereas the less intense columns correspond to corner Al (B site) atom positions in the $L1_2$ structure.

According to XEDS analysis performed prior to the HAADF and EELS approaches, this γ' precipitate has a high Ti content (about twice that of Al in atomic fraction). **Figure 8(c)** shows two EELS spectra in the vicinity of the Ti $L_{2,3}$ edge (~450 eV) recorded from the A and B sites, respectively. It is clear that the Ti $L_{2,3}$ edge intensity is more significant in the spectrum obtained from the B site. These results suggest that the Ti atoms preferentially occupy the B-site in the $L1_2$ structure by substituting for Al atoms, which agrees with previous studies using the X-ray based ALCHEMI method [e.g. 15]. Using the new generation aberration-corrected STEMs, therefore, such site occupancies of alloying elements or even impurity elements can be determined *directly* at the individual atomic-column level, not by averaging information from broad regions as is traditionally done using the ALCHEMI method. Characterization on the atomic column-by-atomic column scale can now, at last, be achieved in practice using state-of-the-art commercial STEMs equipped with aberration correctors. This atomic-column point analysis capability implies that not only detection, but also the characterization of a single atom impurity is feasible in aberration-corrected STEMs, when used in combination with the latest spectrum imaging and advanced statistical analysis techniques.

TEM Performance with an Activated STEM Corrector

In addition to the impressive STEM performance, the JEM-2200FS has all the TEM functionality as well, and it is designed so that both the TEM and aberration-corrected STEM modes can be seamlessly switched back and forth. TEM performance of this type has previously been reported for an instrument with a TEM aberration corrector [2, 8]. In the original TEM mode, the aberration corrector is deactivated. In the JEM-2200FS at Lehigh, however, the TEM mode has been set up while keeping the aberration corrector activated. This special TEM mode is called the CsTEM mode and is very important for doing atomic resolution STEM work where one wishes to avoid any electronic instabilities caused by turning the STEM corrector on and off. Several TEM-resolution performance characteristics in the CsTEM mode are summarized in **Fig. 9**. The point resolution as determined from Au particles on a Ge thin-film using the optical diffraction method is 0.19 nm (**Fig. 8(a)**). The information limit measured from a poly-crystalline Ti thin-film by employing the Young's fringe method was found to be 0.11 nm (**Fig. 9(b)**). **Figures 9(c)** and **(d)** show an atomic resolution phase contrast image from Si <110> and its Fourier-transformed diffractogram, respectively. Although the 1.36-Å atomic spacing is not resolved in the phase contrast image, Bragg spots corresponding to {224}, {115} and {333} reflections are visible in the diffractogram. Since these Bragg spots correspond to the atomic spacings of 0.110 (Si{224}) and 0.105 nm (both Si{115} and Si{333}), the result correlates well with the measured point resolution and information limit presented in **Figs. 9(a)** and **(b)**. Because the measured TEM performance results in the CsTEM mode are identical with those in the original TEM mode, it can be concluded that the TEM performance of the JEM-2200FS is not degraded at all by the activation of the STEM corrector. Additionally, a static convergent probe can also be formed with STEM-corrector activation, which is called the CsCBD mode. In contrast to the CsTEM mode, the probes formed in the CsCBD mode are actually corrected by the STEM corrector. Therefore, the aberration-corrected fine probes

in this instrument are available even in the static probe mode in addition to the scanning probe mode.

In the static probe mode, materials can also be characterized by energy-filtering via the Ω filter. **Figure 10** shows a series of energy-filtered images taken from a cross-section Si/Si-Ge multilayer thin film, which is reported to be one of the most useful specimens for evaluating energy-filtered images [16]. Unfiltered (conventional) and zero-loss filtered bright-field (BF) images are shown in (a) and (b), respectively, and the relative thickness map determined from both the BF images is presented in (c). The elemental maps of Si L (d), Ge L (e) and Si K (f) ionization edges were obtained by the three-window method. These filtered images were recorded in the CsTEM mode. The elemental distributions using higher energy-loss edges such as the Ge L (1217 eV) and Si K (1839 eV) are very clear. This is a clear demonstration that the illumination compensation works very well at higher energy-loss regions.

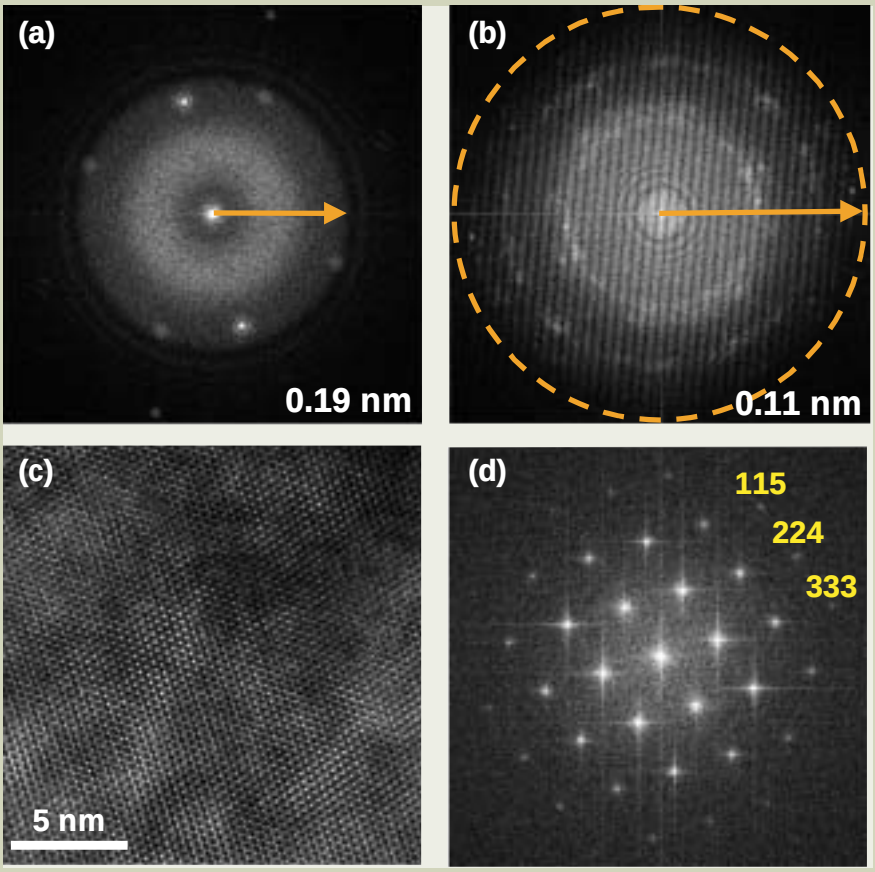

Fig. 9 (a) Point resolution measured from Au particles on a Ge thin film by the optical diffraction method. (b) Information limit measured from a Ti thin film by the Young's fringe method. (c) An atomic resolution phase-contrast image of Si <110> and (d) its corresponding diffractogram.

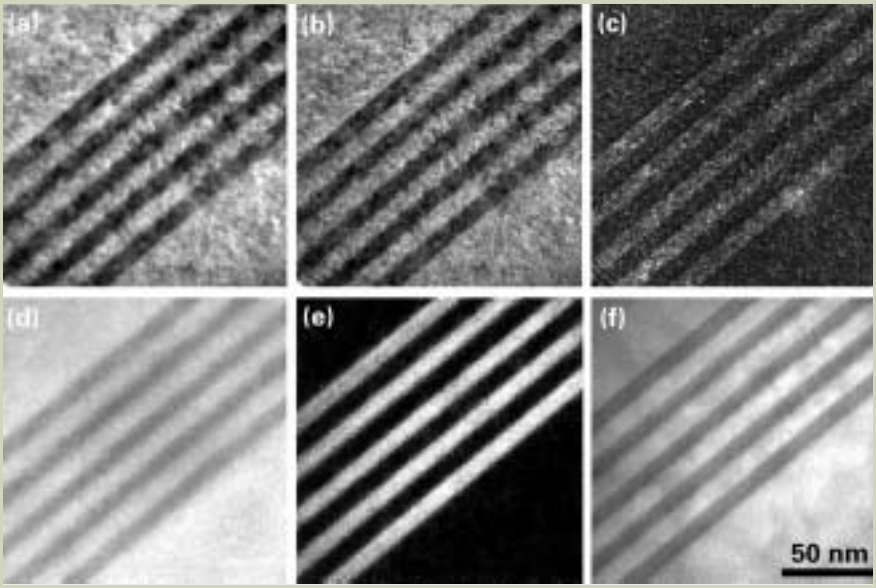

Fig. 10 A series of energy-filtered images from a Si/Si-Ge multilayer thin specimen measured in the CsTEM mode: (a) unfiltered BF image, (b) zero-loss filtered BF image, (c) relative thickness map, (d) Si L map, (e) Ge L map and (f) Si K map.

Summary

The newly developed JEM-2200FS STEM/TEM has been successfully installed at Lehigh University. This instrument has been optimized for EELS analysis in the atomic-resolution HAADF-STEM imaging mode by the integration of the CEOS aberration-corrector for STEM and an in-column Ω-filter, which provides significant improvements in the imaging and analytical performance. Characterization on the atomic column-by-atomic column scale can be achieved using the JEM-2200FS with the STEM aberration corrector. In addition to the STEM mode, static-beam TEM-based operations can also be performed without any degradation in atomic resolution phase-contrast imaging or energy filtering in the STEM-corrector activated mode.

Acknowledgements

The authors wish to acknowledge the support of the National Science Foundation through grants (DMR-9626279 and DMR-0320906) and of Bechtel Bettis, Inc (MW and DBW).

References

[1] M. Haider et al.: *Nature*, **392**, 768 (1998).
[2] J. L. Hutchison et al.: *Ultramicrosc.*, **103**, 7 (2005).
[3] P. D. Nellist et al.: *Science*, **305**, 1741 (2004).
[4] M. Varela et al.: *Rev. Mat. Res.*, **35**, 539 (2005).
[5] M. Watanabe et al.: *Microsc. Microana.* (in press).
[6] D. A. Muller and J. Grazul.: *J. Electron Microsc.*, **50**, 219 (2001).
[7] M. Haider et al: *Ultramicrosc.*, **75**, 53, (1998).
[8] H. Sawada et al.: *J. Electron Microsc.*, **54**, 119 (2005).
[9] C. Colliex and C. Mory.: *Quantitative Electron Microscopy* (ed. by J. N. Chapman & A. Craven), Scottish University Summer School in Physics, Glasgow, Scotland, p. 149 (1984).
[10] M. Haider et al.: *Ultramicrosc.*, **81**, 163 (2000).
[11] M. Watanabe et al.: (in preparation).
[12] L. M. Brown.: *J. Phys. F: Metal Phys.*, **11**, 1 (1981).
[13] H. Tanaka et al.: *J. Electron Microsc.*, **51S**, 127, (2002).
[14] D. B. Williams et al.: *Ultramicrosc.*, **47**, 121 (1992).
[15] Z. Horita et al.: *Phil. Mag. A*, **67**, 425 (1993).
[16] T. Oomura et al.: *J. Electron Microsc.*, **51S**, 87 (2002).

Applications of Aberration Corrected Transmission Electron Microscopy to Materials Science

Angus I. Kirkland, Lan-Yun Chang and John L. Hutchison

Department of Materials, University of Oxford

The performance of electron microscopes has undergone a dramatic improvement with the development of electron-optical aberration correctors. It is now possible to probe individual atomic sites in many materials and to determine atomic and electronic structure with single atom sensitivity. This paper presents a brief overview of some of these instrumental advances and their application to structural problems in materials science.

Introduction

Richard Feynman is commonly associated with the nanoscience revolution as a result of his lecture "There's Plenty of Room at the Bottom" given in 1959 [1]. Less well known, is his challenge, in the same lecture to "improve the resolution of the electron microscope by 100 times". It has been long understood that the resolution of the electron microscope is limited by the intrinsic spherical aberration in the objective lens to values nearly two orders of magnitude poorer than the electron wavelength. This spherical aberration arises from the rotationally symmetric magnetic field of the objective lens and to correct this requires sophisticated electron-optical components which break the rotational symmetry [2]. The successful design and development of such correctors for transmission electron microscopes (**Figure 1**) has led to a rapid improvement in the interpretable resolution to sub 0.1 nm levels at intermediate voltages (**Figure 2**). The major reason that it has taken over four decades to achieve this is the requirement for sophisticated computer control to measure the aberrations present and to iteratively adjust the necessary lens currents. However, the current generation of correctors readily achieve this and are able to correct the electron wave front to a degree of perfection better than a quarter wavelength (~ 0.5 pm) over 70 microns, a level of performance that exceeds that of the Hubble Space Telescope.

There are presently two designs of aberration corrector available for electron microscopes produced by Nion [3] and by CEOS [4]. The former has been exclusively used in Scanning Transmission Electron Microscopy (STEM), whereas the latter has been used in both STEM and in conventional Transmission Electron Microscopy (TEM). Although the optical design of these two systems differs, it is important to appreciate that both correct only for the geometric aberrations (**Figures 3 (a) and (b)**) of the optical system through the use of non-round elements. Chromatic aberration (**Figure 3 (c)**) correctors which require electrostatic elements have so far only been successfully developed in the Scanning Electron Microscope (SEM) [5] which operates at significantly lower accelerating voltages.

Aberration correction in TEM images leads to both improvements in interpretable resolution and to reduced image delocalisation. In the absence of spherical aberration, to a first approximation, the point-to-point resolution in a high resolution image is extended out to the limits imposed by the partial temporal coherence of the illumination. Information delocalisation, arising from the presence of aberrations in an uncorrected microscope, is also substantially reduced with particular benefits to imaging of surfaces, boundaries and other aperiodic features.

Mention should also be made of indirect methods which deconvolve the effects of aberrations from a series of TEM images, to restore the complex wavefunction at the exit plane of the specimen [6]. These "off-line" procedures can be usefully applied not only to uncorrected TEMs but also to TEMs fitted with aberration correctors to remove the effects of residual aberrations and to compensate for higher order aberrations that cannot be corrected directly (see later).

Aberration Measurement and Correction

An essential component in the operation of aberration corrected instruments is the measurement of the objective lens aberrations. The relevant theories of wave optics applicable to HRTEM are well established and are detailed elsewhere [7, 8]. The aberration coefficients are conveniently defined in terms of a wave aberration function, W that measures the axial distance between the actual diffraction plane wavefront and the ideal spherical wavefront and importantly for HRTEM also describes the phase shift in a ray passing through the lens in a particular direction.

In polar form this can be written as a Taylor expansion (to third order) with (complex) aberration coefficients

$$\begin{aligned} W(\theta,\phi) = {} & |A_0|\,\theta\cos(\phi-\phi_{11}) \\ & +\tfrac{1}{2}|A_1|\,\theta^2\cos 2(\phi-\phi_{22})+\tfrac{1}{2}C_1\theta^2 \\ & +\tfrac{1}{3}|A_2|\,\theta^3\cos 3(\phi-\phi_{33}) \\ & +\tfrac{1}{3}|B_2|\,\theta^3\cos(\phi-\phi_{31}) \\ & +\tfrac{1}{4}|A_3|\,\theta^4\cos 3(\phi-\phi_{44}) \\ & +\tfrac{1}{4}|S_3|\,\theta^4\cos 2(\phi-\phi_{42})+\tfrac{1}{4}C_3\theta^4+\ldots \end{aligned} \qquad [1]$$

which demonstrates the azimuthal and radial dependence of the various aberration terms. The terms in C_1 and C_3 correspond to defocus and spherical aberration and are the only terms present in perfectly round lenses with the

Parks Road, Oxford OX1 3PH, U.K.
E-mail: angus.kirkland @materials.ox.ac.uk

spherical aberration positive for electromagnetic lenses. In order to correct them it is necessary to introduce combinations of multipole fields of appropriate symmetry which forms the optical basis for aberration correction.

The aberration correctors used in the JEOL JEM-2200FS installed at Oxford [9] are based on a pair of strong electromagnetic hexapole elements together with four additional lenses [10] (**Figure 4**). Correction is achieved due to the fact that the primary second- order aberrations of the first hexapole (a strong three fold astigmatism) are exactly compensated by the second hexapole element. Owing to their nonlinear diffraction power, the two hexapoles additionally induce a residual secondary, third-order spherical aberration which is rotationally symmetric with a negative sign, thus cancelling the positive spherical aberration of the objective lens. For HREM applications it is essential that the corrector is aplanatic to provide a sufficiently large field of view which can be achieved by matching the coma-free plane of the objective lens to that of the corrector using a round transfer-lens doublet. In addition to these primary optical elements the correctors also contain a number of additional weak multipole elements which are used for alignment and correction of any residual parasitic aberrations.

These phase shifts determined by the aberration coefficients of Equation 1 can be usefully used to estimate the maximum tolerable value in any coefficient for a particular target resolution as given in **Table 1** which in turn reflects the required precision in their measurement. In particular Table 1 clearly indicates the twin requirements of both increased precision in the measurement of any given coefficient with increasing resolution and for the determination of an increased number of coefficients as the resolution is improved.

Practical operation of aberration correctors requires the accurate, local measurement of the aberration coefficients. Experimental determi-

Fig. 1 A modern 200 kV corrected TEM/STEM fitted with both probe forming and imaging correctors.

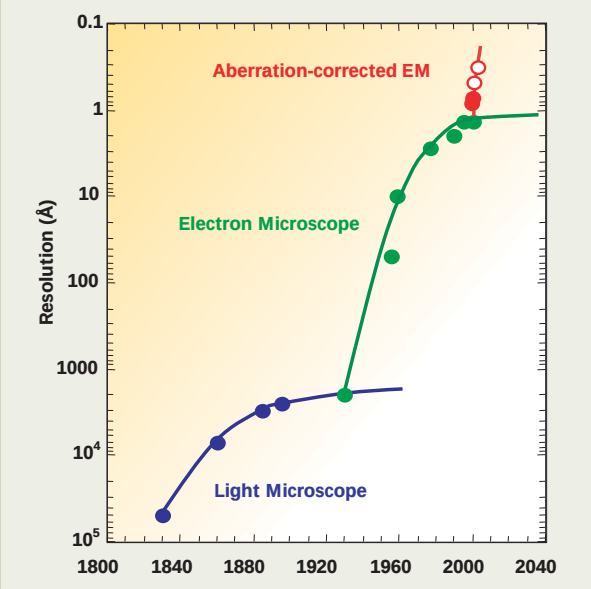

Fig. 2 The historical evolution of resolution in the TEM (after H. Rose, adapted from [2]).

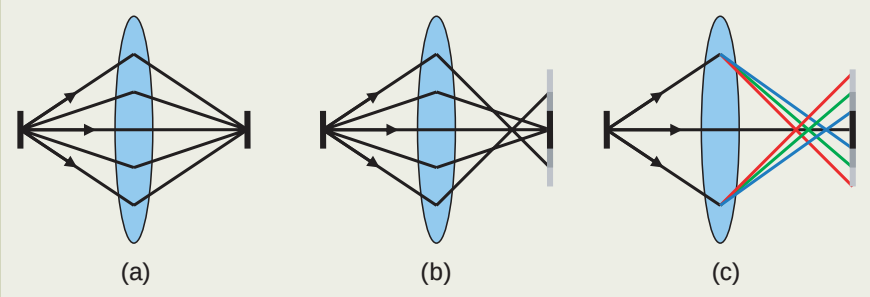

Fig. 3 Illustration of certain lens aberrations. (a) A perfect lens focuses a point source to a single image point. (b) Spherical aberration causes rays at higher angles to be overfocused. (c) Chromatic aberration causes rays at different energies (indicated by color) to be focused differently.

nation of the majority of the axial aberration coefficients relies on the measurement of one of several possible observables as a function of known injected beam tilts. The most commonly used methods rely on the determination of either image shifts, or defocus and astigmatism for which a suitably conditioned set of known beam tilts provides a method for measuring all coefficients [8, 11, 12]. The advent of aberration-corrected instruments has made automated aberration measurement even more important because the non-round lens elements introduce a multitude of high-order aberrations (up to six-fold astigmatism) that require correction in an elaborate alignment procedure. For this purpose the current generation of TEM correctors rely on a robust and computationally efficient algorithm that evaluates the apparent defocus and astigmatism from a diffractogram in less than 400 ms based on a comparison of experimental diffractograms to a stored library of simulated diffractograms.

Applications to Materials Science

The first application described here is the characterisation of nanometer sized crystals of compound semiconductors which exhibit novel optical properties. **Figure 5** shows aberration corrected images of nanometer sized CdSe crystallites in which the benefits of aberration correction are immediately evident. In the first instance the elimination of the spherical aberration leads to a significant reduction of image delocalisation at the particle surface, thus enabling a more accurate measurement of the particle shape in projection. In addition the restricted depth of field leads to a substantial reduction in contrast from the amorphous support film compared to uncorrected imaging, further increasing the visibility of the particle. In particular we note that both particles shown in **Figure 5** exhibit stacking faults, dislocations and regions of both hexagonal and cubic stacking sequences despite their small size and this may have a direct influence on their optical properties.

Our second example application combines direct electron optical aberration correction with local aberration measurement [13] and subsequent exit wave restoration as summarised in **Figure 6**. For the experiment described here a focal series of aberration corrected images was initially used to recover the specimen exit wave using a Wiener restoring filter [6]. Subsequently local aberration coefficients from a subregion of interest were measured to an accuracy of <1 nm [11, 12] and these were used to refine the exit wave by application of an appropriate phase plate parameterised by the locally determined axial aberrations in Fourier space. **Figure 7** illustrates the phase plates obtained after initial electron optical correction to third order and subsequently after refinement to fifth order together with the resultant exit wave function of a nanocrystalline Pt particle. It is apparent that whereas the initial phase plate shows significant variation at the 0.1 nm transfer limit set by the partial coherence of the microscope the refined phase plate is constant to a value beyond this limit. The restored phase of the particle shows a number of interesting structural features which are not immediately apparent in the individual images including

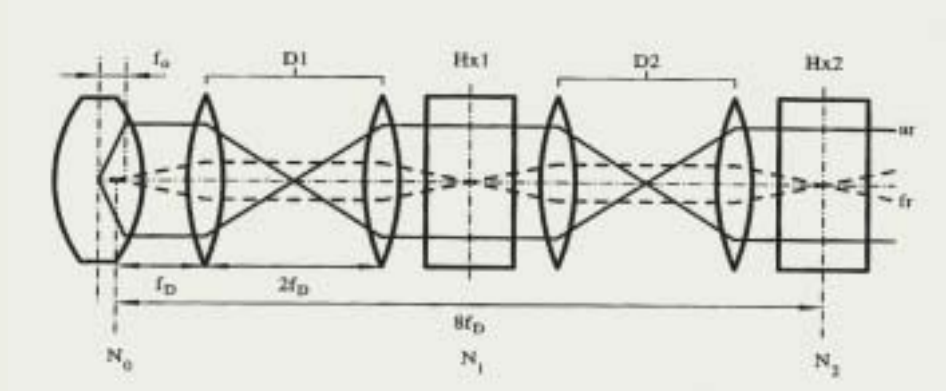

Fig. 4 Optical ray diagram for the hexapole based aberration corrector used in the Oxford — JEOL JEM-2200FS (reproduced from [10]).

Table 1 Precision required in the coefficients of the wave aberration function for various target resolutions (adapted from [10]).

Cocfficient	π/4 limit	π/4 limit at 200kV		
		g_{max} = 4nm^{-1}	g_{max} = 7nm^{-1}	g_{max} = 10nm^{-1}
C_1	$\frac{1}{4}(\lambda g_{max}^2)^{-1}$	6.2nm	2.0nm	1.0nm
A_1	$\frac{1}{4}(\lambda g_{max}^2)^{-1}$	6.2nm	2.0nm	1.0nm
A_2	$\frac{3}{8}(\lambda^2 g_{max}^3)^{-1}$	0.93μm	0.17μm	60nm
B_2	$\frac{1}{8}(\lambda^2 g_{max}^3)^{-1}$	0.31μm	58nm	20nm
C_3	$\frac{1}{2}(\lambda^3 g_{max}^4)^{-1}$	0.12mm	13μm	3.2μm
A_3	$\frac{1}{2}(\lambda^3 g_{max}^4)^{-1}$	0.12mm	13μm	3.2μm
S_3	$\frac{1}{8}(\lambda^3 g_{max}^4)^{-1}$	31μm	3.3μm	0.79μm
A_4	$\frac{5}{8}(\lambda^4 g_{max}^5)^{-1}$	15mm	0.94mm	0.16mm
B_4	$\frac{1}{8}(\lambda^4 g_{max}^5)^{-1}$	3.1mm	0.19mm	32μm
D_4	$\frac{1}{8}(\lambda^4 g_{max}^5)^{-1}$	3.1mm	0.19mm	32μm
C_5	$\frac{3}{4}(\lambda^5 g_{max}^6)^{-1}$	1.8m	64mm	7.6mm
A_5	$\frac{3}{4}(\lambda^5 g_{max}^6)^{-1}$	1.8m	64mm	7.6mm

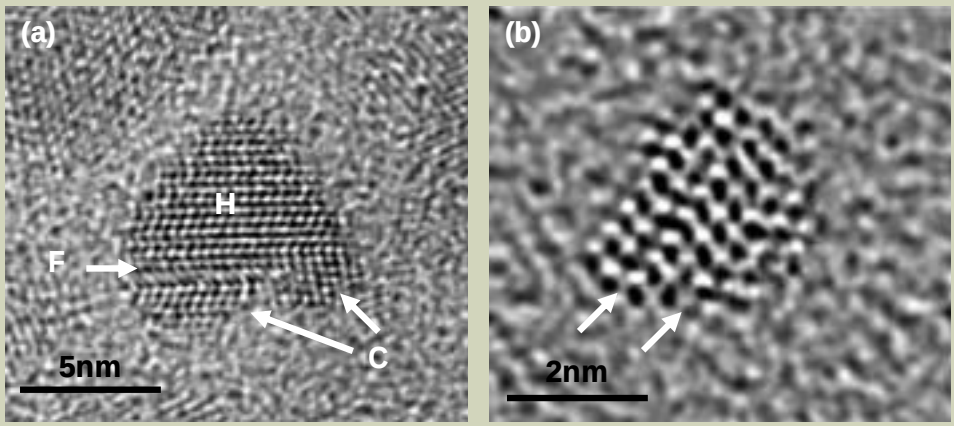

Fig. 5 Aberration corrected images of nanometer sized CdSe particles (a) 5 nm crystallite showing hexagonal and cubic stacking regions (marked H and C respectively) and a {111} stacking fault marked F (b) 2 nm CdSe crystallite containing stacking faults marked with arrows.

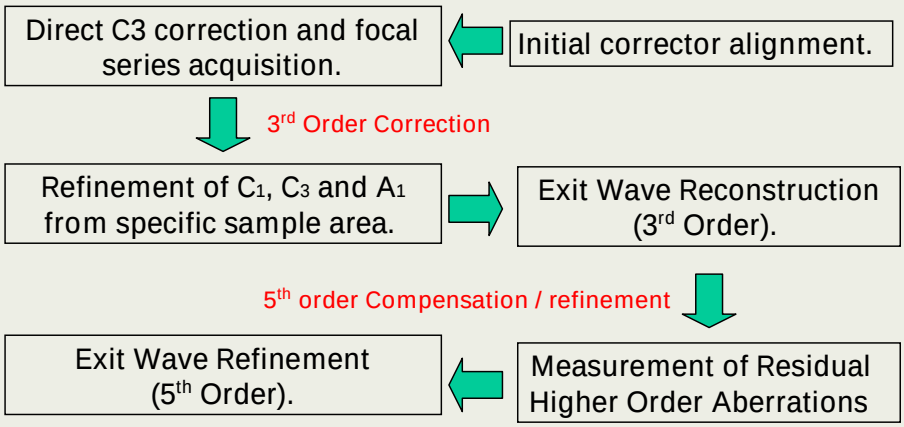

Fig. 6 A schematic illustration of the steps involved in combined electron optical correction and exit wave reconstruction.

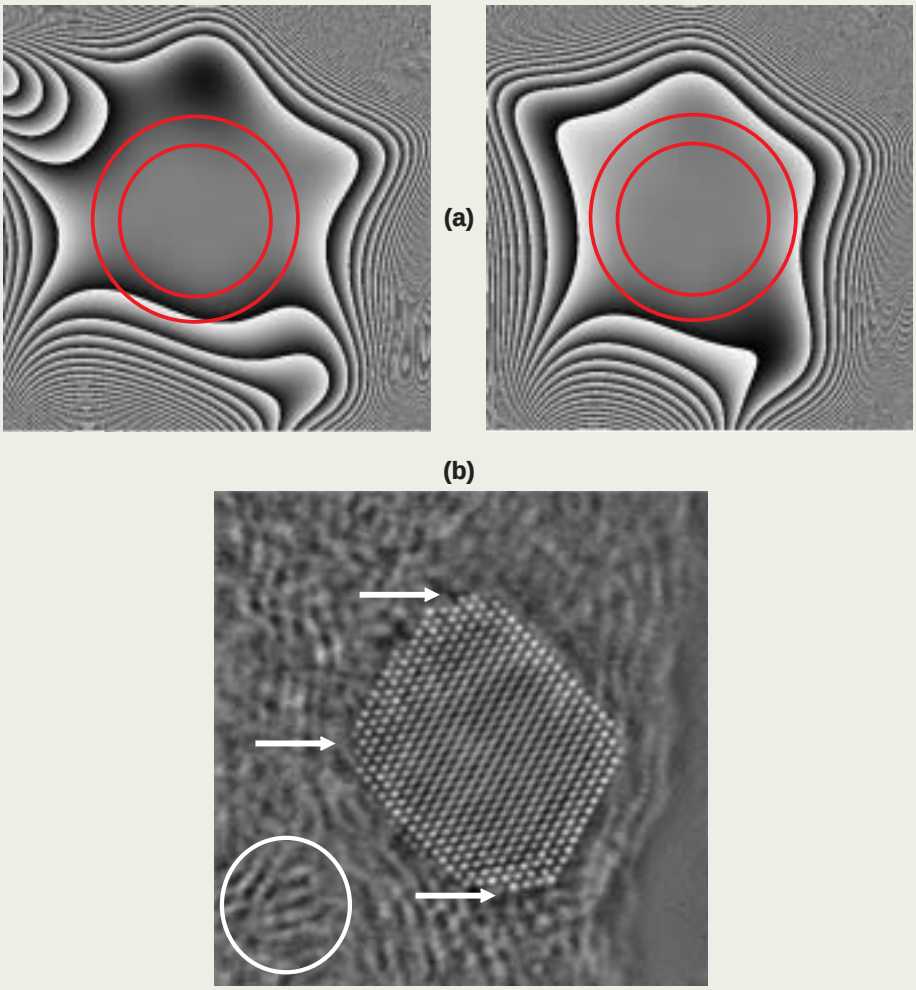

Fig. 7 (a) Phase plates prior to (left) and post (right) aberration refinement to 5th order. Inner and outer circles mark resolution limits of respectively 0.1 and 0.08 nm in both cases. (b) Restored exit plane wavefunction of a nanocrystalline platinum catalyst particle restored from an aberration corrected through focal series of images and subsequent aberration refinement as described in the text. Arrows mark local surface irregularities and the circle highlights localised support crystallinity.

stepped and partially occupied surfaces and local support crystallinity.

Conclusions and Future Directions

At the present time spherical aberration has been successfully corrected in TEM, improving the point resolution to the information limit. In order to extend the information limit itself there are two possibilities, both of which are actively being pursued. The first possibility is to reduce the energy spread of the electrons (and thus improve the limit set by temporal coherence) by replacing the standard thermally assisted Schottky FEG with a Cold FEG, or by monochromating the electron beam. The second is to correct the chromatic aberration of the objective lens [14] using a complex combination of magnetic and electrostatic multipole elements. An improved information limit will allow not only greater detail and precision to be obtained in the analysis of the atomic structure of materials but will also permit the use of large gap pole pieces without the constraint of minimising Cs and Cc. These larger gap lenses will in turn allow the use of a wider range specialised specimen holders for in-situ experiments and measurements with dynamic observation.

Acknowledgements

The Oxford aberration corrected instrument was funded by the UK's Engineering and Physical Sciences Research Council and Oxford University. We are also grateful to JEOL Ltd. and JEOL (UK) Ltd. for their continued support and to colleagues in Oxford for many helpful discussions.

References

[1] R. Feynman, http://www.zyvex.com/nanotech/feynman.html
[2] H. Rose.: *Ultramicroscopy*, **56**,11 (1994).
[3] P. E. Batson, N. Dellby, and O. Krivanek.: *Nature*, **418**, 617 (2002).
[4] M. Haider, S. Uhlemann, E. Schwan, B. Kabius and K. Urban.: *Nature*, **392**, 768 (1998).
[5] J. Zach and M. Haider.: *Nucl. Inst. and Meth.*, **A363**, 316 (1995).
[6] A. Kirkland and R. Meyer.: *Microscopy and Microanalysis*, **10**, 401 (2004).
[7] P. Hawkes and E. Kasper (Eds.).: *Principles of Electron Optics: Wave Optics*. London: Academic Press (1996).
[8] O. Saxton.: *J. Microsc.*, **179**, 201 (1995).
[9] J. Hutchison, J. Titchmarsh, D. Cockayne, R. Doole, C. Hetherington, A. Kirkland and H. Sawada.: *Ultramicroscopy*, **103**, 7 (2005).
[10] M. Haider, H. Rose, S. Uhlemann, E. Schwan, B. Kabius and K. Urban.: *Ultramicroscopy*, **75**, 53 (1998).
[11] R. Meyer, A. Kirkland and O. Saxton.: *Ultramicroscopy*, **92**, 89 (2002).
[12] R. Meyer, A. Kirkland and O. Saxton.: *Ultramicroscopy*, **99**, 115 (2004).
[13] A. I. Kirkland, L. Y. Chang.: *Microscopy and Microanalysis*, in press (2006)
[14] H. Rose.: *Ultramicroscopy*, **103**, 1 (2005).

Visualization of Biological Nano-Machines at Subnanometer Resolutions

Wah Chiu[†,††], Donghua Chen[†], Joanita Jakana[†], Juan Chang[†,†], Wen Jiang[†,†††], Steven J Ludtke[†] and Matthew L Baker[†]

[†]National Center for Macromolecular Imaging, Verna and Marrs McLean Department of Biochemistry and Molecular Biology
[††]Program in Structural and Computational Biology and Molecular Biophysics, Baylor College of Medicine
[†††]Current address: Department of Biological Sciences, Purdue University

Introduction

Based on genome sequence analysis, it has been suggested that a living cell conducts 200-300 distinct biological processes (Martin and Drubin, 2003), each of which can be carried out by macromolecular complexes. These complexes, which can both be persistent and transitory, are usually relatively large (>0.5 MDa) and contain specific and complex spatial organization of components to facilitate their dynamic behaviors. As such, these complex assemblies actually are biological nano-machines. As the name implies, an analogy can be drawn to almost any conventional man-made machine in which the machine is composed of multiple components operating in a coordinated fashion to perform one or more biological functions. These biological nano-machines can be found throughout the cell, responsible for key processes such as cell division and signaling, as well as being critical in diseases such as cancer or viral infections. Nano-machines are not restricted to "large-scale" cellular processes and may be involved in genome replication and repair, protein folding, protein trafficking and ion transport (Gavin et al., 2006; Krogan et al., 2006). These machines can assume different forms, shapes and symmetries. Therefore, knowledge of the molecular structures of the biological nano-machines, their components and their interactions can provide both mechanistic descriptions of function and clues for developing therapeutics related to health and disease. However, because of all these intrinsic complexities, structure elucidation of biological nano-machines at sufficient resolutions often poses a serious challenge.

Houston, TX 77030
E-mail: wah@bcm.edu

Using Single Particle Cryo-EM to Study Nano-Machines

Electron cryo-microscopy (also known as cryo-electron microscopy or cryo-EM) is the most appropriate imaging technique to derive 3-D structures of biological nano-machines because of several reasons (Chiu et al., 2006; Frank, 2002). In single particle cryo-EM, samples do not need to be crystallized as in X-ray crystallography. Rather, specimens can be prepared in frozen, hydrated state at different sample conditions without chemical fixative or negative stain (Duboch et al., 1988). As the conditions attempt to mimic cellular conditions, often the frozen, hydrated samples represent a heterogeneous mixture of conformationally different particles. However, while this may be a drawback for conventional structure determination, single particle cryo-EM image processing techniques could be developed to sort out images of mixed conformations, thus capturing several states from a single experiment. Additionally, well-defined computational protocols can determine the 3-D structure of a sample directly from low dose images. Currently, the resulting reconstructions of conformationally rigid and uniform machines have achieved subnanometer (6-10 Å) resolutions (Chiu et al., 2005; Jiang and Ludtke, 2005). In this resolution range, secondary structure elements can be identified and high-resolution structures can be fitted to provide an understanding of the biological machine and its components (Chiu et al., 2002; Rossmann et al., 2005). Despite not being able to obtain atomic resolution structures of biological samples, cryo-EM continues to gain popularity in understanding biological processes as evidenced from the increasing number of publications (**Figure 1**) and the establishment of a public cryo-EM structure repository (http://www.ebi.ac.uk/msd-srv/emsearch/index.html) (Fuller, 2003).

A Single Particle Cryo-EM Experiment

As cryo-EM has assumed an increasingly important role in determining biological nano-machines, the complexity of imaging the samples to higher resolutions has also increased. However, the basic procedure (Jiang and Chiu, 2006; Serysheva et al., 2006) can be summarized as having two components: an experimental and a computational component (**Figure 2**). In the experimental portion of a cryo-EM experiment, the specimen must first be biochemically purified. While not as stringent of a restriction as other structural imaging modalities, the specimen should be relatively "pure" in terms of both conformation and function, meaning that the individual particles in sample should generally have the same structure and function. The purified sample can then be suspended in a buffer depending on the sample and the intended experiments. Typically, only a small amount of material is needed. For initial testing, as little as 100 μl at concentrations of 0.1-1 mg/ml are required. Subsequent higher resolution structural studies may require additional amounts of sample, however in some favorable cases high resolution structures may be obtained from the initial imaging of the specimen.

Once a suitably purified specimen has been obtained, the sample must then be prepared for imaging in the electron cryomicroscope. This step involves freezing the specimen on a holey

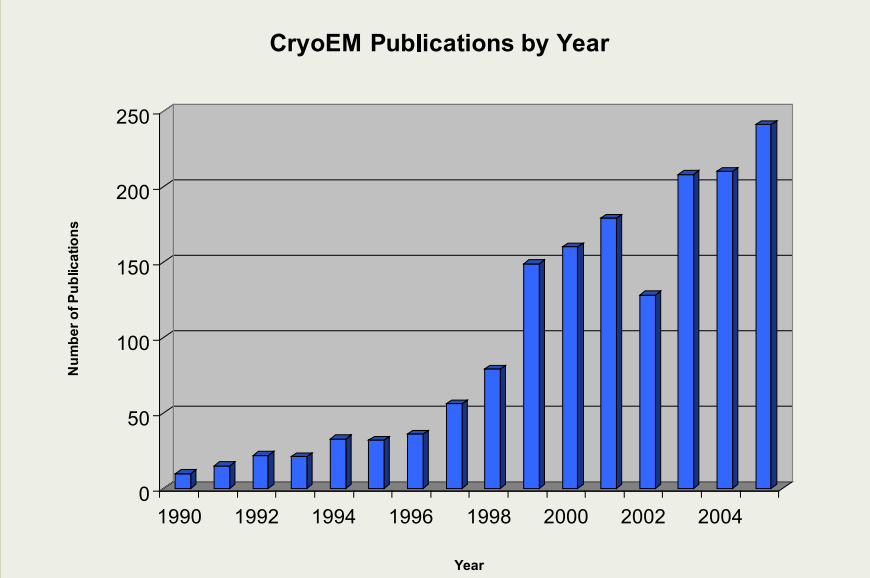

Fig. 1 Cryo-EM publications since 1990. A list of publications indexed by year is shown. This list of unique papers was generated by searching PubMed (http://www.ncbi.nlm.nih.gov/entrez/) using the Endnote software (http://www.endnote.com, The Thomson Corporation) with the following keywords: electron cryomicroscopy, cryoelectron microscopy, cryoEM and cryo-EM.

grid (e.g. Quantifoil grid) which has been cleaned and pre-treated with glow discharging. 3-5 μl of sample can then be applied to the grid with the excess liquid blotted off with filter paper. At this point, the sample can be vitrified by plunging the grid with sample rapidly into a liquid ethane bath (Dubochet et al., 1988). To accomplish this, a variety of freezing apparatuses can be used from simple hand-operated devices, to pneumatic plungers or even temperature/humidity controlled plunging chambers from commercial companies. Once the sample has been frozen, it can then be stored almost indefinitely in a liquid nitrogen dewar or imaged immediately in the electron cryomicroscope.

The freezing step can often be the rate limiting step in the experiment. For any new specimen, it is generally necessary to perform trial-and-error freezing experiments to identify suitable conditions for obtaining a sufficiently thin layer of ice yet maintaining a reasonable number of randomly orientated particles across the holes of the holey carbon grid. Often variables such as specimen concentration, buffer, blot time, wait time, carbon support, temperature and humidity must be evaluated to achieve optimal imaging conditions. One of the more frequent challenges in this step is the presence of detergent, glycerol or sucrose which has been used to help solublize, purify or store the specimens. For imaging in the electron cryomicroscope, these types of organic molecules must be removed without disrupting the integrity of the complex itself.

The third step in a cryo-EM experiment is imaging frozen, hydrated specimen in the electron cryomicroscope equipped with a cryo-specimen transfer device (**Figure 2**). The specimen grid is suspended in a cryo-specimen stage that can generally be operated at either liquid nitrogen or liquid helium temperatures. Since biological specimens are highly radiation sensitive, low dose imaging is necessary to record the images. The practical dosage ranges from 10-40 electrons/Å^2 depending on the specimen temperature and the intended resolution of the study. Typically, images are recorded at 1-3 μm underfocus in order to provide sufficient contrast to visualize the particles while still maintaining high enough resolution structural information. The imaged specimen can be recorded on photographic film or directly to a CCD camera. When using film, the data has to be subsequently digitized using a scanner, such as Nikon Super Coolscan 9000ED. In addition to their convenience, CCD cameras provide an additional benefit as the low frequency component of the image is enhanced (Booth et al., 2004), making it easier to identify the particles. Conversely, the CCD has an additional modulation transfer function that may "smear out" high frequency data. Previous experience with a commercially available Gatan 4 k × 4 k CCD camera has shown that the signal up to 2/5 Nyquist frequency can be retrieved and used in the reconstruction (Booth et al., 2004), meaning that subnanometer resolution data can be obtained at moderate microscope magnifications (i.e. 80,000 ×).

In the second half of the cryoEM experiment, computational techniques are used to transform the 2-D images of the randomly orientated particles into an intermediate resolution 3-D structure, typically referred to as a reconstruction (**Figure 2**). The digital data, whether acquired directly from the CCD camera or digitized using a scanner, is subject to a series of data processing steps that determine the parameters associated with the contrast transfer function of the microscope and the envelope function of the images. These parameters serve to make corrections to the image data prior to merging the individual 2-D particle images into a single 3-D reconstruction.

There are numerous image processing packages such as Spider (Frank et al., 1996), IMAGIC (van Heel et al., 1996), MRC (Crowther et al., 1996), Frealign (Grigorieff, 1998), PFT (Baker and Cheng, 1996), XMIPP (Sorzano et al., 2004), IMIRS (Liang et al., 2002), SAVR (Jiang et al., 2001) and EMAN (Ludtke et al., 1999) that can be used to perform data processing and reconstruction steps. Conceptually, all the software packages use similar principles for image reconstruction. The reconstruction process is iterative, meaning the same procedure is applied to the raw experimental data multiple times, each time producing a slightly improved 3-D model. In the EMAN software suite (Ludtke et al., 1999), the iterative process involves first classifying each of the noisy raw particle images by comparing it to computational projections of the current 3-D model. Corrections to the effects of the contrast transfer function and envelop functions are made for each individual particle images prior to its classification. Classified particles are then rotationally and translationally aligned, and an average image is produced from the experimental data for each projection of the 3-D model. These averages are then used to construct the new 3-D model used for the next iteration of the reconstruction process. This extremely computationally intensive process is continued until the 3-D model is no longer improving. The 3-D model from the last iteration is then the final reconstruction of the specimen.

While the reconstruction represents the structure of the specimen in question, a considerable effort is required to decipher and ana-

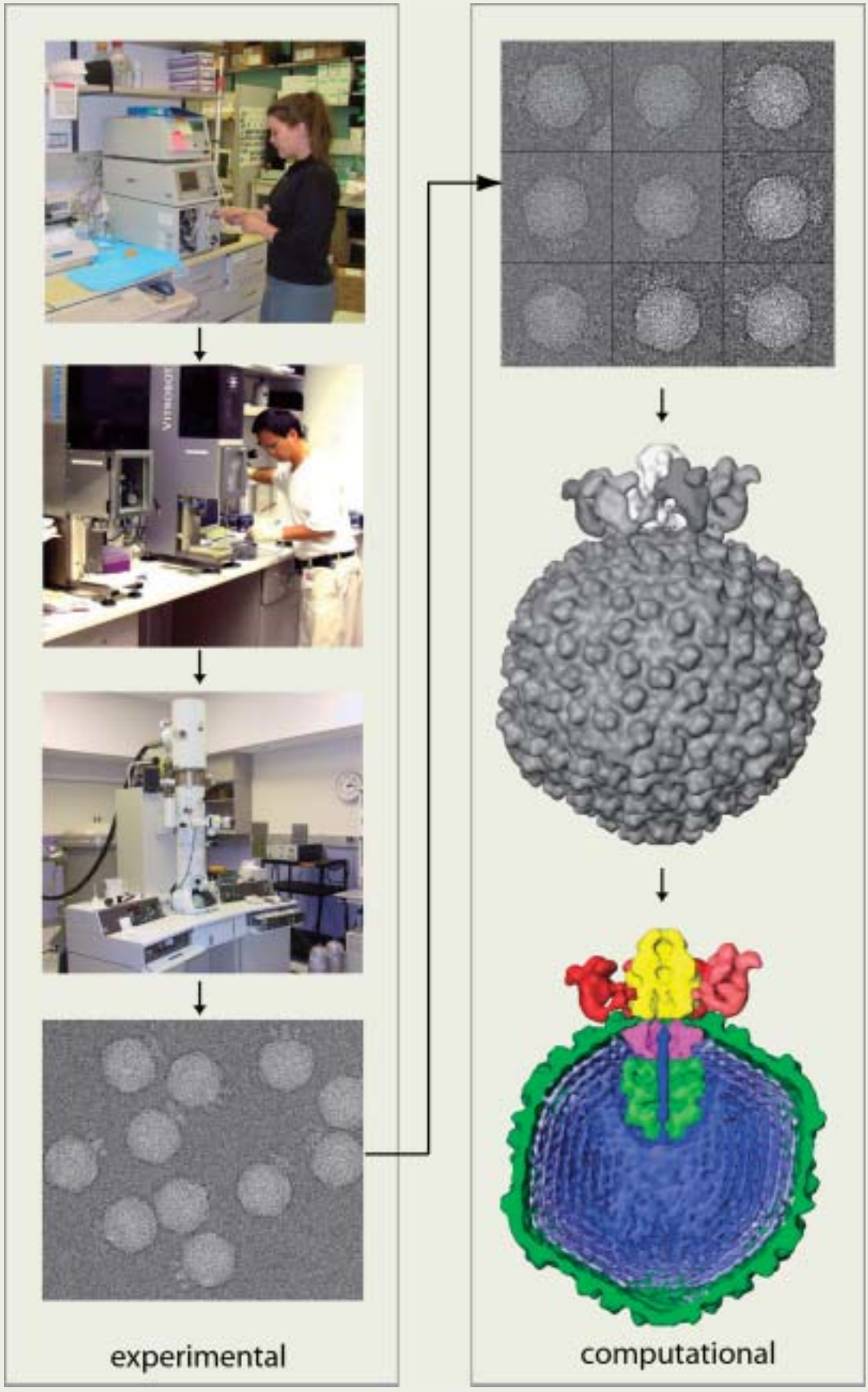

Fig. 2 From sample to model using cryo-EM. Shown is a generic flow diagram illustrating the basic procedure in a cryo-EM experiment. In the first half of the procedure (left panel), the "experimental" portion, the sample is purified, vitrified and imaged, from which raw micrographs or CCD frames of the sample are collected. Once the images have been collected, the data is subjected to the "computational" portion of the experiment which includes image processing, reconstruction, segmentation and analysis as shown on the right panel.

lyze the architecture and composition of the biological nano-machine. As these complexes can be quite large and composed of multiple molecular components, it can be challenging to interpret, let alone just visualize the reconstructed density map at subnanometer resolutions. The first in dissecting the intricate structure of the complex is to identify the individual subunits and segment them from the reconstruction. Again, numerous software packages and approaches are available for this procedure (Bajaj et al., 2003; Baker, 2006; Dougherty and Chiu, 1998; Volkmann, 2002; Yu and Bajaj, 2005). The majority of the approaches rely on the ability to isolate discrete density based by creating a mask and utilizing symmetry information when present. In many instances, the isolation of individual components is a hierarchical procedure, first identifying larger sub-groups of proteins, such as an asymmetric unit in a virus, followed by progressive finer segmentations until individual proteins or small domains have been identified (Baker, 2006).

Once the individual structural components have been isolated, analysis of the individual components can then be done. At subnanometer resolutions, this analysis includes the identification of secondary structure elements and fitting structures into the density map (Chiu et al., 2005; Chiu et al., 2002; Jiang et al., 2001). Additionally, new techniques have begun to arise that utilize the cryoEM density map as a constraint in building structural models (Mitra et al., 2005; Rossmann et al., 2005; Topf et al., 2006). These types of analysis are then combined with traditional genetic, biochemical and bioinformatics analysis to produce "higher resolution" structural models for the individual components. It is plausible that these individual structural models can then be integrated with the cryo-EM refinement, from which a more detailed structural and functional understanding of the complex can be gained.

GroEL, a Protein Folding Machine

With the relatively rapid growth and development of new technology in cryo-EM, it is important to demonstrate the fidelity and limitations in a cryo-EM experiment. For this purpose, it has been necessary to examine a specimen using the cryo-EM pipeline described in **Figure 2** in which the high resolution X-ray crystallographic structure is known. The bacterial chaperonin, GroEL, has been the subject of numerous structural studies by both X-ray crystallography and cryo-EM, including the highest resolution single particle cryoEM reconstruction to date at 6 Å resolution reported today (Ludtke et al., 2004). GroEL, composed of 14 identical subunits and sometimes associated with the capping protein, GroES, is a protein folding machine, with a molecular mass near 1 million Daltons. **Figure 3A** shows an image of frozen, hydrated GroEL recorded on a JEM-2010F cryomicroscope operated at 200 kV equipped with a Gatan cryo-specimen holder and 4 k × 4 k CCD camera. As discussed previously, the image contains particles randomly orientated and thus appears differently in the 2-D images. ~8000 individual GroEL particles were combined and used to compute the 9 Å resolution reconstruction (**Figure 3B**), based on the 0.5 criterion of the Fourier Shell Correlation technique, using the image processing package EMAN (Ludtke et al., 1999). At this resolution, it was possible to dissect and analyze the structure of a GroEL monomer (**Figure 3C**). Using SSEhunter (M. L. Baker, unpublished), individual α-helices greater than two turns were identified in the monomeric subunit (**Figure 3C**). Additionally, large flat density regions, corresponding to β-sheets could be readily identified. To confirm the GroEL structure and the secondary structural analysis, the GroEL X-ray structure (1OEL) (Braig et al., 1994) was fitted to the GroEL density, using FOLDHUNTER (Jiang et al., 2001), and compared (**Figure 3D**). The resulting comparison showed the relative accuracy in identifying nearly all of the secondary structure elements and illustrated the ability of the cryo-EM reconstruction to faithfully capture the native structure of GroEL. As such, the structure and the procedure used to generate the density map and model were validated. Experiments such as this one not only provide the necessary validation of the technique but also provide an excellent way to test new experimental and computational procedures.

Challenges to Higher Resolution

Modern cryo-EM instruments have a resolving power better than 3 Å even with imaging conditions used for the biological nano-machines at moderate magnification and low dose. Therefore, the question becomes if the instrumentation can achieve atomic resolutions, why is it not currently possible to reconstruct density maps to these resolutions? In fact, there are several plausible factors that currently limit high-resolution cryo-EM. First, electron beam induced specimen movement can blur the image anisotropically in a relatively unpredictable manner (Henderson, 2004). Though various attempts have been made to reduce this phenomenon, no general remedy has yet been introduced. Nevertheless, images of frozen, hydrated particles can be recorded in a liquid helium cryomicroscope (JEM-3000SFF) with information contents beyond 6 Å as demonstrated from the visibility of the contrast transfer function rings from the power spectrum of the boxed-out particle images (**Figure 4**). Secondly, inadequacy of the image reconstruction algorithm can result in inaccurate particle orientations and/or improperly correcting the contrast transfer function and envelope function. Furthermore, conformational heterogeneity, due to the dynamic nature of the biological nano-machines, can limit the ability of the reconstruction software to accurately assign orientations and combine them in the 3-D reconstruction. As seen in X-ray crystallography map, different structural regions have different quality, usually referred to as a B-factor. Regions with high B-factors often represent regions of disorder or regions that are highly flexible. As the traditional single particle cryo-EM approach relies on averaging large numbers of individual particles, this type of flexibility, despite the same global structure, would produce reconstructions at resolutions limited by the extent of rigidity of the particle. Computational approaches have begun to address both flexibility and specimen heterogeneity and may result in more accurate and higher resolution structures.

Challenges in cryo-EM are not restricted to specimen, imaging and reconstructing the specimen. As the reconstructions achieve higher resolutions, the density maps grow in size. Current visualization software is capable of interactive visualization; however larger maps are nearing the maximum size and dimensions for standard desktop visualization software. While one would also assume that the subunits are more completely defined and thus easier to segment in higher resolution structures, the fine structural details in this resolution range in fact can blur the boundaries between the subunits and noise. Structural analysis can also be complicated by higher resolution structures. X-ray crystallography and NMR have an extensive repertoire of software designed for building structural models. However, only limited algorithms and applications have been developed by those pushing the resolution envelope in cryo-EM and as such complete packages for structural analysis do not yet exist.

Conclusion

Cryo-EM is a maturing field in structural biology that can determine structures of macromolecular complexes at a broad range of resolutions and can bridge the information gap between cell biology and crystallography/NMR. CryoEM also affords investigators a unique glimpse at these large, dynamic machines, which generally are not amenable to traditional structural approaches. As the field continues to expand, new techniques emerge and conquer previous roadblocks. The past ten years have seen cryo-EM reconstruction improved from 20-30 Å to subnanometer resolutions and now stand poised to achieve near atomic resolution structures in the near future. The realization of this goal will ultimately result in making an impact in our understanding of biological processes and in structure-based drug design against human diseases.

Acknowledgements

We thank the support of grants from NIH (P41RR02250, P01GM064692, PN2EY016525 and P20RR 020647) and NSF (EIA-0325004). The specimens provided by Dr. Jiu-Li Song and Dr. David Chuang at UTSW Medical School and Dr. Peter Weigele and Dr. Jonathan King at MIT are greatly appreciated.

References

- Bajaj, C., Yu, Z., and Auer, M. (2003). Volumetric feature extraction and visualization of tomographic molecular imaging. *J. Struct Biol.*, **144**, 132-143.
- Baker, M. L., Yu, Z., Chiu, W., and Bajaj, C. (2006). Automated segmentation of molecular subunits in electron cryomicroscopy density maps. *J. Struct Biol.*, in press.
- Baker, T. S., and Cheng, R. H. (1996). A model-based approach for determining orientations of biological macromolecules imaged by cryoelectron microscopy. *J. Struct Biol.*, **116**, 120-130.
- Booth, C. R., Jiang, W., Baker, M. L., Zhou, Z. H., Ludtke, S. J., and Chiu, W. (2004). A 9 Å single particle reconstruction from CCD captured images on a 200 kV electron cry-

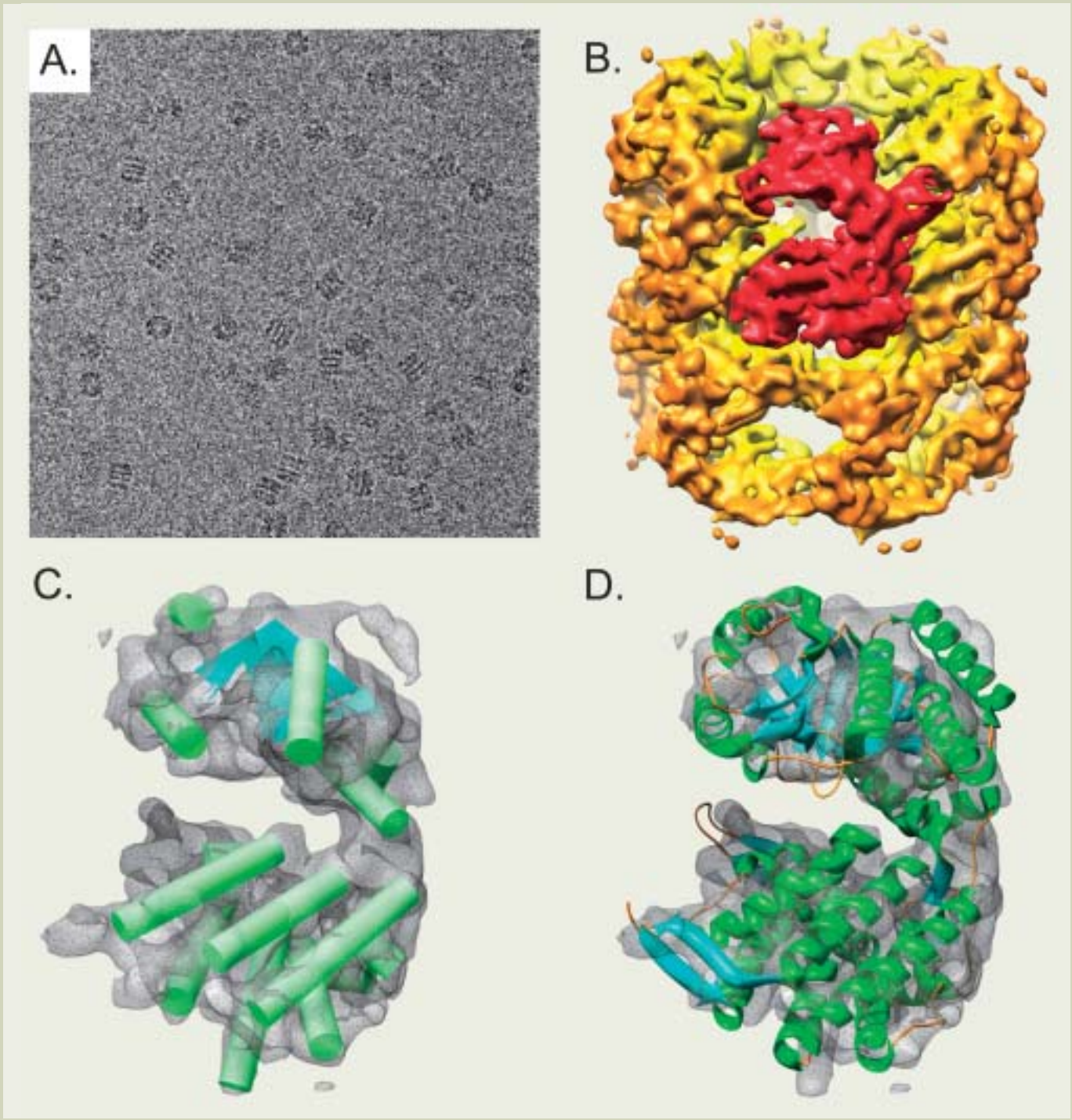

Fig. 3 The 9 Å structure of GroEL. A CCD image of GroEL from the JEOL JEM-2010F is shown in (A). ~8000 individual GroEL particles were used to reconstruct GroEL to 9 Å resolution (tilted side view and top view in (B). A single monomer is highlighted in red. A GroEL monomer was analyzed using SSEhunter, revealing helices and sheets (green and blue, respectively in C). The X-ray crystal structure of GroEL (1OEL) was fitted to the density corresponding to a single GroEL monomer using FOLDHUNTER, thus illustrating the effectiveness and accuracy of cryo-EM imaging (D).

omicroscope. *J. Struct Biol*., **147**, 116-127.
- Braig, K., Otwinowski, Z., Hegde, R., Boisvert, D. C., Joachimiak, A., Horwich, A. L., and Sigler, P. B. (1994). The crystal structure of the bacterial chaperonin GroEL at 2.8 Å. *Nature*, **371**, 578-586.
- Chiu, W., Baker, M. L., and Almo, S. C. (2006). Structural biology of cellular machines. *Trends Cell Biol.*, **16**, 144-150
- Chiu, W., Baker, M. L., Jiang, W., Dougherty, M., and Schmid, M. F. (2005). Electron cryomicroscopy of biological machines at subnanometer resolution. *Structure*, **13**, 363-372.
- Chiu, W., Baker, M. L., Jiang, W., and Zhou, Z. H. (2002). Deriving folds of macromolecular complexes through electron cryomicroscopy and bioinformatics approaches. *Curr Opin Struct Biol.*, **12**, 263-269.
- Crowther, R. A., Henderson, R., and Smith, J. M. (1996). MRC image processing programs. *J. Struct Biol*., **116**, 9-16.
- Dougherty, M. T., and Chiu, W. (1998). Using animation to enhance 3D visualization: a strategy for a production and environment. *Microsc and Microanal*., **4**, 452-453.
- Dubochet, J., Adrian, M., Chang, J. J., Homo, J. C., Lepault, J., McDowall, A. W., and Schultz, P. (1988). Cryo-electron microscopy of vitrified specimens. *Q Rev Biophys*., **21**, 129-228.
- Frank, J. (2002). Single-particle imaging of macromolecules by cryo-electron microscopy. *Annu Rev Biophys Biomol Struct.*, **31**, 303-319.
- Frank, J., Radermacher, M., Penczek, P.,

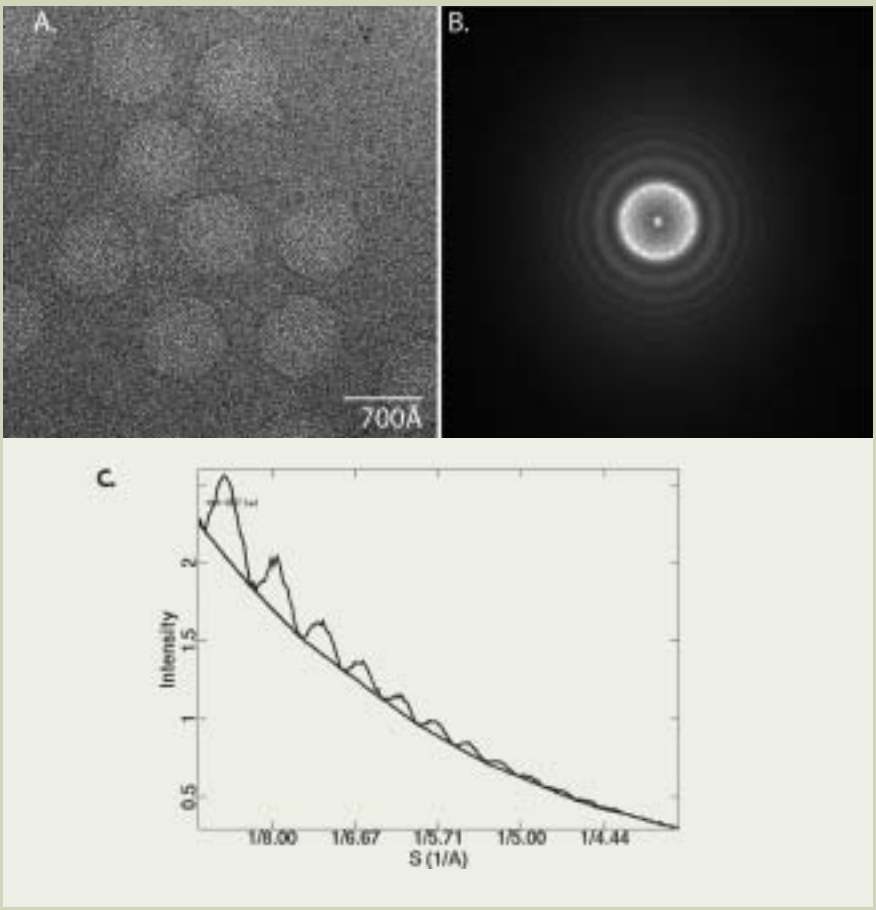

Fig. 4 Imaging Epsilon 15 bacteriophage. A micrograph at 1.3 µm defocus of Epsilon 15 from the JEOL JEM-3000SFF operated at 300 kV and specimen at 4.2 K (A). FFT power spectrum of the boxed out particle images are shown (B). A circularly averaged power spectrum is shown in (C) to show the oscillations of the contrast transfer function rings above a fitted background curve beyond 6 Å.

Zhu, J., Li, Y., Ladjadj, M., and Leith, A. (1996). SPIDER and WEB: processing and visualization of images in 3D electron microscopy and related fields. *J. Struct Biol*., **116,** 190-199.

- Fuller, S. D. (2003). Depositing electron microscopy maps. Structure (camb) **11**, 11-12.
- Gavin, A. C., Aloy, P., Grandi, P., Krause, R., Boesche, M., Marzioch, M., Rau, C., Jensen, L. J., Bastuck, S., Dumpelfeld, B., *et al.* (2006). Proteome survey reveals modularity of the yeast cell machinery. *Nature.*, **440**, 631-638.
- Grigorieff, N. (1998). Three-dimensional structure of bovine NADH:ubiquinone oxidoreductase (complex I) at 22 A in ice. *J. Mol Biol*., **277**, 1033-1046.
- Henderson, R. (2004). Realizing the potential of electron cryo-microscopy. *Quart Rev Biophys.*, **37**, 3-13.
- Jiang, W., Baker, M. L., Ludtke, S. J., and Chiu, W. (2001). Bridging the information gap: computational tools for intermediate resolution structure interpretation. *J. Mol Biol.*, **308**, 1033-1044.
- Jiang, W., and Chiu, W. (2006). Cryo-electron microscopy of icosahedral virus particles, In Methods in Mol. Biol., J. Kuo, ed. (Totowa, NJ: The humana press), in press.
- Jiang, W., and Ludtke, S. J. (2005). Electron cryomicroscopy of single particles at subnanometer resolution. *Curr Opin Struct Biol*., **15**, 571-577.
- Krogan, N. J., Cagney, G., Yu, H., Zhong, G., Guo, X., Ignatchenko, A., Li, J., Pu, S., Datta, N., Tikuisis, A. P., *et al*. (2006). Global landscape of protein complexes in the yeast Saccharomyces cerevisiae. *Nature*, **440**, 637-643.
- Liang, Y., Ke, E. Y., and Zhou, Z. H. (2002). IMIRS: a high-resolution 3D reconstruction package integrated with a relational image database. *J. Struct Biol*., **137**, 292-304.
- Ludtke, S. J., Baldwin, P. R., and Chiu, W. (1999). EMAN: semiautomated software for high-resolution single-particle reconstructions. *J. Struct Biol*., **128**, 82-97.
- Ludtke, S. J., Chen, D. H., Song, J. L., Chuang, D. T., and Chiu, W. (2004). Seeing GroEL at 6 Å resolution by single particle electron cryomicroscopy. *Structure*, **12**, 1129-1136.
- Martin, A. C., and Drubin, D. G. (2003). Impact of genome-wide functional analyses on cell biology research. *Curr Opin Cell Biol.*, **15**, 6-13.
- Mitra, K., Schaffitzel, C., Shaikh, T., Tama, F., Jenni, S., Brooks, C. L., Ban, N., and Frank, J. (2005). Structure of the E. coli protein-conducting channel bound to a translating ribosome. *Nature*, **438**, 318-324.
- Rossmann, M. G., Morais, M. C., Leiman, P. G., and Zhang, W. (2005). Combining X-ray crystallography and electron microscopy. *Structure*, **13**, 355-362.
- Serysheva, I. I., Chiu, W., and Ludtke, S. J. (2006). Single particle electron cryomicroscopy of the ion channels in the excitation-contraction coupling junction, In Methods in Cell Biol, Cellular Electron Microscopy, J. R. McIntosh, ed. (San Diego: academic press), in press.
- Sorzano, C. O., Marabini, R., Velazquez-Muriel, J., Bilbao-Castro, J. R., Scheres, S. H., Carazo, J. M., and Pascual-Montano, A. (2004). XMIPP: a new generation of an open-source image processing package for electron microscopy. *J. Struct Biol*., **148**, 194-204.
- Topf, M., Baker, M. L., Marti-Renom, M. A., Chiu, W., and Sali, A. (2006). Refinement of protein structures by Iterative comparative modeling and cryoEM density fitting. *J. Mol Biol.*, **357**, 1655-1668.
- van Heel, M., Harauz, G., Orlova, E. V., Schmidt, R., and Schatz, M. (1996). A new generation of the IMAGIC image processing system. *J. Struct Biol.*, **116**, 17-24.
- Volkmann, N. (2002). A novel three-dimensional variant of the watershed transform for segmentation of electron density maps. *J. Struct Biol*., **138**, 123-129.
- Yu, Z., and Bajaj, C. (2005). Automatic ultrastructure segmentation of reconstructed cryo-EM maps of icosahedral viruses. IEEE Transactions on Image Processing. **14**, 1324-1337.

Intracellular Transport and Kinesin Superfamily Proteins, KIFs: Genes, Structure, Dynamics, Functions and Diseases

Nobutaka Hirokawa

Department of Cell Biology and Anatomy, Graduate School of Medicine, University of Tokyo

Introduction

Cells transport and sort various proteins and lipids following synthesis as distinct kinds of membranous organelles and protein complexes to the correct destinations at appropriate velocities. The intracellular transports are fundamental for cell morphogenesis, functioning and survival not only in polarized cells such as neurons and epithelial cells but also in all other cells. To elucidate this mechanism, we have identified kinesin superfamily proteins, KIFs based on the discovery of various kinds of crossbridges between microtubules and membranous organelles (**Fig. 1**) [1-6] and been characterizing KIFs using molecular cell biology, molecular genetics, biophysics, X-ray crystallography and cryoelectron microscopy. Recently we have identified all KIFs genes in mammals such as mice and human [27]. In this manuscript, I present our recent studies about the structure, dynamics and functions of KIF1A, KIF1Bβ, KIF17, KIF5s, KIF3, KIF2A and KIF4. Especially I focus on our works to reveal how the molecular motors move on microtubules processively.

Discovery of Kinesin Superfamily Motor Proteins, KIFs and Elucidation of their Functions

KIF1A, KIF1Bβ, KIF17, KIF5s, KIF2A and KIF4 are deeply involved in neuronal functions, network formation and activity dependent neuronal survival during development. KIF1A and KIF1Bβ are unique monomeric motors transporting synaptic vesicle precursors and play essential roles on neuronal function and survival (**Figs. 2**, **3**, **4A**) [6, 11, 19, 29]. Molecular genetic study revealed that KIF1Bβ is a responsible gene of a human hereditary neuropathy [29]. KIF1Bα and KIF5 transport mitochondria from the cell body to periphery [9, 20]. KIF17 conveys NMDA type glutamate receptors, important for memory and learning, in dendrites through the interaction with scaffolding protein complex and NR2B subunit of NMDA receptors (**Fig.s 4A**, **B**)[24, 32]. Transgenic mice study showed that overexpression of KIF17 improved spatial and working memory [31]. On the other hand, conventional kinesin (KIF5) transports AMPA type glutamate receptors in dendrites via GRIP1 and GluR2 interaction (**Fig.s 4A**, **B**)[30].

The middle motor domain type KIF2A is fundamental for correct wiring of brain by suppressing elongation of axon collaterals through depolymerizing microtubules in growth cones (**Fig. 4A**)[6, 10, 33]. Recently using X ray crystallography of KIF2C at ADP state and ATP like state, we have elucidated how unique KIF2 depolymerizes microtubules at their ends [35].

KIF3 is ubiquitously expressed [6, 7, 13, 16]. Our gene targeting studies demonstrated that KIF3 is essential for determination of left-right asymmetry of our body through formation of monocilia of node cells which rotate and generate leftward flow of extra embryonic fluid, nodal flow. This nodal flow is critical to turn on switches of a gene cascade expressed strictly at left side, and determines left-right asymmetry. Our recent studies finally uncovered the morphogens which are conveyed toward left and play critical roles on L/R determination [39, 40]. Actually vesicles containing Shh and retinoic acid are released from nodal cells dependently on the FGF signaling and conveyed to the left by the nodal flow [39]. Thus, KIF3 is essential for left-right determination of our body [42].

Conditional gene targeting study of KAP3, an associated protein of KIF3 motor complex, caused suppression of KIF3 function and revealed that hyper proliferation of progenitor cells in the neuroepithelium occurred and resulted in formation of brain tumors [41]. This is because KIF3 suppresses tumorigenesis by transporting N cadherin-β catenin complex from Golgi to the plasma membrane which works as a transcriptional factor with T cell factor and enhances cell proliferation as a signaling molecule down stream of Wnt canonical pathway in the nucleus [41].

KIF4 controls the activity-dependent survival of postmitotic neurons by regulating PARP-1 activity in brain development. In brain development [6, 8, 43], apoptosis is a physiological process that controls the final numbers of neurons. The C-terminal domain of KIF4 is a module that suppresses the activity of poly(ADP-ribose)polymerase-1(PARP-1), a nuclear enzyme known to maintain cell homeostasis by repairing DNA and serving as a transcriptional regulator. When neurons are stimulated by membrane depolarization, calcium signaling mediated by CaMKII induces dissociation of KIF4 from PARP-1, resulting in upregulation of PARP-1 activity, which supports neuron survival. After dissociation from PARP-1, KIF4 enters into the cytoplasm from the nucleus and moves to the distal part of neurites in a microtubule-dependent manner [43]. This suggested that KIF4 controls the activity-dependent survival of postmitotic neurons by regulating PARP-1 activity in brain development [43].

Our very recent study unraveled also that KIF5 transports mRNAs such as CaMKIα mRNA and Arc mRNA in dendrites through the interaction of KIF5 tail and a large RNA-Transporting protein complex (~1000s) containing hnRNP-U, Pur α and β, PSF, DDX1, DDX3, SYNCRIP TLS, NonO, HSPC117, ALY, CGI-99, Staufen, three FMRPs and EF1α (**Fig.4A**, **B**)[37].

Thus, KIFs play a number of significant roles not only on various cell functionings by transporting important membranous organelle, protein complexes, and mRNAs but also play unique and important functions on fundamental developmental events such as left-right asymmetry, brain wiring, activity dependent

University of Tokyo, Tokyo, Japan 113-0033.
e-mail : hirokawa@m.u-tokyo.ac.jp

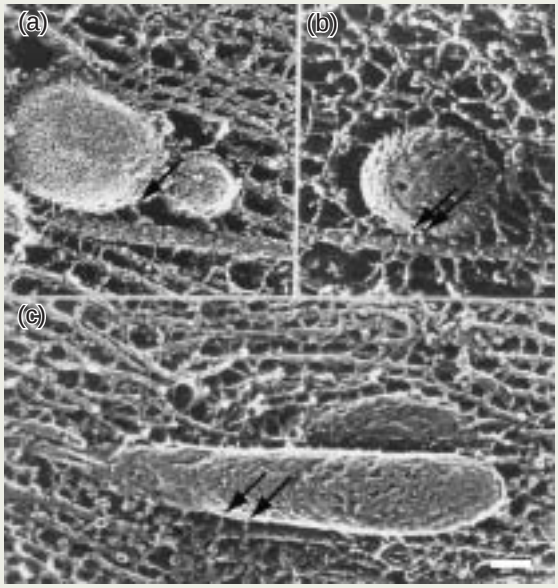

Fig. 1 Quick-frozen, deep-etched axons in which various types of crossbridge (arrows) are identified between membranous organelles and microtubules.
(a) A crossbridge (arrow) composed of two heads and a long stalk (~25 nm).
(b) Only globular heads (arrows) are recognizable between a membranous organelle and a microtubule.
(c) Crossbridges (arrows) between mitochondria and microtubule are short and have small heads. Bar, 50 nm. Reproduced with permission from Hirokawa [14].

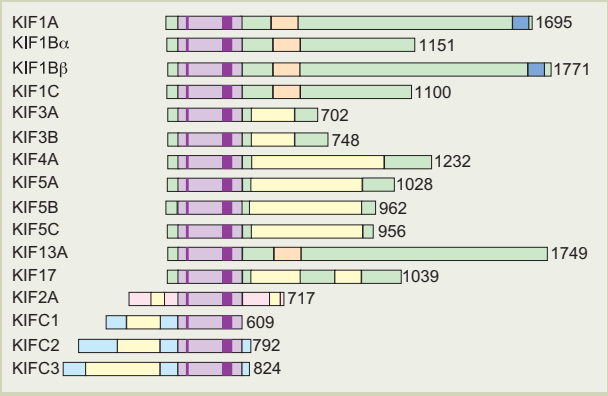

Fig. 2 The domain structures of principal KIFs. The motor domains are shown in purple. The ATP-binding consensus sequence is indicated by a thin red line and the microtubule-binding consensus sequence by a thick red line. The dimerization domains, forkhead-associated domains and pleckstrin homology domains are shown in yellow, orange, and dark blue respectively. The number of amino acids in each molecule is shown on the right. N-kinesins are shown in green, M-kinesin in pink and C-kinesin in pale blue.

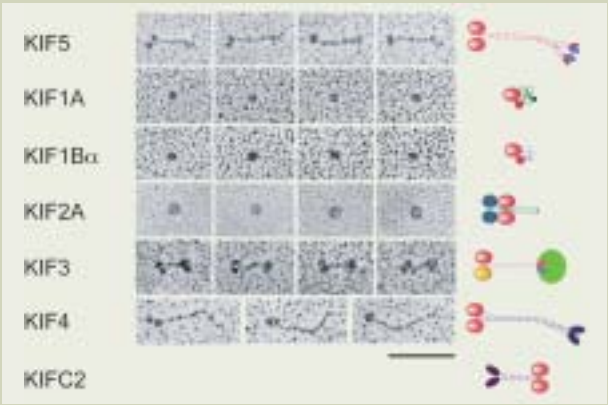

Fig. 3 Principal members of KIFs observed by low-angle rotary shadowing. Diagrams, constructed on the basis of electron microscopy or predicted from the analysis of their primary structures, are shown on the right (the large red ovals in each diagram indicate motor domains). Reproduced with permission from Hirokawa [18]. Scale bar, 100 nm.

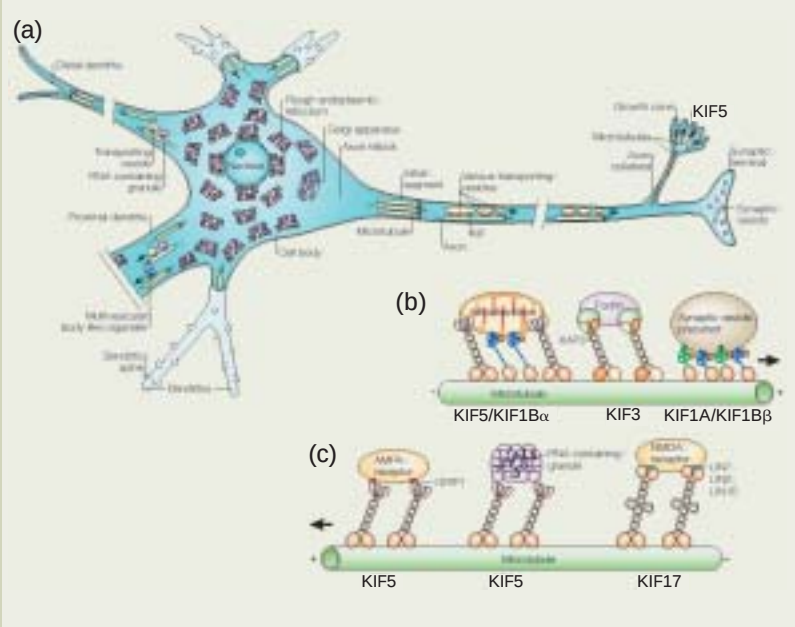

Fig. 4A **(a)** A typical neuron, extending several dendrites (left) and a single thin axon (right) from the cell body. In the axon, microtubules are unipolar, with the plus ends pointing towards the synaptic terminal. Microtubules form special bundles at the initial segment, which might serve as the cue for axonal transport. Tubulovesicular organelles are transported anterogradely along microtubules by KIFs. In the growth cone of an axon collateral, KIF2A controls microtubule dynamics and the extension of collaterals. Rough endoplasmic reticula are abundant in most parts of the cell body, except for the axon hillock. Dendrites contain some rough endoplasmic reticlula. Microtubules have mixed polarity in proximal dendrites, but are unipolar in distal dendrites, with the plus end pointing away from the cell body. Membranous organelles and RNA-containing granules are transported along microtubules by KIFs.
(b) Mitochondria are transported by KIF5 and KIF1B. KIF3 transports vesicles associated with fodrin. KIF1A and KIF1B both transport synaptic vesicle precursors. KAP3, kinesin superfamily-associated protein 3.
(c) In dendrites, KIF5 transports vesicles containing AMPA (-amino-3-hydroxy-5-methyl-4-isoxazole propionic acid) receptors through an interaction between KIF5 and GRIP1 (glutamate receptor-interacting protein 1). RNA-containing granules are also transported by interacting directly with KIF5. KIF17 transports vesicles containing NMDA (*N*-methyl-D-aspartate) receptors by interacting through the LIN complex, a tripartite protein complex containing mammalian homologues of the *Caenhorhabditis elegans* presynaptic density zone (PDZ) proteins LIN-2, LIN-7 and LIN-1065. Reproduced with permission from Hirokawa and Takemura [42].

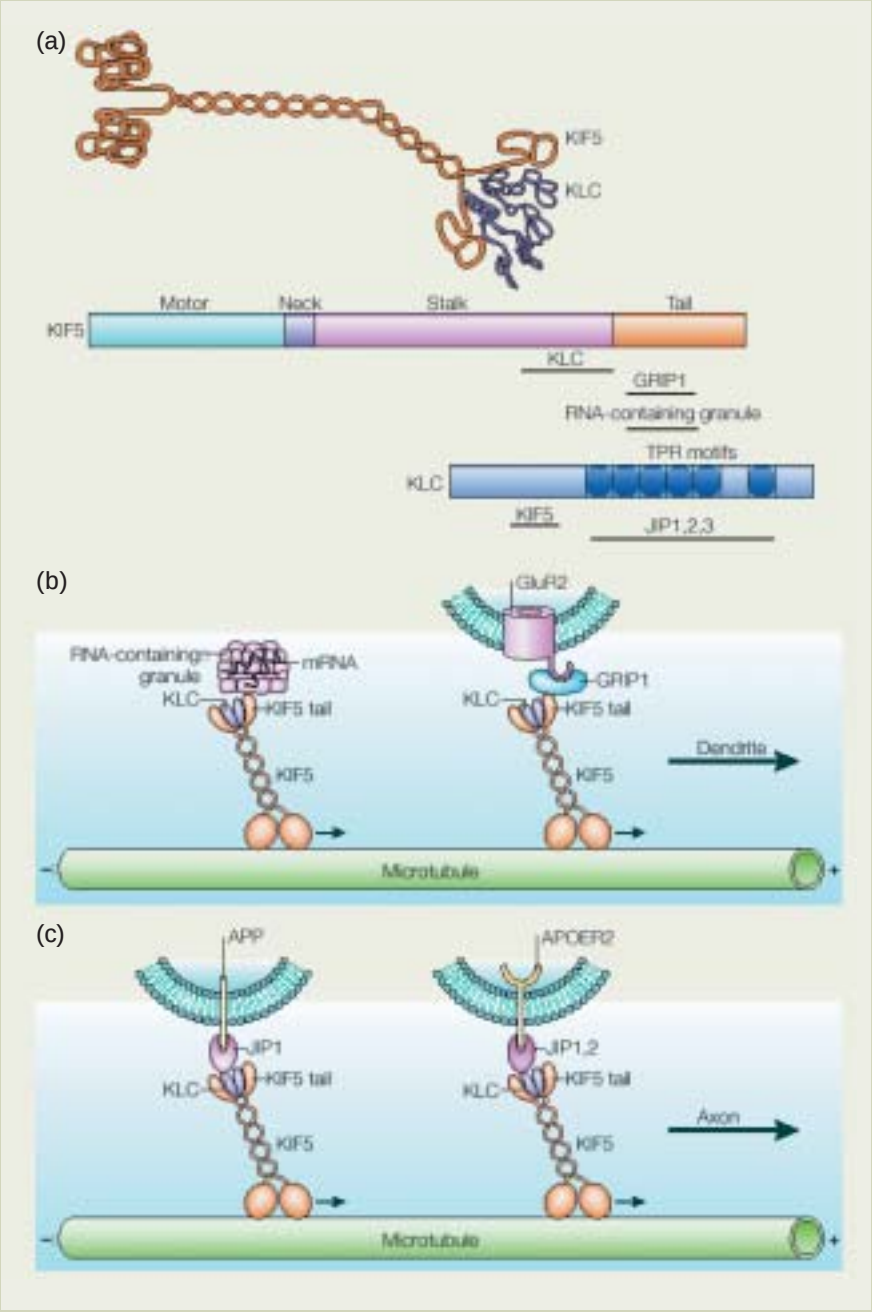

Fig. 4B **(a)** Schematic model and binding domains of KIF5 and kinesin light chain (KLC). Top, schematic model of KIF5 associating with KLC. The KIF5 dimer associates with two KLCs to form a heterotetramer. The globular motor domains of KIF5 are shown on the left, followed by the neck, stalk and carboxy (C)-terminal tail, with which KLC associates to form fanlike ends. Middle, the domain structures of KIF5 and binding sites for KLC, GRIP1 (glutamate receptor-interacting protein 1) and RNA-containing granules. KIF5 consists of motor, neck, stalk and tail domains. The binding site for KLC is near the C-terminal end of the stalk region (amino acids 775–802); those for GRIP1 and RNA-containing granules are in the C-terminal tail (amino acids 807–934 and 865–923, respectively). The C-terminal tail cargo-binding site of KIF5 overlaps with the cargo-binding site of fungus KIF, which lacks KLC. Bottom, the domain structure of KLC and the binding sites for KIF5 and JIPs (scaffolding proteins of the c-Jun amino (N)-terminal kinase (JNK) signalling pathway). KLC contains six TPR (tetratricopeptide repeat) motifs. The binding site for KIF5 is in the N-terminal portion of KLC and JIPs bind to the TPR motifs.
(b) The C-terminal tail of KIF5 binds RNA-containing granules (left) and AMPA (-amino-3-hydroxy-5-methyl-4-isoxazole propionic acid) receptor subunit GluR2-containing vesicles (right), and transports them to dendrites. The direct binding partner of RNA-containing granules is unknown. Binding to the C-terminal tail of GluR2 is mediated by GRIP1.
(c) The TPR motif of KLC binds to JIPs and transports APP (amyloid precursor protein)- and APOER2 (apolipoprotein E receptor 2)-containing vesicles to axons. The phosphotyrosine-binding domain of JIPs interacts with APOER2 and APP. However, it has also been proposed that APP binds directly to KLC. Reproduced with permission from Hirokawa and Takemura [42].

neuronal survival, suppression of tumorigenesis and higher brain functions such as memory and learning [14, 18, 38].

How the Molecular Motor Moves on the Microtubules Processively

Here, we discuss the mechanism underlying motor motility. We identified KIF1A motor, which exists as a monomer in solution [6, 11]. It was an important finding because all the motors that had been identified before KIF1A are dimeric two-headed motors; for example, myosins that move along actin filaments, dyneins that generate the movements of cilia or flagella, or conventional kinesin. Therefore, the "walking" model or a "hand-over-hand" model is a widely accepted model of the processive movement, that is the movement of motor molecules along the rail without detaching for some distance (**Fig. 5**)[44]. In other words, it had been widely accepted that a motor needs two legs, just like when we walk. When one foot steps forward, the other foot needs to be firmly attached to the rail for a motor to be able to "walk" without detaching from the rail. With this theory, a single-headed motor molecule is not expected to move processively along the rail, because a single-headed motor would dissociate from the rail when it steps forward [45, 46].

Processive biased Brownian movement of KIF1A

To determine whether KIF1A is a processive motor, we produced the shortest motor domain construct of the KIF1A molecule, C351, and labeled it with a fluorescent Alexa dye. A similar construct was produced for conventional kinesin [22]. We constructed a low-background video-intensified microscope and then visualized the behavior of single molecules, that is, their dynamics. It was revealed that a single KIF1A molecule moves along a microtubule processively over a distance of more than 1 μm (**Figs. 6a** and **6b-C** shaded bar). The movement of single C351 molecules on the microtubule is not smooth, and actually appears to be oscillatory (**Figs. 6a** and **6b-D**). Although on average they move unidirectionally, a single C351 molecule sometimes pauses for a while, or moves backward for a short distance, and then forward. To quantitatively analyze this apparently oscillatory movement, the distribution of displacement was plotted (**Fig. 6b-F**). The plot fitted well with a normal distribution whose mean and variance increased linearly against time. The linear increase of mean indicates a unidirectional constant-velocity movement on average. The linear increase of variance indicates a linear accumulation of random noise, as observed in Brownian movement [47]. Thus, the distribution of the displacement of C351 suggests that it was a biased Brownian movement. In contrast, a dimeric conventional kinesin molecule, K381, moves smoothly unidirectionally (**Figs. 6b-E** and **6b-C** open bar). The distribution of its displacement fitted well with a normal distribution with linearly increasing mean and a constant variance (**Fig. 6b-G**). The latter can be explained by the error in position measurement.

We further analyzed the movement of C351 and K381 by plotting mean square displacement ([MSD, ρ (t)]) against time, which is a convenient quantitative measure of stochastic movement (**Fig. 6b-H**). The MSD plot of C351 (**Fig. 6b-H** open circle) fitted well with biased Brownian movement,

$$\rho(t) = 2Dt + v^2t^2, \qquad (1)$$

where D is the diffusion coefficient and v is the mean velocity. The MSD plot of C351 fitted well with

$$D = 44{,}000 \pm 1200 \text{ nm}^2/\text{s} \qquad (2)$$

and

$$v = 140 \pm 10 \text{ nm/s}. \qquad (3)$$

The estimated value of D is much larger than the value expected from fluctuation in ATPase activity (<2400 nm^2/s), but it is in good agreement with the value previously reported for one-dimensional Brownian movement in microtubule-motor protein systems. In contrast, the MSD plot of K381 (**Fig. 6b-H** closed square) fitted well with

$$D = 2200 \pm 1000 \text{ nm}^2/\text{s} \qquad (4)$$

and

$$v = 710 \pm 10 \text{ nm/s}, \qquad (5)$$

and the fluctuation in K381 movement can be explained by the fluctuation in ATPase activity.

The difference in the degree of fluctuation of movement between C351 and K381 is illustrated by the plot of the diffusion term,

$$\rho(t) - v^2t^2. \qquad (6)$$

The movement of C351 is about 20 times as diffusive as K381 (**Fig. 6b-I**). This heavily stochastic nature of the movement cannot be explained by the error of position measurement or the Brownian noise, because these cannot accumulate and only contribute as constant terms to the diffusion term of MSD or the variance of displacement. Furthermore, our single-motor assay is free from the Brownian noise because the position of a fluorescent spot directly reflects the position of a motor molecule. These results are the first clear experimental demonstration that a motor could move by a biased Brownian movement.

"K-loop" is essential for processivity

The next question is why a one-headed monomeric motor can move processively along microtubules without detaching. It was suggested that the binding between motor and microtubule is mediated by electrostatic interactions. The microtubule surface is mainly negatively charged; therefore, we thought that KIF1A might have a highly positively charged region and we attempted to identify this region. We found a region with five lysines in tandem, and named this region the "K-loop" [22]. We considered that this highly positively charged region may play important roles and we confirmed it to be so. When mutants that have fewer lysines in the K-loop were produced, the processivity of the motor decreases, as determined by single-motor motility assay [48]. In other words, the duration of movement

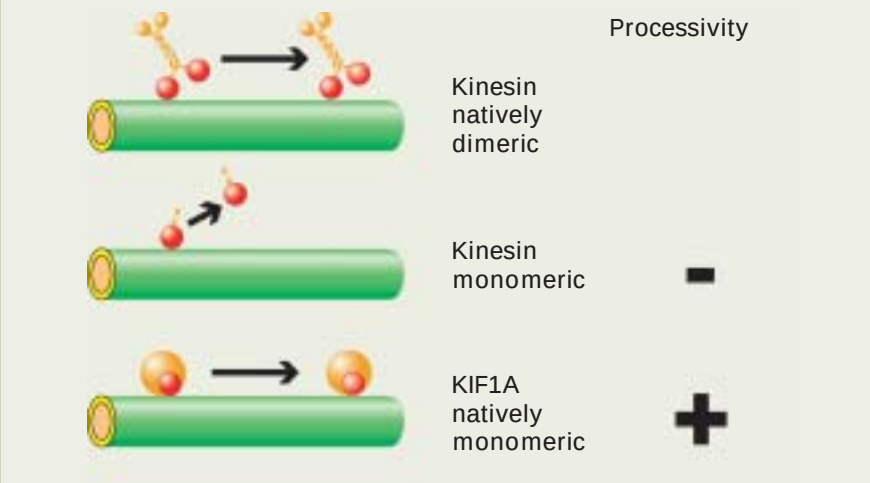

Fig. 5 Processivity of movement of monomeric motor along microtubules. Conventional kinesin is dimeric in its native form. It moves processively along microtubules in the dimeric forms, but not in the monomeric form. In contrast, KIF1A is monomeric in its native form and moves processively in the monomeric form.

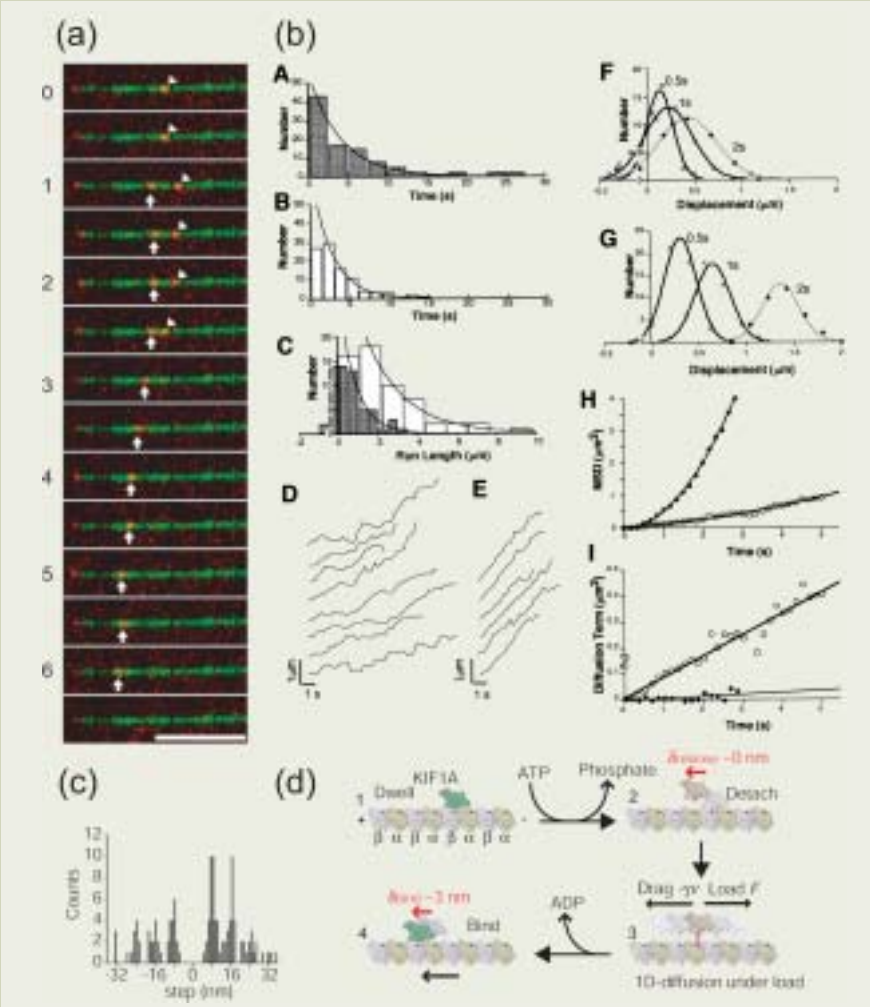

Fig. 6 Processive movement of monomeric motor KIF1A.
(a) Movement of fluorescently labeled single C351 molecules (red) along microtubule (green). Sometimes C351 moves backward (arrowhead), but it usually moves in one direction (arrow). Scale bar, 2 μm; frame interval, 0.5 s.
(b) Analysis of movement. Distribution of duration of movement of C351 (A) and K381 (B). Distribution of run length of C351 (shaded bar) and K381 (open bar) (C). Typical traces of displacement of C351 (D) and K381 (E). Distribution of displacement of C351 (F) and K381 (G). MSD of C351 (○) and K381 (◆) plotted against time (H). Diffusion term of C351 (○) and K381 (◆) plotted against time (I).
(c) Distribution of step size of KIF1A beads measured by optical trapping.
(d) Flush ratchet model of KIF1A movement along microtubule. Panels (a and b) reproduced with permission from [23]. Panels (c and d) reproduced with permission from Okada and Hirokawa [22].

along a microtubule becomes shorter for the mutant KIF1A. The turnover rates (k_{cat}) of these mutants are the same level as that of the original construct, but $K^{0.5}_{MT(ATPase)}$ (microtubule concentration for half-saturation of ATPase), which is a measure of the average affinity to microtubule throughout the ATPase cycle, is significantly affected.

The time constant of the mechanical processivity (τ_{mec}) of C351 determined by single-molecule-motor assay is 6.1 ± 0.8 s (**Fig. 6b-A**), which agrees well with the time constant of kinetic processivity (τ_{kin}) of 6.3 s determined by microtubule-activated ATPase assay. In comparison, the time constant of the mechanical processivity of K381 (τ_{mec}) is 2.6 s and that of kinetic processivity (τ_{kin}) is 2.0 s (**Fig. 6b-B**), that is, about one-third of those of C351, indicating that monomeric KIF1A has a higher processivity than dimeric conventional kinesin.

The kinetic index of processivity, which indicates the number of ATPase cycles per motor-microtubule encounter, is 690 for C351. On average, C351 hydrolyzes nearly 700 ATPs before detaching from the microtubule. This is more than five times the number of ATPs hydrolyzed by the dimeric kinesin K381, and more than 40 times that hydrolyzed by the monomeric kinesin K351.

Biased stepwise movement during ATP hydrolysis cycle

We then analyzed the detail of movement by optical trapping nanometry [34]. For this, we attached a 0.2-μm-diameter bead to one end of a monomeric KIF1A construct, which contains almost solely the motor head domain and cannot dimerize. We then placed the beads on a polarity-marked microtubule fixed to a coverglass and performed optical trapping, that is, by pulling a bead with a laser beam, the optical tweezer, the movement of KIF1A is amplified as the movement of the bead.

A region called the "neck linker" at the C-terminus of the motor domain is proposed to play important roles in the motility of conventional kinesin [45, 49]. To determine whether this is the case for the biased Brownian movement of KIF1A, a bead was attached to the N-terminus or C-terminus of the KIF1A motor domain. We also attached KIF1A to beads using methods that prevent dimerization. Binding beads at the N-terminus or C-terminus of KIF1A does not make any difference in the results of optical trapping nanometry; therefore, this indicates that the neck linker does not significantly contribute to at least motility based on biased Brownian movement.

The KIF1A attached beads showed a clear bidirectional stepwise movement. In addition, it was shown that a single ATP hydrolysis produces a single mechanical step. Furthermore, it was shown that the step size is not fixed, but distributed approximately in multiples of 8 nm (**Fig. 6c**). The histogram shows that the step size is distributed in both the directions of plus and minus ends, but step sizes are all in multiples of 8 nm. Therefore, the beads moved backward and forward in step sizes of multiples of 8 nm, but the net direction of the bead movement is towards the plus end, indicating biased Brownian movement. Because the size of the tubulin monomer is 4 nm and that of the heterodimer is 8 nm, the microtubule is predicted to have high affinity sites every 8 nm.

Next, to analyze at which steps the movement is biased towards the plus end, the movement was observed in the presence of ATP at a low concentration. The analysis showed that in the ADP-bound state, KIF1A was in Brownian motion, and when it released ADP and had no nucleotides, it bound tightly to the microtubule. At that moment, KIF1A moved towards the plus end by about 3 nm on average. This average distance of 3 nm is explained as follows. If a motor moves twice towards the plus-end over a distance of 8 nm and once towards the minus end over a distance of 8nm once, the net distance it moved is 8 nm towards the plus end. However, it took three steps to make that movement. If 8 nm is divided by 3, the average movement of 2.66 nm per step is obtained. Therefore, KIF1A always moves at step sizes of multiples of 8 nm, but it moves towards the plus end over a distance of 3 nm on average. It was also demonstrated that when ADP is released, KIF1A makes a biased movement towards the plus end. In summary, the optical trapping showed that KIF1A is in Brownian movement in the ADP-bound state, and when ADP is released, it moves towards the plus end over a distance of 3 nm on average (**Fig. 6d**). This model also agrees well with the results of X-ray crystallography analysis, but we will discuss it later.

K-loop/E-hook interaction sustain Brownian movement in weak-binding state - Tarzan model

We also studied the mechanism of biased Brownian movement by cryoelectron microscopy [12, 23]. The motor domain of KIF1A, C351, was bound to the microtubule in an ATP-like strong binding state and its structure was studied by cryoelectron microscopy at 15Å resolution. In a state bound to a nonhydrolyzable analog of ATP, AMP-PNP, the KIF1A motor domain bound to microtubule protofilament like koala with three binding sites, namely MB1, MB2, and MB3 (**Figs. 7a** and **c**). When this was compared with conventional kinesin, a unique feature of KIF1A was found to be the high prominence of MB3. The next step was to determine which primary sequences, that is, amino acid sequence, form the MB1, MB2, and MB3 binding sites.

The X-ray crystallographic atomic structure of KIF1A was not available at the time, therefore, the available conventional kinesin atomic model was docked. Because the amino acid sequence of the motor domain of KIF1A have 60% similarity to that of conventional kinesin, certain parts would fit and others would not, revealing the differences. The docking showed that MB3 corresponded to the loop L12, that is, the K-loop region, and MB1 and MB2 corresponded mainly to L8 and L11.

When the tubulin atomic model was also docked, another important feature was revealed, that is the flexible C-terminus of tubulin can interact with the K-loop. This was confirmed by the cleavage of the C-terminus of tubulin [48]. Because this C-terminal region contains many glutamates (E in one-letter code), we named this region the "E-hook" [48]. It was also suggested that the interaction between the E hook and K loop is specifically important in the ADP-bound state. Furthermore, to directly show that the K-loop corresponds to MB3, we labeled the K loop with colloidal gold cluster by introducing reactive cysteine and examined it by cryoelectron microscopy. The gold-cluster labeling unambiguously proved that MB3 contains the K loop.

From these studies, we would like to propose a model for the biased Brownian movement of KIF1A called the Tarzan model (**Fig. 7d**). Tarzan is the KIF1A motor domain, and it is stretching its arm, the K-loop, upwards and grabbing a tether that hangs from the microtubule protofilaments composed of α- and β-tubulin. The tether is the flexible C-terminal E hook of tubulin. In the ADP-bound state, Tarzan does the Brownian motion via the interaction between the K loop and E-hook. Drag force, diffusion, might reflect the fluctuation of the flexible tether between KIF1A's K loop and tubulin's E hook. Upon the hydrolysis of ATP, Tarzan releases the tether and grabs another tether, but in doing so, movement has bias towards the plus end.

Conformational changes in switch I and II during ATP hydrolysis

We then studied how the bias works by examining ATP hydrolysis steps by X-ray crystallography and cryoelectron microscopy (**Fig. 8**)[28]. First, the ADP-bound state and AMP-PCP-bound state of KIF1A were studied. The AMP-PCP state is considered to represent one of the ATP-like-states called preisomerization. X-ray crystallography revealed that switch I and II regions, which form a nucleotide-binding pocket interposed with the bridging water molecule and hydrogen bonds, show marked conformational changes. First, the switch I region forms a short β-hairpin structure in the ATP-like state, but it changes to a helix flanked by two short loops in the ADP-state. In addition, switch I region is closer to switch II region in the ATP-like state, resulting in the closure of the nucleotide-binding pocket. Second, in the switch II region, which is composed of the α4 helix and loop L11, the α4 tilts about 20 degrees and partly melts and L11 extends in the ATP-like state.

We then docked the atomic structures to cryoelectron microscopic images. Cryoelectron microscopy revealed that the "long axis" of the KIF1A motor domain in the ATP-state rotates ~20 degrees compared with that in the ADP-state. What roles this rotation plays is still a speculation, but this suggests that although the α4 helix tilts ~20 degrees in the crystal structure, when the motor is bound to the microtubule it remains fixed to the microtubule and the motor itself rotates relative to the microtubule.

We then analyzed additional states of ATP hydrolysis [36]. For this purpose, we produced a very short motor domain construct, C340. There are several ATP analogs that mimic the different states of the chemomechanical cycle of kinesin motors. First, three analogs mimic the strong-binding states: AMP-PCP, a nonhydrolyzable analog, mimics the preisomerization state; AMP-PNP, also a nonhydrolyzable analog, mimics the next prehydrolysis state;

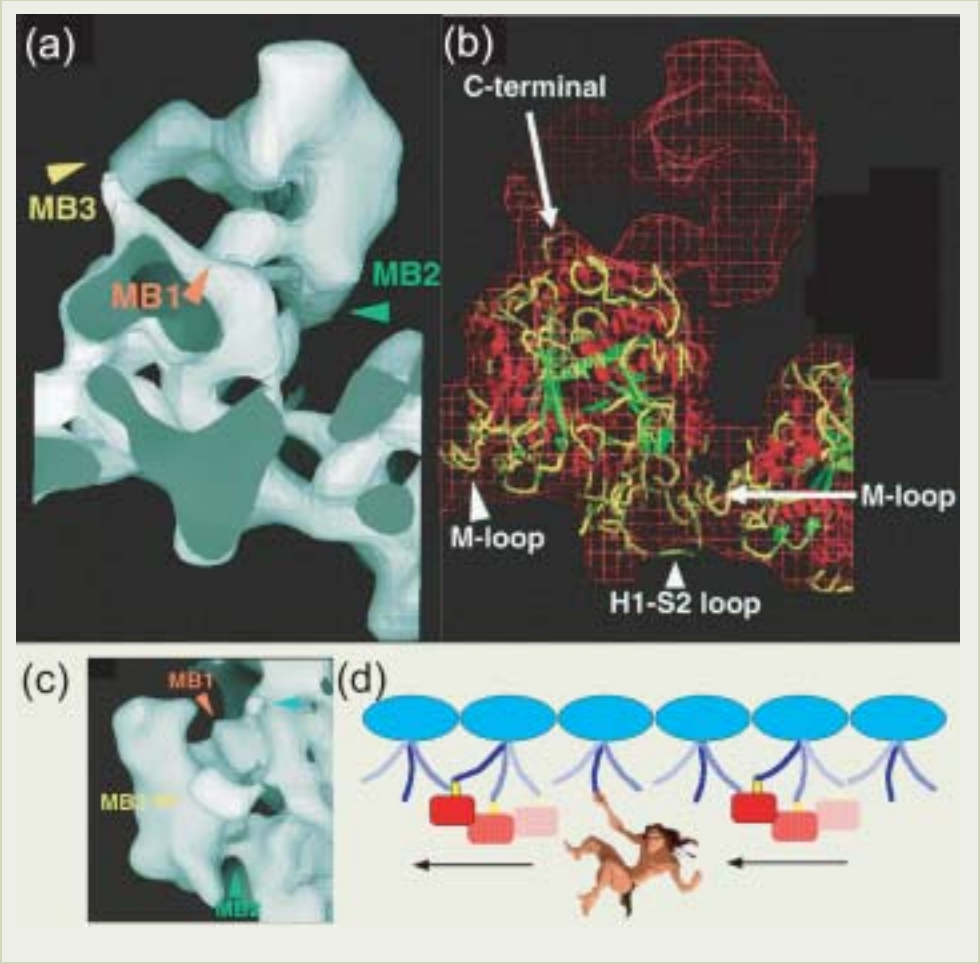

Fig. 7 **(a-c)** Docking of atomic model of KIF1A and tubulin. Surface representation from outside (c) and top view from plus end (a) and superposition of image on atomic model (b).
(d) Tarzan model of biased Brownian movement of KIF1A. Panels (a-c) reproduced with permission from Kikkawa et al. [23].

and ADP-AlFx mimics the early ADP-Pi state, in which ATP hydrolysis begins. ADP-Vi mimics the late ADP-Pi state, in which the association with the microtubule is the weakest, and is considered to be an actively detaching state (**Fig. 8c-f**). After that is the ADP state, a weak-binding state. As discussed above, we solved the AMP-PCP and ADP states by X-ray crystallography in a previous study. Therefore, we decided to determine three additional states, the AMP-PNP, ACP-AlFx, and ADP-Vi states; we have solved five states in total (**Figs. 8b-e**).

Comparing the five different states, the most significant conformational changes occur in switch I and II regions (**Figs. 8c-f**). In the preisomerization (AMP-PCP) state, γ-phosphate does not interact with any regions (**Fig. 8c**). In the prehydrolysis (AMP-PNP) state, γ-phosphate interacts with Ser^{215} and Gly^{251} (**Fig. 8d**). The switch I region elongates and changes its shape from a β-hairpin to a loop. Concomitantly, loop L11 in the switch II region extends downwards. In the early ADP-Pi (ADP-AlFx) state, a hydrogen bond between γ-phosphate and Gly^{251} in switch II is broken and L11 is raised (**Fig. 8e**). The raised conformation of L11 triggers a slight tilt of the α4 helix. In the late ADP-Pi (ADP-Vi) state, γ -phosphate is released from the nucleotide-binding pocket through the back door (**Fig. 8f**). This induces different interactions: loop L11 shortens and the elongated α4 helix tilts further.

KIF1A alternately uses two loops to bind microtubules

We docked the atomic structures of KIF1A and tubulin (**Fig. 9**)[36]. In tubulin, helices H11 and H12 mainly serve as the rail for KIF1A movement. In the strong-binding prehydrolysis (AMP-PNP) state, L11 is elongated and extends downwards binding to H11', which is between H11 and H12 (**Fig. 9a**). In the next early strong-binding ADP-Pi (ADP-AlFx) state, an early stage of hydrolysis, the extended L11 begins to rise (**Fig. 9b**). In the next late ADP-Pi state (ADP-Vi) state, the loop L11 is completely raised, but the loop L12 is also raised; therefore, the interaction of KIF1A with the microtubule rail is the weakest (**Fig. 9c**). This is an actively dissociating state. After the release of Pi in the ADP state, L12 extends downwards and binds to the E-hook, which is the C-terminus of tubulin (**Fig. 9d**). At this stage, the interaction between K-loop (L12) and E-hook, similar to the interaction between Tarzan's arm and the tether, causes the Brownian movement (**Fig. 7d**). Because of this, the motor does not dissociate from the rail in spite of the fact that it is in the weak-binding state. Therefore, Brownian movement is the underlying force for the motor movement, and when ADP dissociates, KIF1A binds to the microtubule with bias towards the plus end, probably due to the presence of higher affinity sites on the plus end of tubulin.

We tested this hypothesis of the alternate use of two loops by introducing mutations to L11 and L12 and observed changes in the binding between KIF1A and microtubules [36]. In the AMP-PNP state, introducing mutations in L11 resulted in a decreased strength of binding. In contrast, in the ADP state, introducing mutations in L12 resulted in a decreased strength of binding. These results confirmed that L11 is used for binding at the AMP-PNP state and L12 is used for that at the ADP state. In addition, when the strength of binding between KIF1A and microtubules was compared at different ATP hydrolysis steps in wild type constructs, ADP-Vi (late ADP-Pi) state was the weakest binding state and KIF1A actively dissociates from microtubules in this state.

In summary, KIF1A uses L11 and L12 alternately for binding to tubulin (**Figs. 9a-d**). In the ATP-like prehydrolysis state, KIF1A extends L11 and binds to the H11' helix of tubulin. Then L11 is raised, and KIF1A dissociates from tubulin in the late ADP-Pi state. In the ADP state, KIF1A extends L12, binding to the E-hook, and makes a Brownian movement. Therefore, energy derived from hydrolysis of ATP is used to dissociate from the microtubule at the late ADP-Pi state. This strategy is also used when kinases phosphorylate their substrates or when heterotrimeric guanine nucleotide-binding proteins (G proteins) interact with their target molecules (**Figs. 9e-h**). In both cases, energy derived from the hydrolysis of nucleotides is used for dissociation from the

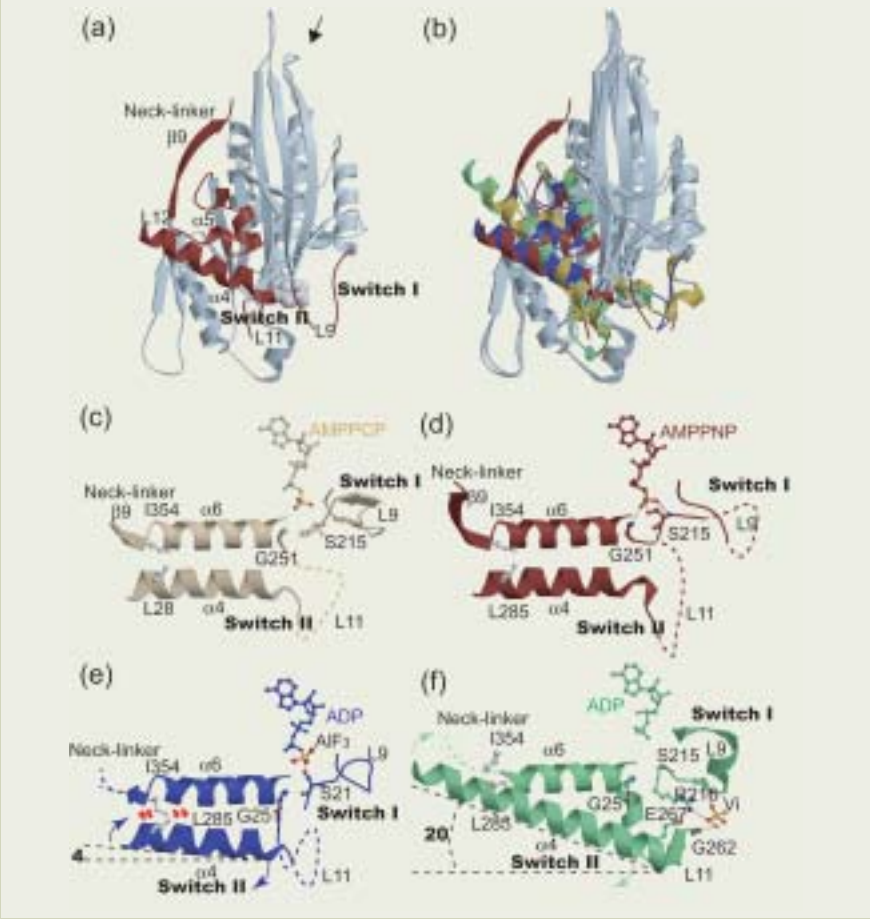

Fig. 8 (**a** and **b**) Crystal structures of KIF1A. (a) The AMP-PNP form . The switch I, switch II and neck linker regions are highlighted in red. (b) Superposition of AMP-PNP (red), ADP-AlFx (blue), ADP-Vi (green) and ADP (yellow) forms.
(**c-e)** Conformational changes in two switch regions during ATP hydrolysis. AMP-PCP (c), AMP-PNP (d), ADP-AlFx (e) and ADP-Vi (**f**) forms. Reproduced with permission from Nitta et al. [36].

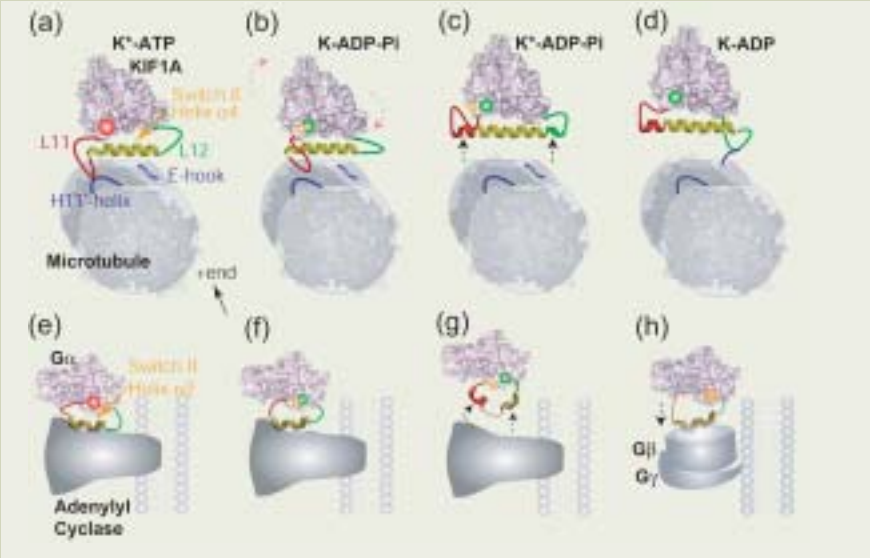

Fig. 9 Structural models of active detachment of KIF1A and G proteins. (**a-d**) KIF1A (pink)-microtubule (gray) complex observed from minus end of microtubule in different states of ATP hydrolysis. (a) Prehydrolysis state. (b) Early ADP-Pi state. (c) Late ADP-Pi state, that is, detaching state (indicated by arrows). (d) ADP state. L11, α4 and L12 are shown as colored ribbon model (red, yellow and green). H11' and E-hook of tubulin are shown in purple. ATP, ADP and Pi are shown as red, green and orange spheres, respectively. Asterisks refer to the second ATP or ADP-Pi state of KIF1A.
(**e-h**) The α subunit of G proteins and region corresponding to switch II are color-coded as in (a-d). Adenylyl cyclase and β and γ subunits of G proteins are shown in gray. (e) to (h) represent states during GTP hydrolysis corresponding to those described in (a) to (d). The energy derived from GTP hydrolysis is used for dissociation of G a from adenylyl cyclase as indicated by arrows in (g).

substrates or target molecules. Therefore, it was suggested that this is an evolutionarily conserved mechanism for nucleotide-binding proteins including kinases, G proteins, and motor proteins. The movement itself of motor proteins depends on the Brownian movement.

We would like to add some detailed discussion here. One of them is if neck linker regions play any roles in the movement of motor proteins by biased Brownian movement. The neck linker regions, which are located at the C-terminus of the motor domain of N-kinesins, are proposed to play important roles in dimeric motor movement. The neck linker of KIF1A is docked on the motor domain when in the ATP-bound state, but undocked when in the ADP-bound state, making conformational changes [28]. However, it is not likely that the neck linker contributes to biased Brownian movement, because results of optical trapping experiments were unaffected when beads were attached either to the N-terminus or C-terminus of the motor domain [34]. Another issue that needs to be discussed is the velocity achieved by biased Brownian movement. When a single molecule is bound to a bead and moves through the mechanism of Brownian movement, the bead moves at ~0.2 μm/s, which is slower than the velocity observed in microtubule gliding assays. However, with the clustering of a few KIF1A molecules on the bead surface, but without dimerization, the bead moves much faster. This enhancement can be explained from the nature of biased Brownian movement. The increase in velocity is caused by the suppression of the backward movement, which is caused by the presence of multiple motors; this results in an increase in the efficiency of forward movement, that is, the plus-end-directed movement.

References

[1] Hirokawa, N.: The crosslinker system between neurofilaments, microtubules and membranous organelles in frog axons revealed by quick freeze, freeze fracture, deep etching method. *J Cell Biol.*, **94**:129-142, 1982.

[2] Hirokawa, N., K. K. Pfister, H. Yorifuji, M. C. Wagner, S. T. Brady, and G. S. Bloom.: Submolecular domains of bovine brain kinesin identified by electron microscopy and monoclonal antibody decoration. *Cell*, **56**:867-878, 1989.

[3] Okabe, S. and N. Hirokawa.: Turnover of fluorescently labeled tubulin and actin in the axon. *Nature*, **343**:479-482, 1990.

[4] Hirokawa, N., R. Sato-Yoshitake, T. Yoshida, and T. Kawashima.: Brain dynein (MAP1C) localizes on both anterogradely and retrogradely transported membranous organelles in vivo. *J Cell Biol.*, **111**: 1027-1037. 1990.

[5] Hirokawa, N., R. Sato-Yoshitake, N. Kobayashi, K. K. Pfister, G. S. Bloom, and S. T. Brady.: Kinesin associates with anterogradely transported membranous organelles in vivo. *J Cell Biol.*, **114**:295-302, 1991.

[6] Aizawa, H., Y. Sekine, R. Takemura, Z.

Zhang, M. Nangaku, and N. Hirokawa.: Kinesin family in murine central nervous system. *J Cell Biol.*, **119**:1287-1296, 1992.
[7] Kondo, S. et al.: KIF3A is a new microtubules-based anterograde motor in the nerve axon. *J Cell Biol.*, **125**:1095-1107, 1994.
[8] Sekine, Y., Y. Okada, Y. Noda, S. Kondo, H. Aizawa, R. Takemura, and N. Hirokawa.: A novel microtubule-based motor protein (KIF4) for organelle transports, whose expression is regulated developmentally. *J Cell Biol.*, **127**:187-202, 1994.
[9] Nangaku, M., R. Sato-Yoshitake, Y. Okada, Y. Noda, R. Takemura, H. Yamazaki, and N. Hirokawa.: KIF1B; A novel microtubule plus end-directed monomeric motor protein for transport of mitochondria. *Cell*, **79**: 1209-1220, 1994.
[10] Noda, Y., R. Sato-Yoshitake, S. Kondo, M. Nangaku, and N. Hirokawa.: KIF2 is a new microtubule-based anterograde motor that transports membranous organelles distinct from those carried by kinesin heavy chain or KIF3A/B. *J Cell Biol.*, **129**:157-167, 1995.
[11] Okada, Y., H. Yamazaki, Y. Sekine-Aizawa, and N. Hirokawa.: The neuron-specific kinesin superfamily protein KIF1A is a unique monomeric motor for anterograde axonal transport of synaptic vesicle precursors. *Cell*, **81**:769-780, 1995.
[12] Kikkawa, M., T. Ishikawa, T. Wakabayashi, and N. Hirokawa.: Three-dimensional structure of the kinesin head-microtubule complex. *Nature*, **376**:274-276. 1995.
[13] Yamazaki, H., T. Nakata, Y. Okada, and N. Hirokawa.: KIF3A/B: A heterodimeric kinesin superfamily protein that works as a microtubule plus end-directed motor for membrane organelle transport. *J Cell Biol.*, **130**:1387-1399, 1995.
[14] Hirokawa, N.: Organelle transport along microtubules-the role of KIFs (Kinesin superfamily proteins). *Trend Cell Biol.*, **6**:135-141, 1996.
[15] Terada, S., Nakata, A. C. Peterson, and N. Hirokawa.: Visualization of slow axonal transport in vivo. *Science*, **273**: 784-788, 1996.
[16] Yamazaki, H., T. Nakata, Y. Okada, and N. Hirokawa.: Cloning and characterization of KAP3: a novel kinesin superfamily-associated protein of KIF3A/3B. *PNAS*, **93**(16): 8443-8448. 1996.
[17] Saito, N., Y. Okada, Y. Noda, Y. Kinoshita, S. Kondo, and N. Hirokawa.: KIFC2 is a novel neuron-specific C-terminal type kinesin superfamily motor for dendritic transport of multivesicular body-like organelles. *Neuron*, **18**: 425-438, 1997.
[18] Hirokawa, N.: Kinesin and dynein superfamily proteins and the mechanism of organelle transport. *Science*, **279**: 519-526, 1998.
[19] Yonekawa, Y., A. Harada, Y. Okada, T. Funakoshi, Y. Kanai, Y. Takei, S. Terada, T. Noda, and N. Hirokawa.: Defect in synaptic vesicle precursor transport and neuronal cell death in KIF1A motor protein-deficient mice. *J Cell Biol.*, **141**:431-441, 1998.
[20] Tanaka, Y., Y. Kanai, Y. Okada, S. Nonaka, S. Takeda, A. Harada, and N. Hirokawa.: Targeted disruption of mouse conventional kinesin heavy chain, KIF5B, results in abnormal perinuclear clustering of mitochondria. *Cell*, **93**: 1147-1158, 1998.
[21] Nonaka, S., Y. Tanaka, Y. Okada, S. Takeda, A. Harada, Y. Kanai, M. Kido, and N. Hirokawa.: Randamization of left-right asymmetry due to loss of nodal cilia generating leftward flow of extraembryonic fluid in mice lacking KIF3B motor protein. *Cell*, **95**:829-837, 1998.
[22] Okada, Y. and N. Hirokawa.: A processive single-headed motor: kinesin superfamily protein, KIF1A.*Science*,**283**:1152-1157, 1999.
[23] Kikkawa, M., Y. Okada, and N. Hirokawa.: 15Å resolution model of the monomeric kinesin motor: KIF1A. *Cell*, **100**:241-252, 2000.
[24] Setou, M., T. Nakagawa, D. H. Seog, and N. Hirokawa.: Kinesin superfamily motor protein KIF17 and mLin-10 in NMDA receptor-containing vesicle transport. *Science*, **288**: 1796-1802, 2000.
[25] Terada, S., M. Kinjo, and N. Hirokawa.: Oligomeric tubulin in large transporting complex is transported via kinesin in squid giant axons. *Cell*, **103**:141-155, 2000.
[26] Nakagawa, T., M. Setou, D. Seog, K. Ogasawara, N. Dohmae, K. Takio, and N. Hirokawa.: A novel kinesin superfamily motor, KIF13A, transports mannose-6-phosphate receptor to plasma membrane through direct interaction with AP-1 complex. *Cell*, **103**:569-581, 2000.
[27] Miki, H., M. Setou, K. Kaneshiro, and N. Hirokawa.: All kinesin superfamily protein, KIF, genes in mouse and human. *PNAS*, **98**(13): 7004-7011. 2001.
[28] Kikkawa, M., P. Sablin, Y. Okada, H. Yajima, R. J. Fletterick, and N. Hirokawa.: Switch-based mechanism of kinesin motors. *Nature*, **411**: 439 - 445, 2001.
[29] Zhao C., J. Takita, Y. Tanaka, M. Setou, T. Nakagawa, S. Takeda, H. W. Yang, S. Terada, T. Nakata, Y. Takei, M. Saito, S. Tsuji, Y. Hayashi, and N. Hirokawa.: Charcot-Marie-Tooth Disease ttpe2A caused by mutation in a microtubule motor KIF1Bb. *Cell*, **105**: 587-597, 2001.
[30] Setou, M., D.-H. Seog, Y. Tanaka, Y. Kanai, Y. Takei, M. Kawagishi, and N. Hirokawa.: Glutamate-receptor-interacting protein GRIP1 directly steers kinesin to dendrites. *Nature*, **417**(6884): 83-87. 2002.
[31] Wong, R. W.C., M. Setou, J. Teng, Y. Takei, and N. Hirokawa.: Overexpression of motor protein KIF17 enhances spatial and working memory in transgenic mice. *PNAS*, **99**: 14500-5. 2002.
[32] Guillaud, L., M. Setou, and N. Hirokawa.: KIF17 dynamics and regulation of NR2B trafficking in hippocampal neurons. *J Neurosci.*, **23**(1): 131-40. 2003.
[33] Homma, N., Y. Takei, Y. Tanaka, T. Nakata, S. Terada, M. Kikkawa, Y. Noda, and N. Hirokawa.: Kinesin superfamily protein 2A (KIF2A) functions in suppression of collateral branch extension. *Cell*, **114**:229-239, 2003.
[34] Okada, Y., H. Higuchi, and N. Hirokawa.: Processivity of the single-headed kinesin KIF1A through biased binding to tubulin. *Nature*, **424**:574-577, 2003.
[35] Ogawa, T., R. Nitta, Y. Okada, and N. Hirokawa.: A common mechanism for microtubule destabilizers– M-type kinesins stabilize curling of the protofilament using the class-specific neck and loops. *Cell*, **116**: 591-602, 2004.
[36] Nitta, R., M. Kikkawa, Y. Okada, and N. Hirokawa.: KIF1A alternately uses two loops to bind microtubules. *Science*, **305**: 678-683, 2004.
[37] Kanai, Y., N. Dohmae, and N. Hirokawa.: Kinesin transports RNA: isolation and characterization of an RNA-transporting granule. *Neuron*, **43**: 513-525, 2004.
[38] Hirokawa, N. and R. Takemura.: Molecular motors and mechanisms of directional transport in neurons. *Nature Reviews Neuroscience*, **6**: 201-214, 2005.
[39] Tanaka, Y., Y. Okada, and N. Hirokawa.: FGF-induced vescicular release of Sonic hedgehog and retinoic acid in leftward nodal flow is critical for left-right determination. *Nature*, **435**:172-177, 2005.
[40] Okada, Y., S. Takeda, Y. Tanaka, J.-C. I. Belmonte and N. Hirokawa.: Mechanism of nodal flow: a conserved symmetry breaking event in left-right axis determination. *Cell*, **121**: 633-644, 2005.
[41] Teng, J., T. Rai, Y. Tanaka, Y. Takei, T. Nakata, M. Hirasawa, A. B. Kulkarni, and N. Hirokawa.: The KIF3 motor transports N-cadherin and organizes the developing neuroepithelium. *Nat Cell Biol.*, **7**:474-82, 2005.
[42] Hirokawa, N.,Y. Tanaka, Y. Okada, and S. Takeda.: Nodal flow and the generation of left-right asymmetry. *Cell* **125**: 33-45, 2006.
[43] Midorikawa, R., Y. Takei, and N. Hirokawa.: KIF4 motor regulates activity-dependent neuronal survival by suppressing PARP-1 enzymatic activity. *Cell*, **125**: 371-383, 2006
[44] Yildiz, A., and P.R. Selvin.: Kinesin: walking, crawling or sliding along? *Trends Cell Biol.*, **15**: 112-120, 2005.
[45] Howard, J., A.J. Hudspeth, and R.D. Vale.: Movement of microtubules by single kinesin molecules. *Nature*, **342**: 154-158, 1989.
[46] Schnapp, B.J., B. Crise, M.P. Sheetz, T.S. Reese, and S. Khan.: Delayed Start-Up of Kinesin-Driven Microtubule Gliding Following Inhibition by Adenosine 5'-[b, g-Imido]Triphosphate. *PNAS*, **87**: 10053-10057, 1990.
[47] Astumian, R.D.: Thermodynamics and Kinetics of a Brownian Motor. *Science*, **276**: 917-922, 1997.
[48] Okada, Y. and N. Hirokawa.: Mechanism of the single-headed processivity: Diffusional anchoring between the K-loop of kinesin and the C terminus of tubulin. *PNAS*, **97**: 640-645, 2000.
[49] Rice, S., A.W. Lin, D. Safer, C.L. Hart, N. Naber, B.O. Carragher, S.M. Cain, E. Pechatnikova, E.M. Wilson-Kubalek, M. Whittaker, E. Pate, R. Cooke, E.W. Taylor, R.A. Milligan, and R.D. Vale.: A structural change in the kinesin motor protein that drives motility. *Nature*, **402**: 778-784, 1999.

Ultrahigh Pressure Earth Science: Applications of TEM and FIB Techniques for Study of Core-Mantle Boundary Region of Earth

Eiji Ohtani

Department of Earth Science, Graduate School of Science, Tohoku University

A laser heated diamond anvil cell (LHDAC) has been used to generate pressure and temperature exceeding the core-mantle boundary conditions, i.e., 130 GPa and 3000 K. The focused ion beam (FIB) method for preparation of the recovered samples and the analytical transmission electron microscope (ATEM) for their characterization are the ideal tools for studying the recovered samples from the Mega-bar conditions.

The partitioning coefficient of Fe and Mg between post-perovskite (PPv) and magnesiowustite (Mw) $KP^{Pv/Mw}$ = 0.30 is larger than that between perovskite (Pv) and Mw $K^{Pv/Mw}$ = 0.12 keeping a constant value up to the PPv phase boundary. The density jump associated with the post-perovskite transition combined with the compositional change associated with the change in the partition coefficient at Pv-PPv phase boundary is 1.7 %. Thus, the post-perovskite bearing assemblage in the lower-most mantle has negative buoyancy and tends to stabilize the region gravitationally against plume upwelling.

We have conducted a reaction experiment between molten iron and post-perovskite at the conditions equivalent to the core-mantle boundary (CMB). Significant amounts of oxygen up to 6.3 wt.% and silicon up to 4.0 wt.% are dissolved in metallic iron, and the solubility of silicon and oxygen in metallic iron can readily account for the density deficit of the core. The dihedral angle between the PPv and molten iron is around 67 degrees. A small amount of molten iron about 2 vol.% (1 wt.%) can be tapped by PPv at the base of the lower mantle, although percolative separation of metallic melt is effective. The core metal trapped in the PPv region can produce the core signature of the plume source at the base of the lower mantle. The partition coefficient of potassium between metallic iron and K-silicate, D_K is determined to be D_K ~0.15 at 134 GPa and 3500 K. The total potassium concentration in the core is about 35 ppm or 4 x 10^{-3} ppm ^{40}K, which could produce 0.23 TW of radiogenic power in the core assuming a primitive mantle concentration of potassium of 240 ppm.

Introduction

The Earth can be divided into three layers, crust, mantle, and the core. The study of the material science of the core has been limited due to a difficulty to produce the extreme conditions of the core-mantle boundary (CMB) (130 GPa and 3000-3500 K) and the core (360 GPa, 5000-7000 K). There is seismological anomaly, such as low velocity, preferred orientation, and high attenuation of the seismic waves based on the seismological observations. Therefore the bottom of the lower mantle, CMB, and the interior of the core are the new frontier for the material science of the Earth.

Recent progress of high-pressure techniques made it possible to achieve the conditions of the center of the Earth. A laser heated diamond anvil cell (LHDAC) [1, 2] has been used to generate pressures and temperatures exceeding the core-mantle boundary conditions, i.e., 130 GPa and 3000-3500 K. We can now study the recovered samples from the condition of the core-mantle boundary. The focused ion beam (FIB) method for preparation of the recovered samples [3] and the analytical transmission electron microscope (ATEM) for their characterization are the ideal tools for studying the recovered samples from the Mega-bar conditions, since the samples of the diamond anvil cell are very small with a diameter less than 100 μm and a thickness of about 20 μm.

In order to clarify the structure of the bottom of the lower mantle and the CMB region, we have conducted high pressure and temperature experiments on Mg-Fe partitioning between PPv and Mw, and Pv and Mw observed at the bottom of the lower mantle. We also made experiments to clarify the reaction between metallic iron and PPv which enables us to simulate the chemical reactions at CMB. Here, the details of these experiments are shown as examples of the high-pressure experiments conducted by using combination of LHDAC, FIB and ATEM for study of the central part of the Earth.

Experimental Procedure

High pressure generation by diamond anvil cell

High pressure and temperature experiments were carried out using the double-sided LHDAC technique [4]. A Mao-Bell type diamond anvil cell was used to generate high pressure. The sample was directly loaded into the sample hole (with a diameter of 70 ~ 200 μm) of a pre-compressed Re gasket together with some ruby chips. NaCl or silicate powder was used for a transmitting medium in the experiments.

We have studied the phase transformation of olivine and the chemical reaction of metallic iron and silicates at the core-mantle boundary conditions. Natural samples of K-feldspar (adularia $KAlSi_3O_8$ from Switzerland), and olivine $(Mg,Fe)_2SiO_4$ (San Carlos olivine), and natural and synthetic orthopyroxene $MgSiO_3$ were used as silicate components of the starting materials. The samples consisted of a powdered mixture of metallic iron and silicate composed of olivine, pyroxene, or K-feldspar was embedded between thermal insulator layers of the pure silicate or NaCl powders and loaded into a 50–80 μm hole drilled in a rhenium gasket for the reaction experiments on the metallic iron and silicates. A powdered or single crystalline San Carlos olivine was embedded between two layers of NaCl power as the thermal insulator in the gasket hole.

Pressure measurement

Pressures before and after heating were measured at room temperature by the ruby fluorescence method using ruby chips scattered on the culet surface of diamond anvils [5] and averages of those values were used as experimental pressures. Pressures in some runs were determined before and after heating at room temperature, based on the Raman T_{2g} mode at the culet of diamond anvil [6]. The Raman spectra of diamond were measured using a JASCO NRS-2000 micro-Raman spectrometer. The 514.5 nm line from Ar ion laser was used for excitation, and the laser spot on the culet of the diamond anvil was about 4 μm in

Sendai 980-8578, Japan
E-mail: Fohtani@mail.tains.tohoku.ac.jp

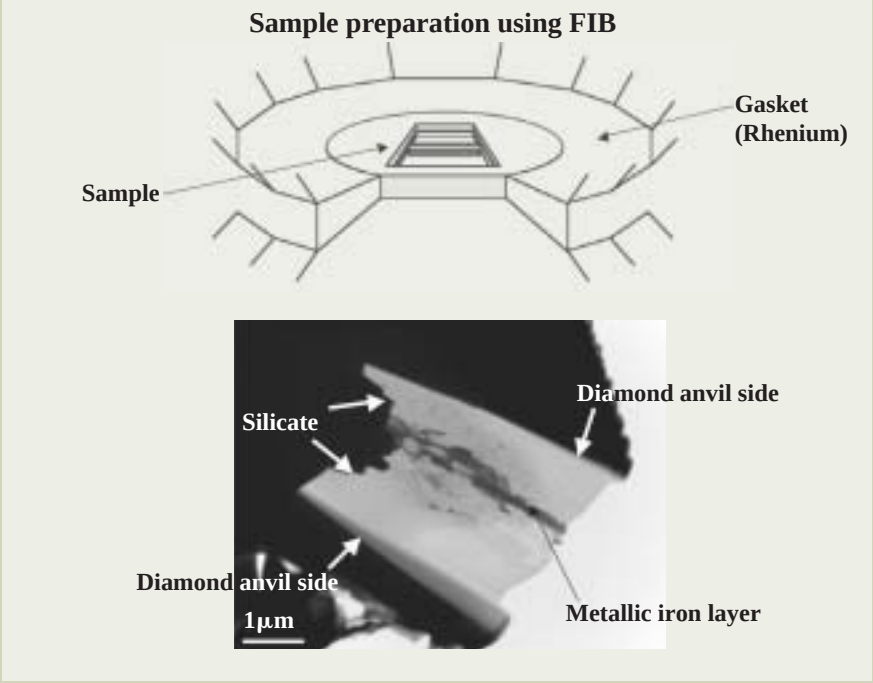

Fig. 1 The sample (Run FeAd4) prepared by FIB with a Ga ion beam for TEM observation **(Upper)**. A block specimen was prepared from the center part of the sample in a rhenium gasket and was picked out using the manipulator. FIB processing was conducted by monitoring the scanning ion beam (SIM) images **(Lower)**. A TEM image of the thin film of the sample prepared by FIB from the surface to the depth of about 15 mm with a uniform thickness ~100 nm. A metallic iron layer is sandwiched and embedded in K-silicate.

diameter. The Raman spectra of diamond were collected with a charge-couple device (CCD) with a resolution within 5 nm^{-1}.

X-ray diffraction at high pressure

We have conducted in situ X-ray diffraction for phase identification of the runs. In situ X-ray diffraction measurements were conducted at BL18C of Photon Factory, High Energy Accelerator Research Organization, Japan (KEK-PF). X-ray diffraction spectra were collected at the conditions of high pressure after quenching to room temperature using angle dispersive method and an imaging plate. The incident X-ray beam was monochromatized to a wavelength of 0.6130 Å and collimated to 40 μm in diameter. Typical exposure time for X-ray diffraction was 30 min. The collected images were integrated as a function of 2θ in order to obtain a conventional one-dimensional diffraction profile. We determined the pressure based on lattice parameters determined by the X-ray diffraction of ε-Fe and its equation of state in some runs containing metallic iron. The uncertainty in this pressure determination was smaller than ±2 GPa and generally consistent with the pressure values measured by the other methods. The phase identification of the run products was made after quenching from high temperatures at high pressure and room temperature by the in situ X-ray diffraction.

High temperature generation by laser heating

Samples were heated up to 3500 K at pressures in excess of 100 GPa using a high power multimode continuous wave Nd: yttrium-aluminum-garnet (YAG) laser (λ=1.064 μm, LEE LASER 8100MQ) [4]. The double-sided heating technique was used to minimize radial and axial temperature gradients in the sample. A single sided laser heating was also applied in some experiments with the same type laser at the BL-13A at KEK-PF in Tsukuba, Japan [4]. In the experiments to study the phase transition of ferrous iron bearing San Carlos olivine samples, no laser absorber was used to avoid contamination and reaction with the starting materials. In the experiments on the reaction of metallic iron and silicate phases, a metallic iron foil or a mixture of metallic iron and the silicate phases such as olivine, orthopyroxene, or adularia sandwiched with the pure silicates thermal insulators were placed in the sample hole of the rhenium gasket. Metallic iron was worked as the laser absorber of the sample in these configurations. The laser spot with a focused size of about 40-50 μm in diameter was slowly scanned (with a speed of less than 10 μm/sec) to heat the entire sample homogeneously in order to minimize the stress and avoid chemical differentiation in the sample by long heating duration with steep temperature gradient at a fixed position.

Temperatures were determined from both sides by fitting the emission spectra from the heated sample to the gray body formula [4, 7] and were maintained at 1500-3500 K for 10 to 90 min. The fluctuation of temperature during heating at a constant laser power was ±100 K at around 1500 K and ±250 K at around 3500 K.

Preparation of the TEM foils by FIB and characterization of run products by TEM

The samples in the rhenium gasket were prepared with the focused ion beam system, FIB (JEOL JEM-9310FIB), and the pick-up method for TEM observation [3]. Grooves were made in the specimen recovered from the diamond anvil cell by using gallium ion beam in the vicinity of the area to be analyzed by the electron microscope TEM/STEM. A block piece was recovered on the stage of a molybdenum-grid using a glass pipette attached to a manipulator under an optical microscope. The block piece was thinned by gallium ion beam again to prepare TEM foils. The foils were cleaned by mild Ar milling in the final stage of the sample preparation. Thus, a thin film with a uniform thickness of 100 nm suitable for ATEM measurements was prepared in this work. **Fig. 1** shows a schematic figure of the specimen prepared by FIB, and a TEM image of the recovered sample for the analysis.

Microstructures and chemical compositions were examined using ATEM (JEOL JEM-2010, JEM-2010F, JEM-2100F and JEM-2500SE) equipped with an energy-dispersive X-ray spectroscope (EDS) at the Tohoku University, Institute for Solid State Physics, University of Tokyo, and Application and Research Center of JEOL Ltd. Quantitative chemical analysis of metallic iron and coexisting silicates in the samples recovered from 50-134 GPa and 1500-3500 K was carried out by STEM (scanning TEM)-EDS mode. The TEM was operated with an accelerating voltage of 200 kV. In the STEM-EDS mode with an electron beam current of 5 nA, a focused stationary beam with a diameter of 1 nm was rastered over 100 × 80 to 300 × 250 nm, to avoid electron beam damage to the samples and resulting ATEM analytical errors. The k-factor [8] was determined according to the parameter-less correction method [9,10].

Results and Discussion

Partitioning of Mg and Fe between Magnesiowustite, perovskite, and post-perovskite

Partitioning of Mg and Fe between the coexisting phases at the bottom of the lower mantle is important to evaluate the density of

this region, since the amount of Fe in minerals affect the mean density of this region. We clarified the Mg and Fe partitioning between perovskite (Pv) and magnesiowustite (Mw) and that between post-perovskite (PPv) and magnesiowustite (Mw). Experimental conditions and results are summarized in **Table 1**. Detailed results are given in Kobayashi et al [11]. We determined that the partition coefficients of Pv and Mw, $K^{Pv/Mw}$, is in the range from 23.0 GPa to 95.4 GPa at around 1500~1600 K. X-ray diffraction pattern obtained at 123.6 GPa and 300 K after laser heating and temperature quenching is given in **Fig. 2**. Although a couple of unknown minor peaks were overlapped in the pattern, PPv (post-perovskite) phase with a space group of Cmcm and Mw are clearly observed as shown in this diffraction pattern. The PPv phase was observed above 105 GPa, which was generally consistent with the boundary of Pv-PPv transition reported by Murakami et al. [12]. The diffraction pattern of the recovered sample synthesized at 64.2 GPa and 1600 K indicates the coexistence of Pv and Mw as shown in **Fig. 2**.

TEM observations of the recovered samples indicate that PPv was amorphoused, whereas some grains of segregated metallic iron were also observed in some areas of the samples, although the precise compositions of metallic iron were not determined due to its small grain sizes (less than 10nm). No other phases were observed in the recovered samples. We determined the partition coefficients of Pv and Mw, and PPv and Mw based on the ATEM measurements.

Fig. 3 shows the Mg-Fe partition coefficients $K^{Pv/Mw}$ and $K^{PPv/Mw}$ at various pressures around 1500~1600 K based on the ATEM analysis. The previous data reported by Mao [13] and Andrault [14] in the olivine system, and Kesson [15] in the pyrolitic system, are also shown in the same figure. Our results indicates clearly a higher FeO content in PPv coexisting with Mw compared to that in perovskite; i.e., $K^{PPv/Mw} = 0.30$ compared to $K^{Pv/Mw} = 0.12$ keeping a constant value within experimental errors up to the Pv-PPv phase boundary.

Mao et al. [13] and Andrault [14] reported a significant increase in $K^{Pv/Mw}$ that derived from the V_0-X (the molar fraction of $FeSiO_3$ component) relation with increasing pressure, which are inconsistent with our results. Andarult [14] estimated $K^{Pv/Mw}$ based on the unit cell volume ratio of Pv and Mw determined at high pressure by X-ray powder diffraction, leading to a large uncertainty. The $K^{Pv/Mw}$ reported by Mao et al. [13] shows similar values within our experimental errors. In this study, compositions were cross-checked by ATEM analysis and X-V relation determined by X-ray diffraction collected at ambient condition. Badro et al. [15] observed a pressure induced spin transition of iron in Mw at around 60~70 GPa and predicted that almost all iron partitions into Mw even though the spin transition occurs in Pv. However, the effect of spin transition on Mg-Fe partitioning was not observed in our study, and Mw maintained a much higher iron content than Pv up to the PPv phase boundary. Relatively low value of $K^{Pv/Mw}$= 0.12 in comparison with previous studies may be explained by the temperature dependence of $K^{Pv/Mw}$[13, 14, 16].

In contrary to our results, the recent study of phase relations of a pyrolitic composition in the condition of D" layer [17] indicated that PPv contains iron smaller than Pv. The discrepancy may be due to the effect of trivalent cations, such as Al^{3+} and Fe^{3+} on Mg-Fe partitioning behavior [e.g. 18, 19]. The spin transition of iron in Pv observed at 120 GPa [20] may also be an important factor to consider a difference from Mg-Fe partitioning between PPv and Mw. Mao et al. [21] suggested that PPv has a solubility of iron higher than coexisting Mw, which was estimated based on the unit cell parameters obtained from X-ray diffraction. Our result implies that iron still prefers Mw to PPv at whole mantle pressures.

We calculated the bulk density change at Pv-PPv boundary at 105 GPa assuming that the metallic phase is pure iron with the hcp structure [22] and Mw with rock salt structure [4]. The density jump at Pv-PPv boundary is 1.7 % in case the initial bulk iron content was preserved in Pv and Mw phases, and 1.5 % when metallic phase was segregated (bulk X in Pv and PPv were 0.05 and 0.09, respectively). Thus, the post-perovskite bearing assemblage in the lower-most mantle has negative buoyancy and tends to stabilize the region gravitationally against plume upwelling.

Iron and post-perovskite reaction and solubility of O and Si in molten iron at CMB condition

Recent discovery of the post-perovskite (PPv) phase [12] revealed that this phase coexists with molten iron and some reactions between the phases may occur at the CMB condition. We have conducted a reaction experiment between molten iron and post-perovskite at 139 GPa and 3000 K equivalent to the CMB condition. The TEM image of the coexisting metallic iron and post-perovskite phase (Run f70En07) recovered from the CMB condition is shown in **Fig. 4A**, in which we can see a clear image of metallic iron sandwiched by PPv. **Fig. 4B** is the high magnification image of the same run product, where we can observe the metallic iron melt at triple junctions of PPv grains in this image.

The compositions of the metallic iron and post-perovskite were determined by ATEM, indicating that a significant amount of oxygen up to 6.3 wt.% and silicon up to 4.0 wt.% are dissolved in metallic iron. Recent reevaluation of the outer core density revealed that it is lower by 7-10 % than that of pure metallic iron [23, 24]. The solubility of silicon and oxygen in metallic iron observed in this study can readily account for density deficit of 10 % in the core. The present results strongly imply that both oxygen and silicon are the plausible candidates of the light elements in the core. The solubility of oxygen and silicon in molten iron coexisting with PPv and Pv increases with increasing pressure at 3000 K [25, 26]. The extrapolated solubility of these elements in molten iron coexisting with Pv [26] to CMB condition is consistent with those with PPv determined in this study. The present result is in contrast with the chemical reaction between metallic iron and (Mg, Fe)SiO_3 perovskite to form FeO, FeSi, and MgO suggested by previous authors [27, 28]. A dissolution reaction of oxygen and silicon into molten iron occurs instead of formation of separate phases of FeO and FeSi around the melting point of iron-alloy coexisting with PPv phase.

We have measured apparent dihedral angles between molten iron and PPv in the run product recovered from 139 GPa and 3000 K (Run f70En07) based on TEM image (**Fig. 4B**). The median value of total 114 measurements of the apparent dihedral angle, which corresponds to the true dihedral angle, was 67 degrees. Although the dihedral angle is slightly smaller than that between perovskite and molten iron-alloy determined at 25 GPa and 2373 K, 71 degrees [29], it is larger than 51 degrees determined at 47 GPa and 3000 K [26], and it is still larger than the critical wetting angle of 60 degrees. The dihedral angle around 67 degrees between the PPv and molten iron indicates that the percolation of metallic melt occurs effectively at the base of the mantle in the case of coexistence of the metallic melt fraction greater than 2 vol.% [30], and that a small amount of iron around 2 vol.% could remain in the regions of the PPv lithology at CMB.

Strong dynamic instabilities are expected at CMB due to sedimentation of slab materials and upwards flow of the hot mantle plumes [e.g. 31, 32, 33]. Therefore, the metallic melt and lower mantle silicates can be mixed in the contact region of CMB. Since the dihedral angle between perovskite and molten iron is 51 degrees, it is small enough [30] for complete separation of molten iron from the lower mantle with the perovskite lithology. On the other hand, a small amount of molten iron, about 2 vol.% (1 wt.%), can be tapped by PPv [30] in the region of the PPv lithology at CMB, since the present result indicates that complete percolative separation of the core metal does not occur because of the dihedral angles greater than 60 degrees between molten iron and PPv.

Geodynamic studies imply that some mantle plumes are originated from the CMB region. Walker et al. [34] pointed out that some plumes derived from the base of the lower mantle show the outer core signature formed by the inner core crystallization. Brandon et al. [35, 36] estimated that addition of 0.5-1 wt.% of core metal to the CMB region (D" layer) can produce the signature observed in the plumes. The amount of core metal trapped in the PPv region at CMB can produce the core signature of the plume source at the base of the lower mantle [36].

Potassium partitioning between iron and silicate and energetics of the core

A study of the potassium dissolution in molten iron at the CMB condition is important to clarify the heat source of the core to drive geodynamo to generate the Earth's magnetic fields. We have conducted reaction experiments between molten iron and K-feldspar (adularia) at 134 GPa and 3500 K, which corresponds to the core-mantle boundary condition. Both textural and compositional observations by ATEM of the sample revealed that metallic iron was molten and chemical reactions between metallic iron and K-silicate occurred. The TEM (BF and HAADF) images of the sample are shown in **Fig. 5**. An interconnected network due to the large melt fraction and a segregated pool of metallic iron with the rounded curvature of the metal-sili-

Table 1 Experimental conditions and results

Run no.	Pressure GPa	Temperature K	Duration min.	Phases observed	Xpv	Xmw	K
Mg-Fe partitioning between Mw and perovskite, and Mw and post-perovskite							
SC4	32.2	1600	60	Mw+Pv	0.029(6)	0.186(11)	0.13(3)
SC8	41.5	1600	90	Mw+Pv	0.043(14)	0.216(3)	0.16(5)
SC22	58	1600	80	Mw+Pv	0.015(1)	0.147(13)	0.09(1)
SC14	95.4	1600	60	Mw+Pv	0.014(6)	0.102(19)	0.12(6)
SC15	123.6	1500	40	Mw+PPv	0.042(11)	0.129(24)	0.30(10)
Iron and post-perovskite reaction and solubility of O and Si in molten iron at CMB condition							
f70En07	139	3000	10	Fe(liquid)+PPv			
FeEn19	130	2000	10	Fe(solid)+PPv			
Potassium partitioning between iron and silicate and energetics of the core							
FeAd4	134	3500		60Fe(liquid)+K-fel(liquid)			
FeAd6	104	3350		30Fe(solid)+K-fel(solid)			

Mw, magnesiowustite; Pv, perovskite; PPv, post-perovskite; K-fel, K-feldspar (Adularia)

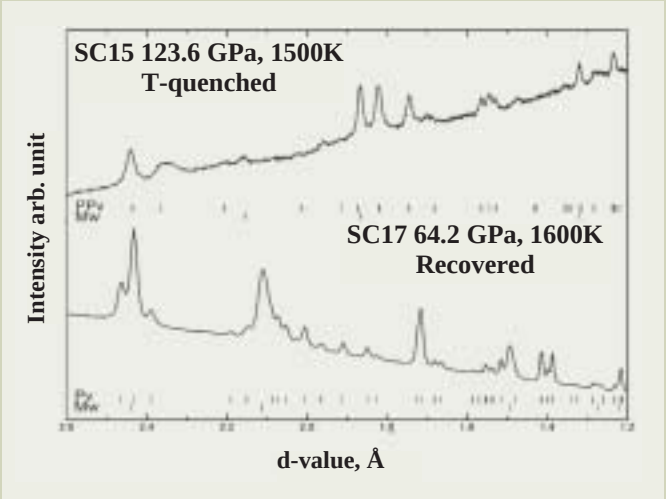

Fig. 2 The X-ray diffraction pattern of 123.6 GPa and 300 K after laser heating at 1500K **(Upper)**. The post-perovskite phase is clearly observed in the diffraction pattern. The diffraction pattern of the recovered sample of Pv and Mw synthesized at 64.2 GPa and 1600 K **(Lower)**. Perovskite and magnesiowustite are observed in this pattern. Solid triangle, PPv; open triangle, Pv; solid circle, Mw.

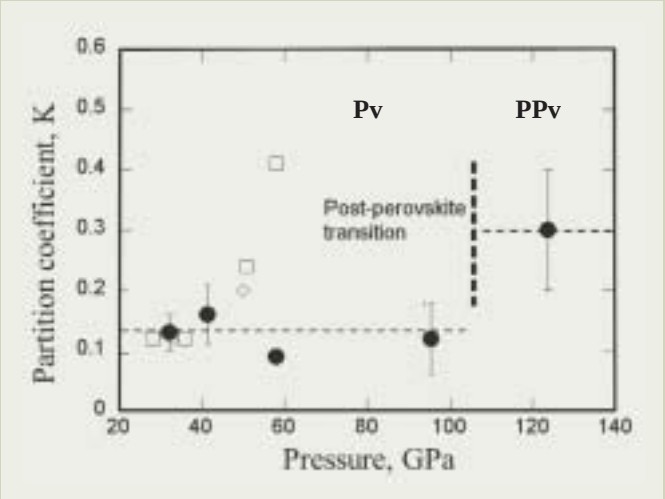

Fig. 3 Pressure versus Mg-Fe partition coefficients between Pv and Mw, $K^{Pv/Mw} = (FeO/MgO)_{Pv}/(FeO/MgO)_{Mw}$, and PPv and Mw, $K^{PPv/Mw} = (FeO/MgO)_{PPv}/(FeO/MgO)_{Mw}$ compared with previous studies. Solid circles represent K values of this study from ATEM. Open diamond, Mao et al. [13] at 1500 K; open square, Andrault [14] at 2200 K; plus, Kesson et al. [15].

cate interface are shown in **Fig. 5**. These microstructures are typically observed in the mixed samples of molten metal and silicates [e. g., 37]. The concentrations of these elements were determined by the intensity of EDS spectra for the elements. The bright field and X-ray element maps of metallic iron and K-silicate are also show in **Fig. 5**. The typical EDS spectra of the coexisting phases at 134 GPa and 3500 K are shown in **Fig. 6**. The results of the chemical analysis by ATEM are given in **Table 2**. Depletion of potassium and silicon and existence of iron were observed in K-silicate adjacent to the metallic iron in contrast to the iron-free composition of the starting material, $KAlSi_3O_8$. The change in compositions of K-silicate occurred due to melting of the K-silicate, and it is consistent with the previous works [38, 39]. A sudden fluctuation of the temperature at the melting point, was observed due to the change of the absorption of laser power, indicating that metallic iron was molten [40]. We also made an experiment at 104 GPa and 3350 K (Run FeAd6). The metallic iron was unlikely to be molten because of existence of polycrystalline metallic iron, with granular K-silicate that preserved textures of the original metal-silicate mixtures, and also because of the very low solubility of oxygen and potassium in metallic iron (Table 2) [26]. Although the melting point of iron at ~100 GPa is 2800–3500 K [22, 41], it has not yet been determined precisely. The chemical analyses of K-silicate adjacent to metallic iron in this quenched sample gives a composition close to $KAlSi_3O_8$, which indicates the K-silicate was not molten in this condition.

The ATEM analysis confirmed that potassium and oxygen were dissolved in metallic iron at 134 GPa and 3500 K (**Fig. 6**); e. g., quenched metallic iron contains 0.8 wt.% potassium and 1.4 wt.% oxygen. The high concentration of oxygen in metallic iron observed at 134 GPa and 3500 K clearly demonstrates that oxygen is a plausible candidate for the light element in the Earth's core. In our study, some amount of potassium can be dissolved in metallic iron with absence of sulfur under the core-mantle boundary conditions, in contrast to previous experimental studies at lower pressures in which the amount of potassium in sulfur-free iron was not detected, or very low [38, 29, 42]. In our ATEM analysis, the X-ray counts for potassium and oxygen in both metallic iron and K-silicate exceed the minimum detectable limits (**Fig. 6**).

The oxygen fugacity relative to the iron–wüstite (IW) buffer can be calculated on the basis of the activities of FeO in silicate and Fe in metal [43]. The oxygen fugacity was estimated to be -3.88 and -3.49 log unit below the IW buffer for the experiments made at 134 GPa and 104 GPa, respectively.

The partition coefficient of potassium between metallic iron and K-silicate, D_K (= concentration, wt. %, of K in metallic iron / concentration, wt. %, of K in K-silicate), is D_K ~0.15 at 134 GPa and 3500 K. The D_K value at 134 GPa and 3500 K is much larger than the

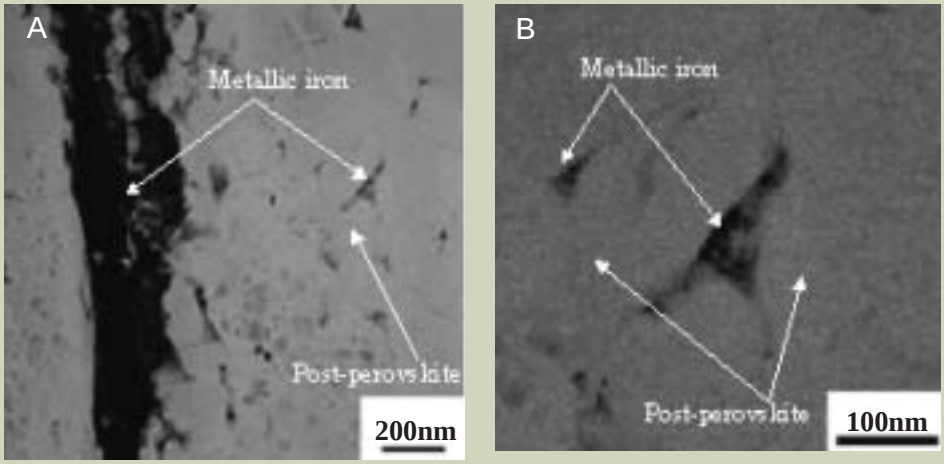

Fig. 4 Bright field TEM images of the sample recovered from 139 GPa and 3000 K (Run f70En07). (A) the coexistence of metallic iron and post-perovskite phases. (B), a high magnification image of metallic iron and PPv. Metallic iron exists in the triple junctions of PPv.

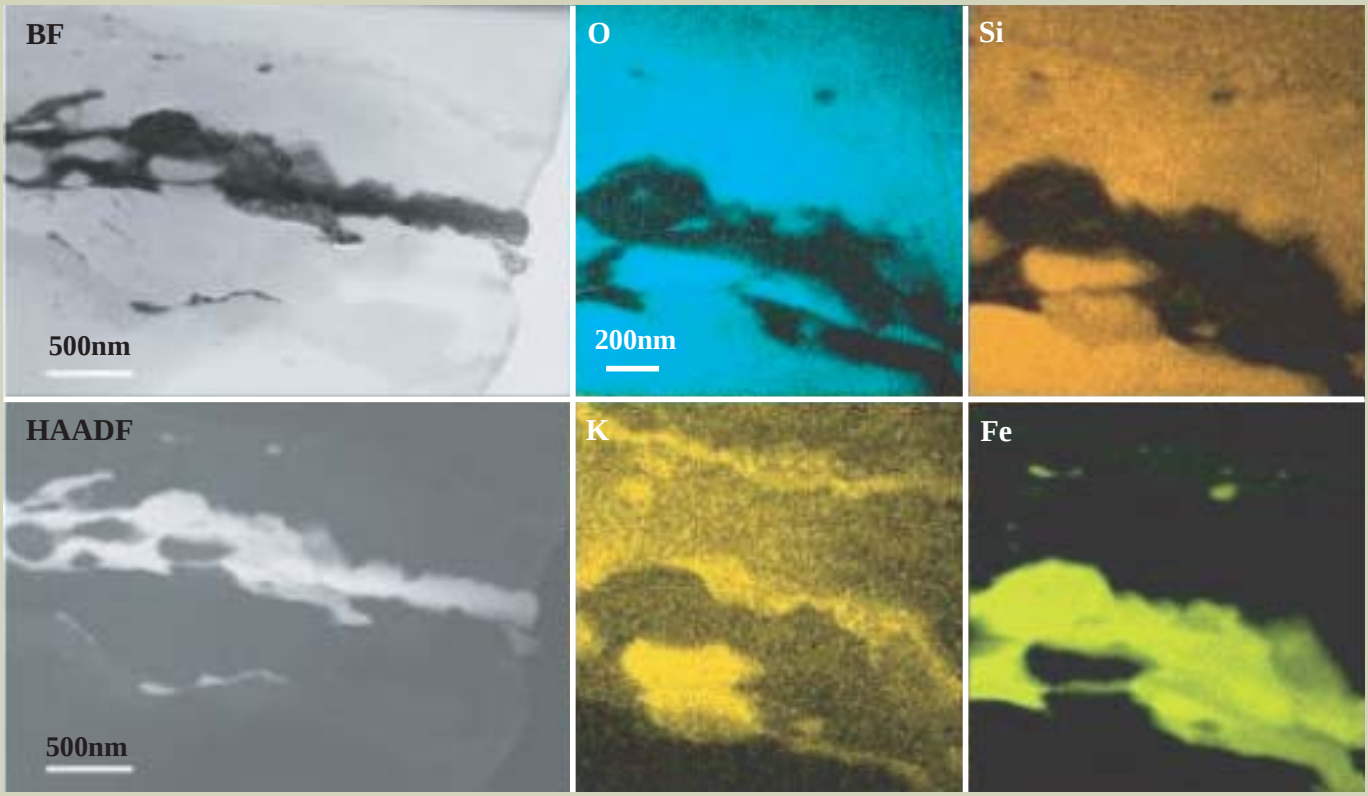

Fig. 5 Analysis of chemical compositions of the sample recovered from 135 GPa and 3500 K (run FeAd4). Bright field (BF) image, high-angle annular dark-field scanning transmission electron microscopic (HAADF-STEM) image, and X-ray element maps of metallic iron and silicate. The distributions of the elements for O, Si, K, and Fe are shown. In the element maps, bright and dark parts represent higher and lower concentrations of the elements, respectively.

partition coefficient determined up to 26 GPa in previous studies [38, 39, 42]. This suggests that pressure significantly affects the solubility of potassium in molten metallic iron. The increase in D_K with pressure is likely to be related to the change in electronic structure of potassium at high pressure [44, 45].

Our results indicate that potassium can readily be dissolved into the core by the chemical reactions between the molten iron and K-silicate at the CMB condition. The D_K value 0.15 at 134 GPa and 3500 K, corresponding to the conditions of CMB, implies that the total potassium concentration in the core is about 35 ppm assuming that a primitive mantle concentration of potassium is 240 ppm [46]. The total potassium concentration of 35 ppm, or 4×10^{-3} ppm ^{40}K, in the core could produce 0.23 TW of radiogenic power, which corresponds to 2–12% of the current total heat flux across CMB, 2–10 TW [e.g., 47]. Our estimation is a tentative one because the D_K value could be modified by incorporation of sulfur into the core and its strong temperature dependency [e. g., 48].

Acknowledgement

This work was conducted by collaboration with T. Kondo, N. Hirao, T. Sakai, M. Miyahara, Y. Kobayashi, H. Sakai, A. Suzuki of Tohoku University, T. Kikegawa of KEK-PF, N. Endo, T. Kuba, and T. Suzuki of Application and Research Center, JEOL Ltd. I would like to appreciate these people for collaboration and fruitful discussions during this work. This work was partly supported by the Grants-in-aid for scientific research from Ministry of Education, Culture, Science, and Sports and Technology of Japanese Government to E. O. (no. 14102009 and 16075202) and to T. K. (no.16330164). It was conducted as a part of the 21st COE program Advanced Science and Technology Center for the Dynamic Earth at Tohoku University.

References

[1] Mao, H.-K., Shen, G., and Hemley, R. J.: *Science*, **278**, 2098-2100 (1997).
[2] Hirao, N., Ohtani, E., Kondo, T., Endo, N., Kuba, T., Suzuki, T., and Kikegawa, T.: *Geophys. Res. Lett.*, **33**, L08303, doi:10. 1029/2005GL025324 (2006).
[3] Suzuki, T., Sibata, M., Okunishi, E., Endo, N. Kuba, T.: *J. Japan Inst. Metals.*, **68**, 293-298 (2004).
[4] Kondo, T., Ohtani, E., Hirao, N., Yagi,

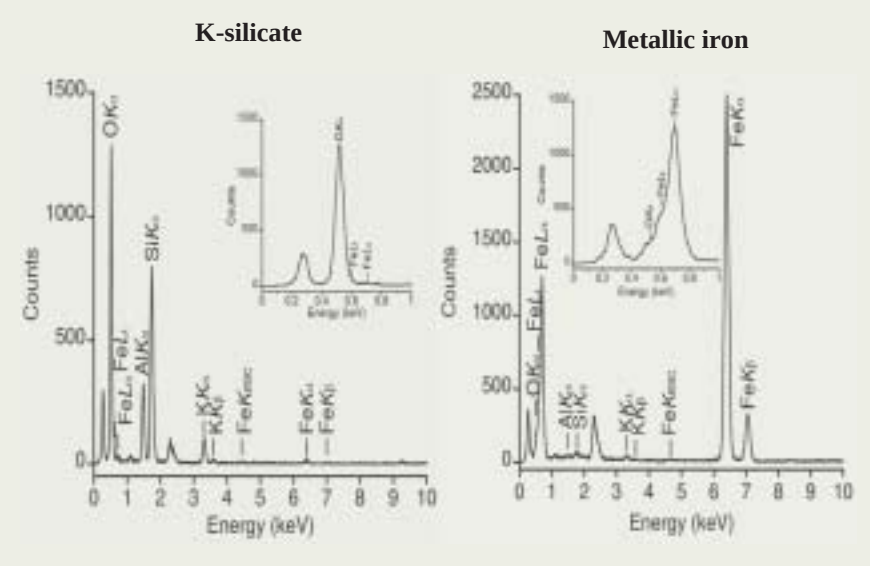

Fig. 6 Typical EDS spectra of metallic iron (*right*) and K-silicate (left). (*Insets*) The spectra in the low energy range from 0 to 1.0 keV: O$K\alpha$ line (E = 0.523keV), Fe$L\iota$ (0.615 keV), and Fe$L\alpha$ (0.705keV).

Table 2 Chemical compositions of metallic iron and K-silicate determined by ATEM (values in weight %)

	FeAd4				FeAd6			
Run	134GPa and 3500K				104GPa and 3350K			
	Metal	σ	K-fel	σ	Metal	σ	K-fel	σ
n	7		7		5		6	
Al	0.16	0.05	11.6	0.71	0.23	0.1	9.68	0.25
Si	0.32	0.16	25.25	0.75	0.53	0.17	28.99	0.62
Fe	97.32	0.46	1.12	0.3	98.63	0.62	1.78	1.7
K	0.77	0.13	0.77	5.29	0.16	0.07	0.16	0.07
O	1.43	0.27	56.75	0.41	0.41	0.32	0.41	0.32

Partition coefficients of potassium, DK, between metallic iron and K-silicate are 0.15 ± 0.07 at 134 GPa and 3500 K and 0.016 ± 0.007 at 104 GPa and 3350 K, respectively. n: the number of area measured by ATEM.

T., and Kikegawa, T.: *Phys. Earth Planet. Inter.*, **143-144**, 201-213 (2004).

[5] Mao, H.-K., Bell, P. M., Shaner, J. W., and Steinberg, D. J.: *J. Appl. Phys.*, **49**, 3276-3283 (1978).

[6] Akahama, Y. and Kawamura, H.: *J. Appl. Phys.*, **96**, 3748–3751 (2004).

[7] Boehler, R.: *Rev. Geophys.*, **38**, 221-245 (2000).

[8] Cliff, G. and Lorimer, G. W.: *J. Microsc.*, **103**, 203–207 (1975).

[9] van Cappellen, E.: *Microscopy, Microanalysis, Microstructures*, **1**, 1-22 (1990).

[10] van Cappellen, E. and Doukhan, J. C.: *Ultramicroscopy*, **53**, 343-349 (1994)

[11] Kobayashi, Y., Kondo, T., Ohtani, E., and Hirao, N., Miyajima, N., Yagi, T., Nagase, T., and Kikegawa, T.: *Geophys. Res. Lett.*, **32**, L19301, doi:10.1029/2005GL023257 (2005).

[12] Murakami, M., Hirose, K., Kawamura, K., Sata, N., and Ohishi, Y.: *Science*, **304**, 855-858 (2004).

[13] Mao, H.-K., G. Shen, and R. J. Hemley.: *Science*, **278**, 2098-2100 (1997).

[14] Andrault, D.: *J. Geophys. Res.*, **106**, 2079-2087 (2001).

[15] Kesson, S. E., J. D. Fitz Gerald, H. St. C. O'Neill, and J. M. G. Shelley.: P*hys. Earth Planet. Inter.*, **131**, 295-310 (2002).

[16] Badro, J., G. Fiquet, F. Guyot, J. P. Rueff, V. V. Struzhkin, G. Vanko, and G. Monaco.: *Science*, **300**, 789-791 (2003).

[17] Murakami, M., Hirose, K., Sata, N., and Ohishi, Y.: *Geophys. Res. Lett.*, **32**, L03304, doi:10.1029/2004GL021956 (2005).

[18] Frost, D. J. and Langenhorst, F.: *Earth Planet. Sci. Lett.*, **199**, 227-241 (2002).

[19] McCammon, C. A., Lauterbach, S., Seifert, F., Langenhorst, F. and van Aken, P. A.: *Earth Planet. Sci. Lett.*, **222**, 435-449 (2004).

[20] Badro, J., Rueff, J. P., Vanko, G., Monaco, G., Fiquet, G. and Guyot, F.: *Science*, **305**, 383-386. (2004).

[21] Mao, W. L., Shen, G., Prakapenka, V. B., Meng, Y., Cambell, A. J., Heinz, D., Shu, J., Hemley, R. J. and Mao, H.-K.: *Pro. Natl. Acad. Sci. U.S.A.*, **101**, 15,867-15,869 (2004).

[22] Ma, Y.-Z., Somayazulu, M., Shen, G.-Y., Mao, H.-K., Shu, J.-F. and Hemley, R. J.: *Phys. Earth Planet. Inter.*, **143-144**, 455–467 (2004).

[23] Anderson, O.L. and Isaak, D.G.: *Phys. Earth Planet. Inter.*, **131**, 19-27 (2002).

[24] Shanker, J., Singh, B. P., and Srivastava, S. K.: *Phys. Earth Planet. Inter.*, **147**, 333-341 (2004).

[25] Hillgren, V. J. and Boehler, R.: *Mineral. Mag.* **62A**, 624-625 (1998).

[26] Takafuji, N., Hirose, K., Ono, S., Xu, F., Mitome, M., and Bando, Y.: *Earth Planet. Sci. Lett.*, **224**, 249-257 (2004).

[27] Knittle, E. and Jeanloz, R.: *Science*, **251**, 1438-1443 (1991).

[28] Goarant, F., Guyot, F., Peyronneau, J., Poirier, J. P.: *J. Geophys. Res.*, **97**, 4477-4487 (1992).

[29] Shannon, M. C. and Agee, C. B.: *Science*, **280**, 1059-1061 (1998).

[30] von Bargen, N. and Waff, H.S.: *J. Geophys. Res.*, **91**, 9261-9276 (1986).

[31] Brandon, A. D. and Walker, R. J.: *Earth Planet. Sci. Lett.*, **232**, 211-225, (2005).

[32] Lay, T., Williams, Q., and Garnero, J.: *Nature*, **392**, 461-468 (1998).

[33] Garnero, E. J.: *Science*, **304**, 834-836 (2004).

[34] Walker, R. J., Morgan, J. W., and Horan, M. F.: *Science*, **269**, 819 (1995).

[35] Brandon, A. D., Walker, R. J., Morgan, J. W., Norman, M. D., and Prichard, H. M.: *Science*, **280**, 1570-1573 (1998).

[36] Brandon, A. D. and Walker, R. J.: *Earth Planet. Sci. Lett.*, **232**, 211-225 (2005).

[37] Holzheid, A., Schmitz, M. D. and Grove, T. L.: *J. Geophys. Res.*, **105** (B5), 13555-13567 (2000).

[38] Ito, E., Morooka, K. and Ujike, O.: *Geophys. Res. Lett.*, **20**, 1651-1654 (1993).

[39] Chabot, N. L. and Drake, M. J.: *Earth Planet. Sci. Lett.*, **172**, 323–335 (1999)

[40] Dubrovinsky, L. S. and Saxena, S. K.: A thermal characteristic of melting in laser heating at high pressure, *High Temp. –High Press.*, **31**, 385-391 (1999).

[41] Boehler, R.: *Nature*, **363**, 534-536 (1993).

[42] Gessmann, C. K., and Wood, B. J.: *Earth Planet. Sci. Lett.*, **200**, 63–78 (2002).

[43] Hillgren, V. J., Drake, M. J. and Rubie, D. C.: *Science*, **264**, 1442-1445 (1994).

[44] Bukowinsky, M. S. T.: *Geophys. Res. Lett.*, **3**, 491-494 (1976).

[45] Lee, K. K. M. and Jeanloz, R.: *Geophys. Res. Lett.*, **30**, 2212, doi:10.1029/2003GL018515 (2003).

[46] McDounough, W. F. and Sun, S. S.: *Chem. Geol.*, **120**, 223-253 (1995).

[47] Buffett, B. A.: *Geophys. Res. Lett.*, **29**, doi:10.1029/2001GL014649 (2002).

[48] Murthy, V. R., van Westrenen, W., and Fei, Y.: *Nature*, **423**, 163–165 (2003).

Method of Automatic Characterization of Inclusion Population by a SEM-FEG/EDS/Image Analysis System

Eric Hénault

CREAS – Research centre of ASCOMETAL

This text describes the system developed to automatically characterize the inclusions observed in polished surfaces of steel samples. A coupling was carried out between a field-emission scanning electron microscope (JEOL, JSM-6500F), an energy-dispersive spectrometer (EDS) (PGT, detector SDD SAHARA) and image analysis software (ADCIS, APHELION). The communication between these elements made it possible to develop software for inclusion measurement. The control functions allow automatic measurements over long periods according to various conditions of observation and analysis. It becomes possible to collect a very large amount of data thus enabling accurate statistical results to be obtained (thousands of analyzed inclusions per day in a clean steel sample). An example is given with improved machinability steels. The knowledge of the distributions and the characteristics of their various inclusion populations permit us to estimate the metal machining behavior.

Introduction

In 2001, ASCOMETAL research centre purchased a field-emission scanning electron microscope. In the list of requirements transmitted to the various suppliers of microscopes, we included the capacity of developing methods of inclusion characterization in an automatic way.

Indeed, until now, no microscope has made possible a complete control of the essential functions (displacement, magnification...) we need for our measurements. However, this demand is essential to obtain precise and statistically exploitable data.

If they are carried out in a manual way, these measurements are often too long and too tedious. For example, it is necessary to measure 300 inclusions to get results with an error lower than 10%, in the case of a homogeneous inclusion distribution. Nevertheless these results are essential for many studies about steels in order to know their properties or to improve the elaboration processes.

Thus, an apparatus running automatically 24 hours per day, and 7 days a week is required.

To achieve this goal, JEOL (microscope), SYNERGIE 4 (EDS system, PGT) and ADCIS (image analysis system APHELION) have collaborated in the development of the control functions necessary for the application to inclusion characterization.

The expected functions, defined in the specifications, were added to the APHELION software as ActiveX components.

ASCOMETAL HAGONDANGE CREAS
Site industriel d'Hagondange, Avenue de France 57301 HAGONDANGE FRANCE
E-mail: e.henault@ascometal.lucchini.com

The application of inclusion characterization was then developed in VISUAL BASIC.NET based upon the APHELION ActiveX components.

The system **(Figure 1**) is more thoroughly described below. The next section is devoted to the benefits provided by the use of a scanning electron microscope compared to the use of an optical microscope. The second section introduces the list of the functions developed for the SEM-FEG/EDS/Image analysis system. Lastly, an example is provided to highlight one among the many possibilities of the system.

Description of the System

Advantages of a field-emission scanning electron microscope

The main limits of the inclusion characterization made by optical microscopy are:
- not very sensitive to the type of inclusion (the morphological criteria are often insufficient),
- the problems involved in the artifacts (dust, scar...),
- the problems involved in the poor depth of field.

Fig. 1 SEM-FEG/EDS/IA system.

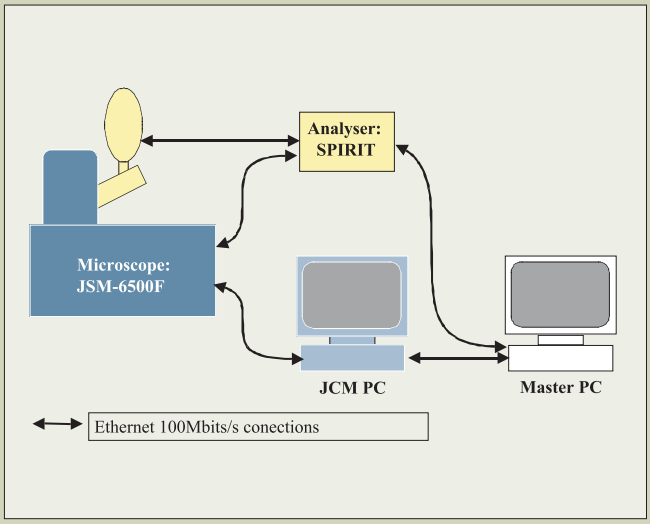

Fig. 2 General diagram of the system.

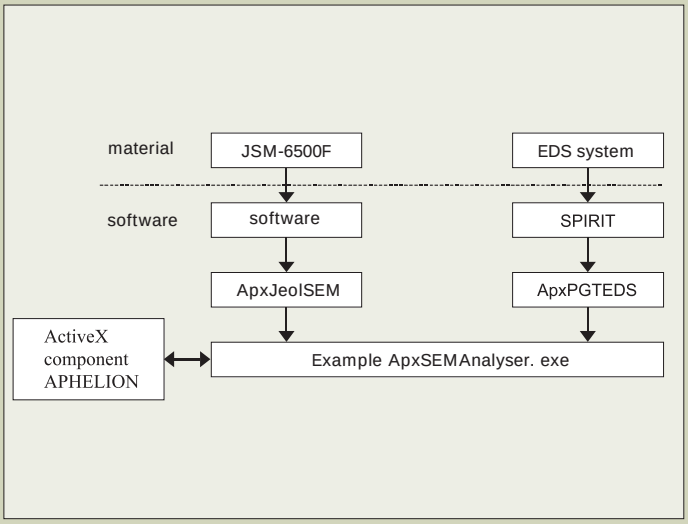

Fig. 3 General structure of the system.

From this non exhaustive list, the specifications of the ideal system for inclusion characterization are:
- signal stability to obtain comparable images,
- stage control to be able to scan a sufficient area in order to obtain statistically representative results,
- magnification control to obtain accurate inclusion sizes whatever the size of the inclusion,
- chemical contrast to discriminate the various inclusion phases,
- chemical composition to discriminate the various inclusion populations,
- resolution suited to detect inclusions smaller than a micrometer,
- improved depth of the field to maintain the image clarity.

We observe that the JEOL JSM-6500F field-emission scanning electron microscope provides these specifications. In particular, its beam can operate for hours without any signal variation. The accuracy of the motorized stage motion allows to detect and to observe the inclusions at various magnifications.

The control functions of the field-emission scanning electron microscope

The general structure of the application is illustrated in **Figure 2**.

The equipment contains two PCs. One is dedicated to the control of the electron microscope. The second, on which SPIRIT software (analysis) and APHELION software (image analysis) are installed, controls the totality of the system. The inclusion characterization application is installed on this PC. The images acquired by SPIRIT are used in the application. The PCs and the various apparatus intercommunicate via Ethernet 100 Mbit/s connections.

Figure 3 illustrates in a simplified way the general structure of the application. It uses the functions of the microscope software, the analysis system (SPIRIT) and the ActiveX components of the image analysis software (APHELION).

The totality of the functions intervening in the application is listed in the following paragraphs a, b and c. The parameters manipulated by these functions are accessible in reading and writing.

a) Control functions of the JSM-6500F microscope:

- X, Y, Z axes movements,
- Rotation of the stage,
- Beam current value,
- Accelerating voltage,
- Magnification,
- Brightness,
- Contrast,
- Autofocus,
- Choice of the detector,
- Data backup of the initial conditions.

b) Control functions of the SPIRIT analyser:

- Positions (x,y) of the measured spectrum,
- Acquisition time of the spectrum,
- Acquisition mode of the spectrum,
- Data backup of the spectrum,
- Choice of the elements to be measured,
- Measurements on the selected elements,
- Automatic search of the elements on the spectrum,
- Size of an image (512, 1024, etc),
- Position and zoom factor,
- Time by pixel,
- Image mode,
- Number of frames to be added,
- Data backup of the image.

c) Image analysis functions:

- Measurement of grey levels values,
- Operators on the images,
- Possibility to use several images,
- Multiple thresholds,
- Morphological functions,
- Segmentations,
- Operators on the binary images,
- Measurements of the parameters.

These functions are necessary for the development of the general application of the characterization of inclusion populations.

General algorithm

The chain of the following principal actions constitutes the algorithm of the method.

Input data:
1 - Choice of the method,
2 - Identification of the samples,
3 - Positions of the samples on the stage,
4 - Positions of the zones of measurements,
5 - Method of focus,
6 - Method of scanning,
7 - Choices of the measurement options,
8 - Method of threshold,
9 - Criteria of chemical analysis,
10 - Backup files.

Measurements:
1 - Acquisition of an image,
2 - Image processing,
3 - Measurements of the parameters,
4 - Saving of the results.

Data processing:
1 - Treatment of the results,
2 - Final documents.

Performance of the system

The application allows to optimize the use of the electron microscope. Some studies require long analyses. They can last several tens of hours. They can be carried out without human intervention thanks to the system set up.

More than 100 inclusions are characterized per hour on a sample with a low inclusion density. Morphological and analytical measurements of each inclusion are saved in a results file. The data are then post-treated according to the nature of the results, adapted to the needs.

We distinguish measurements and treatments to allow multiple exploitations of the results files.

An example of application is proposed in the following paragraph.

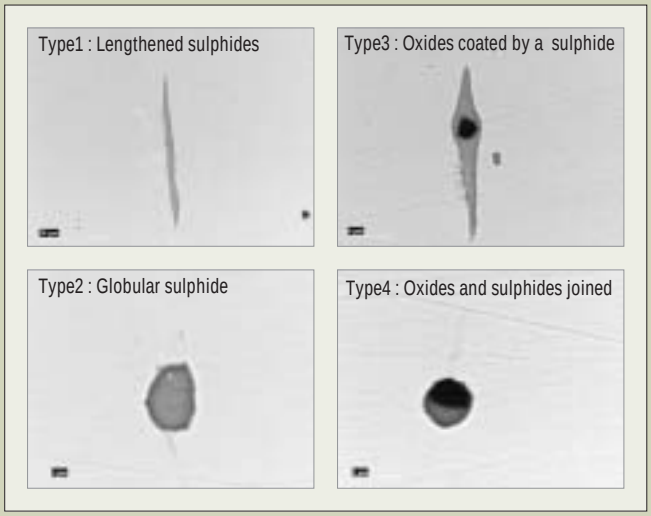

Fig. 4 Inclusion populations.

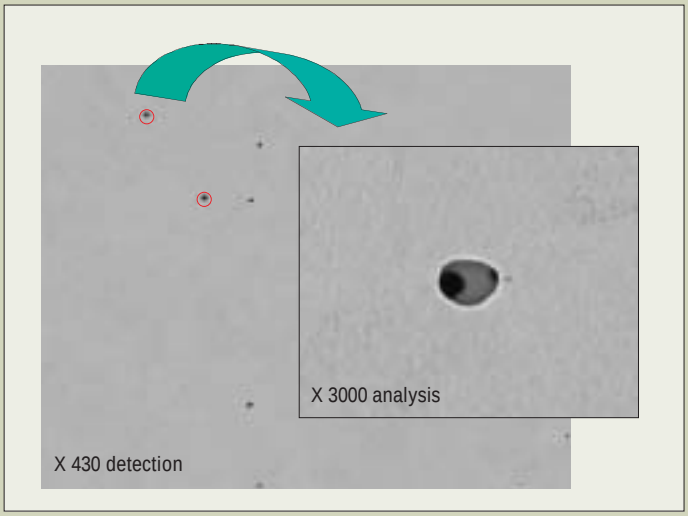

Fig. 5 Inclusion detection.

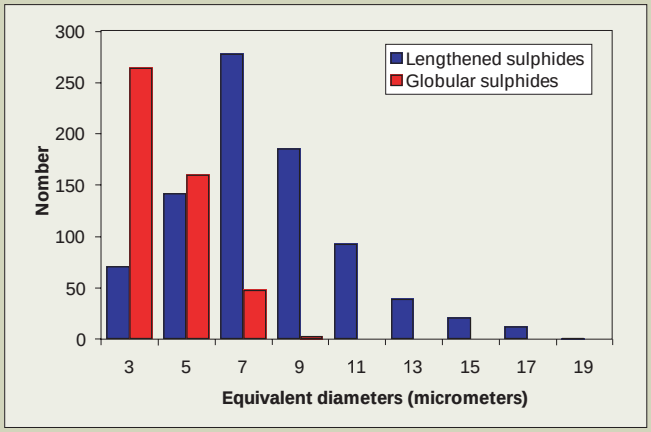

Fig. 6 Histogram of equivalent diameter of sulphides.

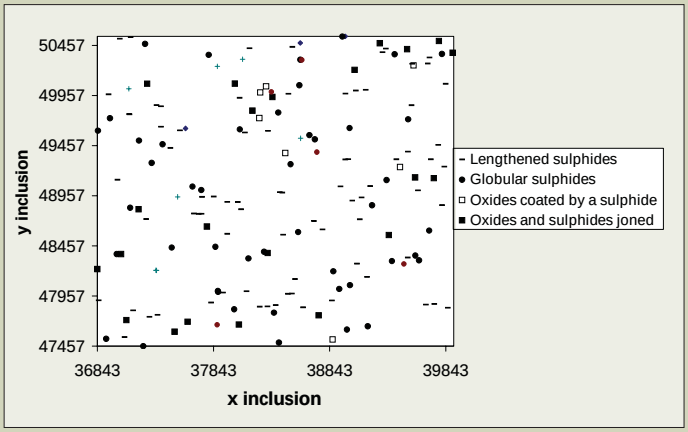

Fig. 7 Inclusion positions.

Application: Characterization of VITAC 3000™ Steels

VITAC 3000™ steels are steel grades subjected to a specific treatment during casting. The goal is to obtain inclusions whose chemical nature, density, size and distribution improve the operations of machinability by limiting the wear on the tools. If one wishes to qualify castings, we can define a method of measurements adapted to the characterization of the various types of inclusions.

The various types included in these grades of steels are (**Figure 4**):

- lengthened sulphides,
- globular sulphides,
- oxides coated by a sulphide,
- oxides and sulphides joined,
- oxides.

The method must allow to distinguish precisely oxide and sulphide phases. It is also necessary to obtain data on the chemical nature of oxides and sulphides.

So, we define a method using the scanning electron microscope and its chemical analysis system. The sample is observed with a scanning magnification which makes it possible to detect and to measure inclusions larger than 3 micrometers in size (**Figure 5**). This magnification is chosen so that enough surface is observed in a reasonable time. In the method used, this magnification is equal to 430, which corresponds to 11 images per mm.

The defined threshold permits to segment the image. The sizes of the objects are measured on the binary image obtained.

The objects whose size is sufficient (small diameter larger than 3 micrometers) are analyzed, automatically (**Figure 5**). Under these conditions of observation, the measurement accuracy is not sufficient. So, each selected object is observed with a higher magnification. This magnification of analysis is higher than 2000 (defined during the setting in data). The stage moves so that each selected inclusion is placed in the centre of the image acquired.

The morphological inclusion parameters and the various phase compositions are then measured. A threshold with two levels permits to isolate oxide and sulphide phases. If the inclusion width is larger than 3 micrometers (the greatest measurement accuracy allows to determine it), a chemical analysis of the different phases is made. The analysis time is equal to a few seconds. These measurements are made for each phase either in the geodetic center of the objects or by a scanning on the area.

Measurements are obtained from a sufficient area of the surface to reach the quality of results required from the statistical point of view.

The data file about inclusion parameters is then treated in an automatic way in order to determine the characteristic values of the various inclusion types. For examples, **Figure 6** represents the histograms of the equivalent diameters of lengthened sulphides (type 1) and of globular sulphides (type 2). In **Figure 7**, one can observe the positions of inclusions which were detected on the observed surface.

Conclusions

The inclusion characterizations of steels are essential to classify the products or for the improvement of the processes of the steel plant.

When precise data about small size inclusion populations are expected, it is then necessary to analyze a significant area of a polished sample to attain a satisfactory precision in the results.

To achieve this goal, the automation of the scanning electron microscope coupled to an EDS (energy-dispersive spectrometer) system and a very complete software of measurements were developed. This software permits fast and precise measurements of a very significant number of inclusions considering the measurement conditions defined by the operator beforehand.

Indeed, having thorough input data makes it possible to describe all the methods that can be used in our domain. The automated application gives an optimal use of the microscope and its analysis system.

Direct Observation of Biomolecular Complexes by Cold-Spray Ionization Time-of-Flight Mass Spectrometry

Noriko Nagahori and Shin-Ichiro Nishimura

Graduate School of Advanced Life Science, Hokkaido University

Introduction

Many biological processes are regulated by the specific and noncovalent intermolecular recognition between enzyme–substrate, antigen–antibody, receptor–ligand, carbohydrate–protein, and carbohydrate–carbohydrate. The direct observation of these biomolecular interactions is important for understanding the mechanisms behind these biological processes.

Electrospray ionization mass spectrometry (ESI MS) is an important tool for the investigation of noncovalent complex formation [1-6]. The advantages of MS over traditional methods such as UV/Vis spectroscopy, fluorescence spectroscopy, surface plasmon resonance (SPR), isothermal titration microcalorimetry (ITC), and nuclear magnetic resonance (NMR) spectroscopy include the accuracy of mass measurement, speed of analysis and small sample quantities. However, the harsh conditions of the ionization process in MS are often detrimental to the survival of noncovalent and unstable biomolecular interactions between sugar-protein, sugar-sugar and sugar-water complexes.

Recently, Yamaguchi and co-workers developed cold-spray ionization mass spectrometry (CSI MS) [7, 8] which does not require heat or an electric field and provides a snapshot of the state of compounds in solution. It is suggested that a cooled ion spray promotes stable solvation-ionization processes through increased compound polarizability by higher dielectric constants at low temperature. Using the CSI system, facile and precise characterization of labile self-assembling nanostructures and unstable organometalic complexes in solution was achieved [9, 10]. CSI MS may become one of the most promising and versatile tools for characterization of a variety of weak but specific biomolecular interactions, as ionization at a low temperature (–20°C) allows direct observation of unstable large-scale aggregates of amino acids or nucleosides in organic solvents with a magnetic-sector-equipped instrument [11-13]. Moreover, CSI MS combined with an orthogonal acceleration time-of-flight (oa-TOF) mass analyzer extends the applicability of this method to the characterization of the dynamic interactions of biomacromolecules. This is possible through a number of attractive features of TOF MS analyzers, such as their theoretically unlimited mass range, very high spectrum acquisition rates, high ion transmission, high sensitivity, multiplex detection capacity, reasonable mass resolution and simplicity in instrument design.

Our interest is focused on the potential of CSI-TOF MS, with particular attention to specific and weak biomolecular interactions in water at a low temperature. We have previously tried to monitor directly the formation of noncovalent protein-carbohydrate, carbohydrate-carbohydrate and carbohydrate-water complexes in an aqueous solution [14].

Frontier Research Center for Post-genomic Science and Technology, Hokkaido University
North 21, West 11, Sapporo, 001-0021, Japan
E-mail: shin@glyco.sci.hokudai.ac.jp

Carbohydrate-Protein Interaction

Among the biomolecular interactions involving carbohydrates, carbohydrate-protein interactions are well known and widely studied. For example, fertilization, cell adhesion, viral infections etc, are mediated by carbohydrate-protein interactions [15]. Thus a high-throughput and sensitive method to analyze carbohydrate-protein interactions contributes to the development of novel compounds (carbohydrates) and drug candidates that have a strong affinity for target proteins as well as promoting the deep understanding of basic biological functions.

We used the CSI-TOF MS to achieve high-throughput analysis of carbohydrate-protein interaction. The effect of temperature on complex formation between hen egg lysozyme and the chitooligosaccharide, chitotetraose is shown in **Figure 1a**. As anticipated, the intensity of the signal that corresponds to the lysozyme-chitotetraose complex was gradually enhanced by lowering the ion spray temperature of the reaction mixture from 200 to 4°C. It seems that the dissociation of carbohydrate-protein interaction was repressed. As shown in **Figure 1b**, CSI-TOF MS is quite an efficient and simple method for the determination of the dissociation constants of protein-ligand interactions, since it does not require the use of molecular probes. In fact, the K_d of lysozyme with chitotetraose was determined to be 1.6×10^{-5} M, which is in good agreement with data reported previously [16]. Furthermore, CSI-TOF MS can be used to search for a compound that shows the highest affinity for the target protein in a mixture of several oligosaccharides by making a simple "snapshot assay". As illustrated in **Figure 2a**, lysozyme interacted selectively with chitooligosaccharides $(GlcNAc)_3$, $(GlcNAc)_4$ and $(GlcNAc)_5$ at 4°C in a compound library containing 23 different oligosaccharide types. Such valuable information could not be obtained by traditional ESI-TOF MS techniques carried out at 200°C as shown in **Figure 2b**. Moreover, when a compound library void of chitooligosaccharides was assayed at 4°C, lysozyme showed a significant affinity toward the maltooligosaccharides $(D\text{-glucose})_{3\text{-}7}$ and γ-cyclodextrin (**Figure 2c**). These interactions cannot be detected by using general spectroscopic methods such as UV/Vis, fluorometric, and SPR. **Figure 3a** shows binding between lysozyme and maltotriose ($(Glc)_3$) (*m/z* 1646.3, $[M+9A]^{9+}$ and 1851.9, $[M+8A]^{8+}$, "A" means ion adduct). Although the interaction is weak and is considered non-specific, the CSI data instead indicate specific binding. The results of a competition experiment (**Figures 3a** and **3b**) suggest that maltotriose binding involves the same

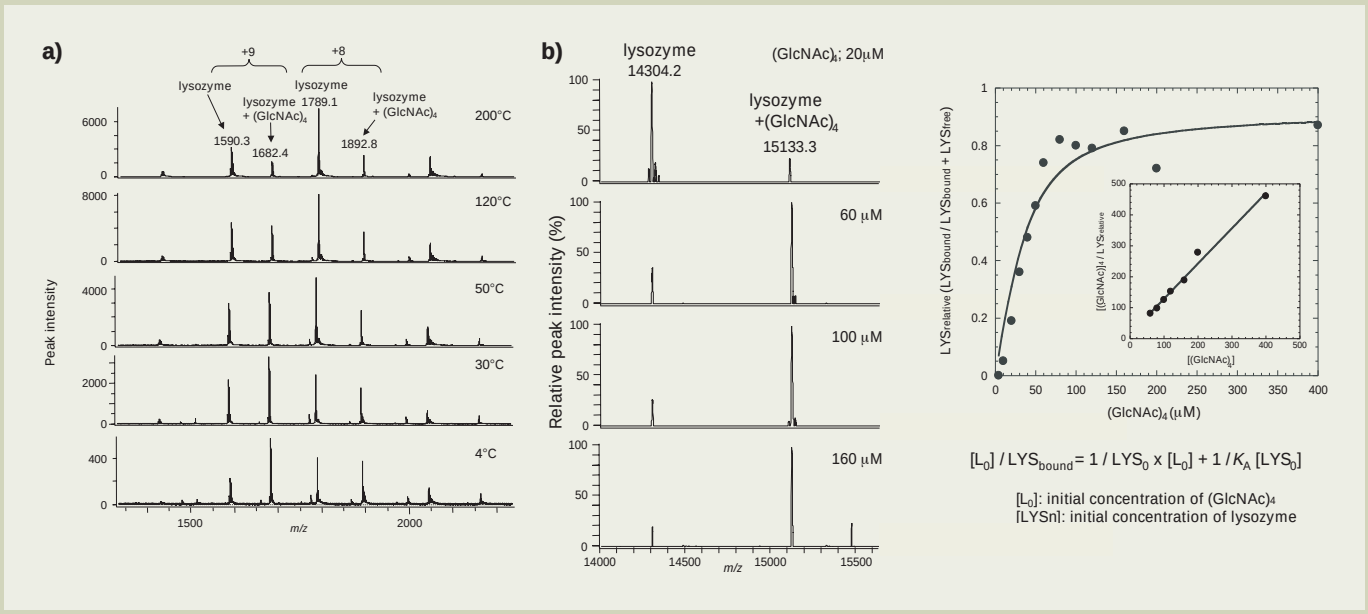

Fig. 1 Interaction of hen egg lysozyme with chitooligosaccharide.
a) Temperature dependency of the signal intensities of the lysozyme-chitotetraose ($(GlcNAc)_4$) complex in ESI (CSI) MS. Spray temperatures are indicated. [Lysozyme] = 35 μM, [$(GlcNAc)_4$] = 200 μM.
b) The binding of lysozyme with chitotetraose at 4°C. [Lysozyme]=35 μM. The $(GlcNAc)_4$ concentrations are indicated. The peak intensities from the mass spectra were used for the determination of the relative amount of bound lysozyme as a function of [$(GlcNAc)_4$], and a sample Kd determination is shown at the bottom. GlcNAc = N-acetyl-D-glucosamine.

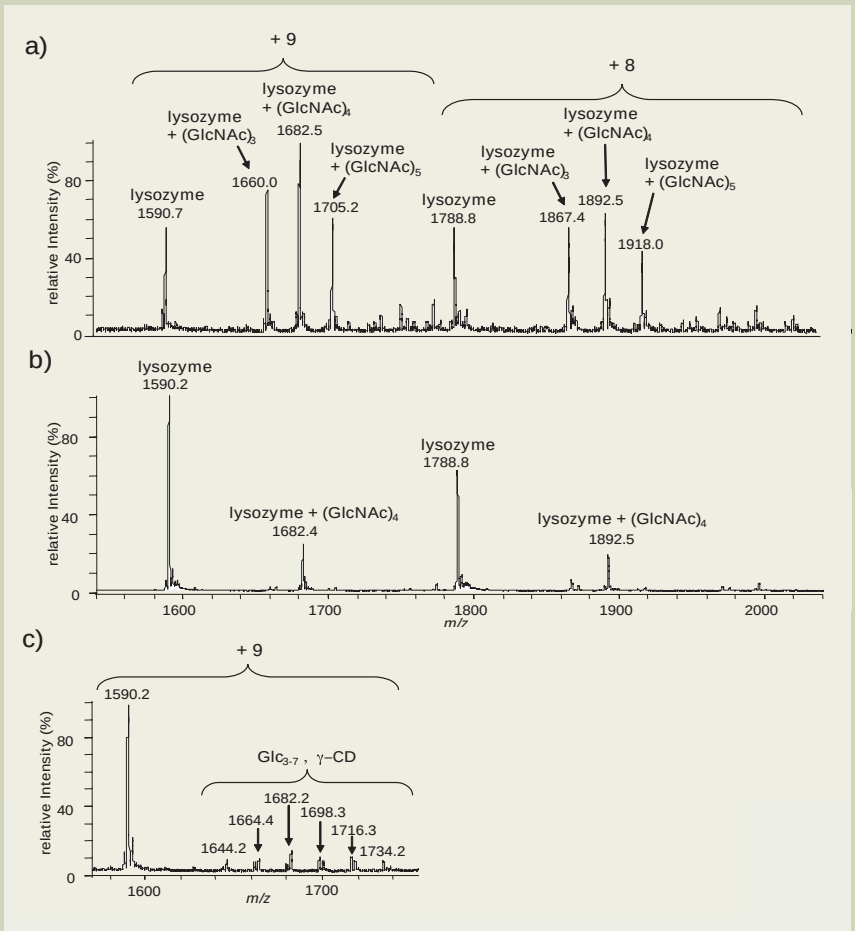

Fig. 2 Carbohydrate-protein complex screening. The interaction of lysozyme with an oligosaccharide library containing GlcNAc, $(GlcNAc)_2$, $(GlcNAc)_3$, $(GlcNAc)_4$, $(GlcNAc)_5$, Glc, $(Glc)_3$, $(Glc)_4$, $(Glc)_5$, $(Glc)_6$, $(Glc)_7$, cellobiose (Glcβ1,4Glc), lactose (Galβ1,4Glc), methyl a-mannoside, $(Man)_5$, D-glucosamine, L-arabinose, lacturose, xylose, L-gluconolactone, α-CD, β-CD, and γ-CD (all 35 μM) was monitored by CSI-TOFMS at a) 4°C and b) ESI-TOF MS at 200°C. c) CSI-TOFMS analysis of lysozyme with a oligosaccharide library lacking chitooligosaccharides [$(GlcNAc)_2$, $(GlcNAc)_3$, $(GlcNAc)_4$, and $(GlcNAc)_5$] at 4°C. [Lysozyme]= 35 μM.

lysozyme cavity as for chitotriose $(GlcNAc)_3$. This is supported by computer-assisted docking simulations carried out in our laboratory (**Figure 3c**). Notably, CSI-TOFMS can be employed to search for unexpected ligand candidates with "specific and low affinity" for a target protein. Identified ligands could then be applied as scaffold molecules for designing new drugs (inhibitors) with a high potential for success.

Carbohydrate-Carbohydrate Interaction

Carbohydrate-carbohydrate interaction might be a crucial step in cell-cell interaction that leads to cellular differentiation, cell growth, and malignant alterations [17]. Lewis x trisaccharide (Le^x) has been reported to form a self-assembly through carbohydrate-carbohydrate interaction in the presence of Ca^{2+} ions involving the adhesion of blastomeres. We demonstrated the direct observation of carbohydrate-carbohydrate interaction of Le^x trisaccharide by using CSI-TOF MS. As shown in **Figure 4**, CSI-TOFMS spectra measured at 4°C clearly demonstrate that Le^x trisaccharides

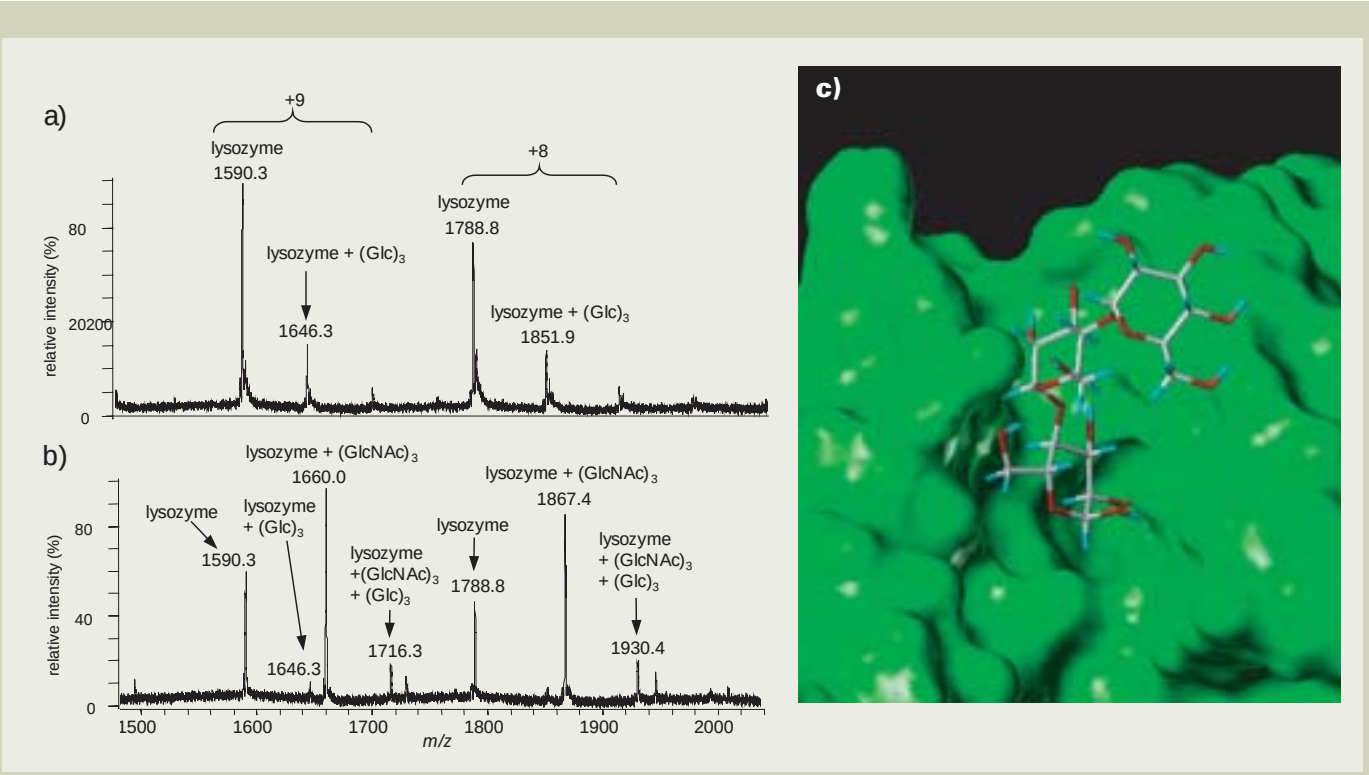

Fig. 3 Evaluation of lysozyme-maltotriose interaction by CSI-TOFMS at 4°C. a) The binding of lysozyme (35 µM) with $(Glc)_3$ (100 µM). b) Competitive binding assay of $(Glc)_3$ and $(GlcNAc)_3$ toward lysozyme. c) Docking simulation of maltotriose $(Glc)_3$ with the subsite of lysozyme. (SYBYL FlexX module)

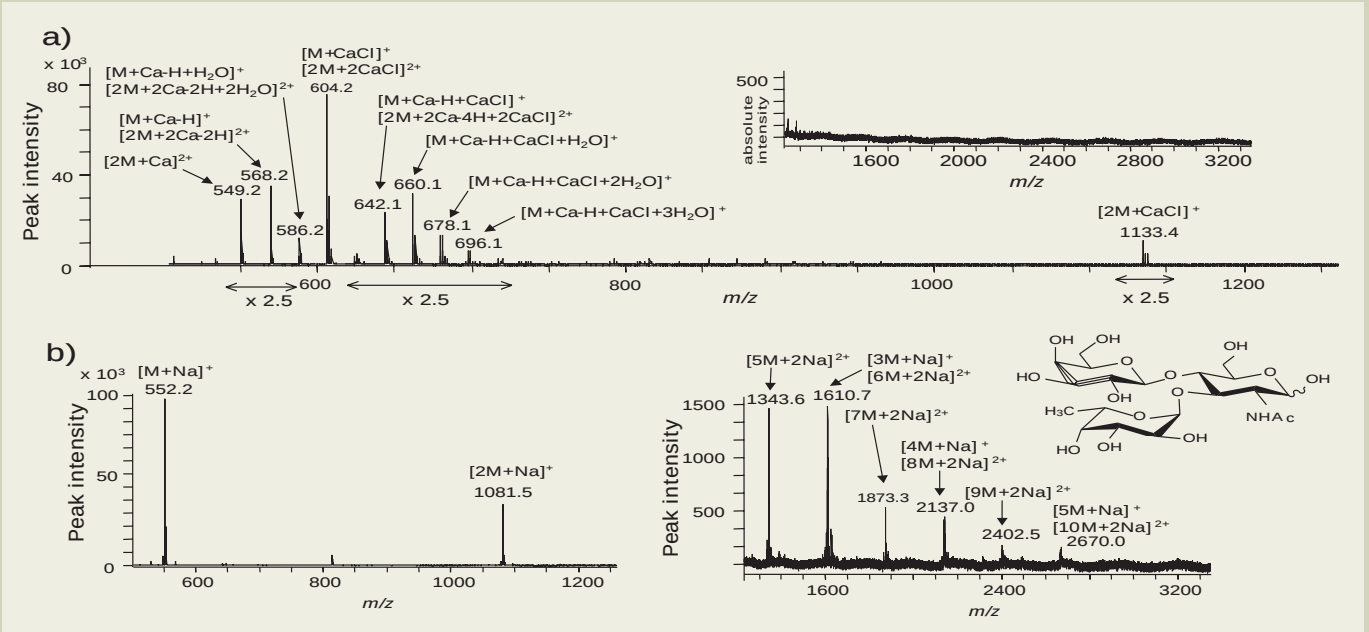

Fig. 4 CSI-TOF mass spectra of the Le^x self-assembly at 4°C a) in the presence of Ca^{2+} and b) in the absence of Ca^{2+}. The experiments were performed by injecting 20 µl (3.8 nmole of Le^x) of Le^x-$CaCl_2$ stock solution ([Le^x]=190 µM and [$CaCl_2$]=1.0 µM).

preferentially dimerize by binding to Ca^{2+} ions, and that in the absence of Ca^{2+}, Le^x trisaccharides form a range of large aggregates of up to 10 trisaccharide units (*m/z* 2670.0, $[10Le^x + 2Na]^{2+}$) (**Figure 4b**). Several ion peaks shown in **Figure 4a** are evidence for the preferential Le^x-Ca^{2+} complex formation such as $[Le^x + Ca - H]^+$, $[Le^x + Ca - H + H_2O]^+$, and $[Le^x + CaCl]^+$. The ion peaks of $[2Le^x + Ca]^{2+}$, $[2Le^x + 2Ca - 2H + 2H_2O]^{2+}$, and $[2Le^x + 2CaCl]^{2+}$ provide valuable information that reveals the mechanism of Le^x-Le^x dimerization in the presence of Ca^{2+} ions. The use of CSI-TOF MS is key to elucidating the mechanism of carbohydrate-carbohydrate interaction.

Glycoprotein-Water Interaction

Anti freeze glycoprotein (AFGP) is a tandem repeating glycopeptide exhibiting an inhibition effect on the ice crystal growth. Monomeric *sy*$AFGP_1$ does not have antifreeze activity and the minimal active structure of the antifreeze glycopeptide was found to be (*sy*$AFGP_3$) with three repeats [18]. We thought that the interaction between AFGP and water molecules may be related to the antifreeze activity of AFGP, and tried direct observation of AFGP-water complexes by using CSI-TOF MS (**Figure 5**). It appears that the active *sy*$AFGP_3$ forms specific complexes with three water molecules, whereas the inactive monomeric *sy*$AFGP_1$ produced neither the complex with water nor the self-aggregation found in the Le^x trisaccharide. Hydration of *sy*$AFGP_3$ at 4°C observed as *m/z* 949.4 $[M + 3H_2O + 2H]^{2+}$, *m/z* 960.4 $[M + 3H_2O + H + Na]^{2+}$, and *m/z* 968.4 $[M + 3H_2O + H + K]^{2+}$ by CSI-TOFMS may become an important way to investigate AFGP binding with the ice (water) lattice, and hence the mechanism of its antifreeze. As indicated in **Figure 5 (c)**, when fully deuterated *sy*$AFGP_3$ with D_2O as the solvent was observed, an analogous spectrum with the "water signals" shifted by 20 Da instead of 18 Da was obtained. This is evidence that the binding of three water molecules is favored over the binding of just one or two.

Mechanism of Dynamic Inhibitor for Glycosyltransferase

Glycosylation conducted by glycosyltransferases is one of the crucial biological processes for the post-translational modifications of proteins and lipids. Selective inhibitors of glycosyltransferases are therefore of interest because they may lead to the development of novel and potential therapeutic reagents. The

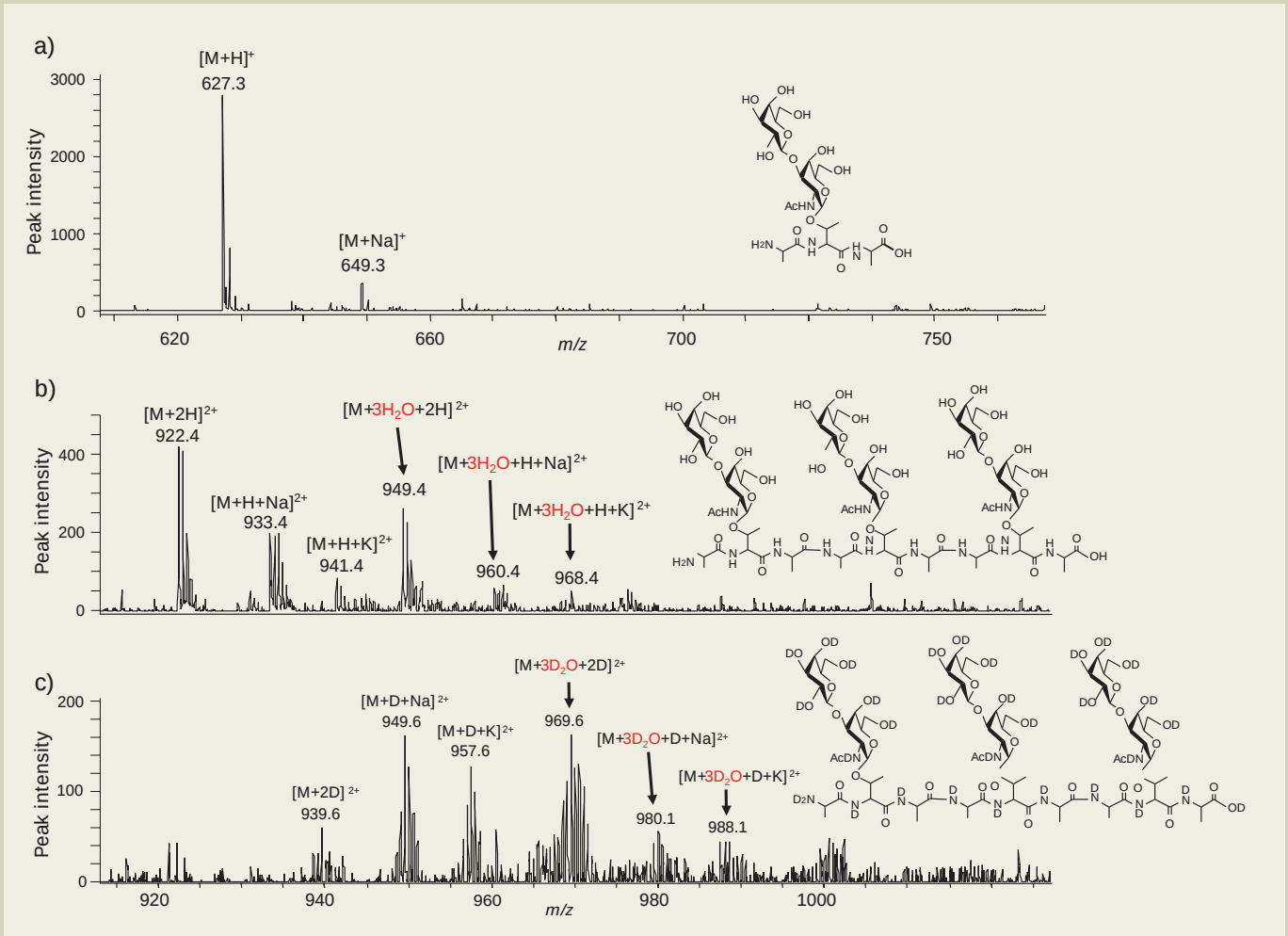

Fig. 5 Direct observation of the specific interaction of *sy*$AFGP_3$ with water at 4°C. CSI-TOFMS of a) monomeric AFGP (*sy*$AFGP_1$) and b) trimeric AFGP (*sy*$AFGP_3$) in water, and c) *sy*$AFGP_3$ in D_2O. AFGP injection volume (20 µl) contained 320 pmole AFGP. [AFGP]=16 µM.

complex and dynamic reaction mechanism of glycosyltransferases involves many components such as a sugar nucleotide as a donor substrate, an acceptor sugar substrate, and a metal ion [19]. We had synthesized a novel dynamic inhibitor for β1,4-galactosyltransferase and analyzed the inhibition mechanism using CSI-TOF MS [20]. Inhibitor **1** was designed and synthesized based on the crystal structure of bovine β1,4-galactosyltransferase (β-GalT1). It is known that β-GalT1 undergoes critical conformational changes upon glycosyl donor substrate binding. First, tryptophan 314 located in the small flexible loop near the active site moves toward the catalytic pocket to interact with the complex of the donor substrate and Mn^{2+} ion. This movement leads to conformational changes in the enzyme, which are essential for the subsequent acceptor-substrate binding. We hypothesized that the naphthalene group linked to the galactose residue of inhibitor 1 strongly binds to the typ 314 to stop the conformational change of the enzyme, resulting in the inhibition of the acceptor-substrate binding. The inhibitory activity of **1** was determined by HPLC analysis, Ki = 1.86 μM. If the hypothesis that inhibitor **1** stops the conformational change of the enzyme is correct, the βGalT1-inhibitor **1** complex does not show any binding capacity with the acceptor sugar substrate. We verified this by direct observation of the enzyme-substrate complex using CSI-TOF MS **(Figure 6)**. The complex of βGalT1 with UDP-Gal and Mn^{2+} (*m/z* 3044.1) shifted to the peak at *m/z* 3030.10 due to GalT1-UDP-Mn^{2+} and to the peak at *m/z* 3073.1 corresponding to the molecular mass for the complex of GalT1-UDP-Mn^{2+} -acceptor substrate **2**. On the other hand, the complex of bGalT1 with inhibitor **1** and Mn^{2+} (*m/z* 3066.6) exhibited no binding capacity toward an acceptor substrate **2**. These results agree with our hypothesis that inhibitor **1** prevents the binding of the acceptor substrate with βGalT1 and this is the first demonstration of the observation of enzyme mechanism without any probe molecule.

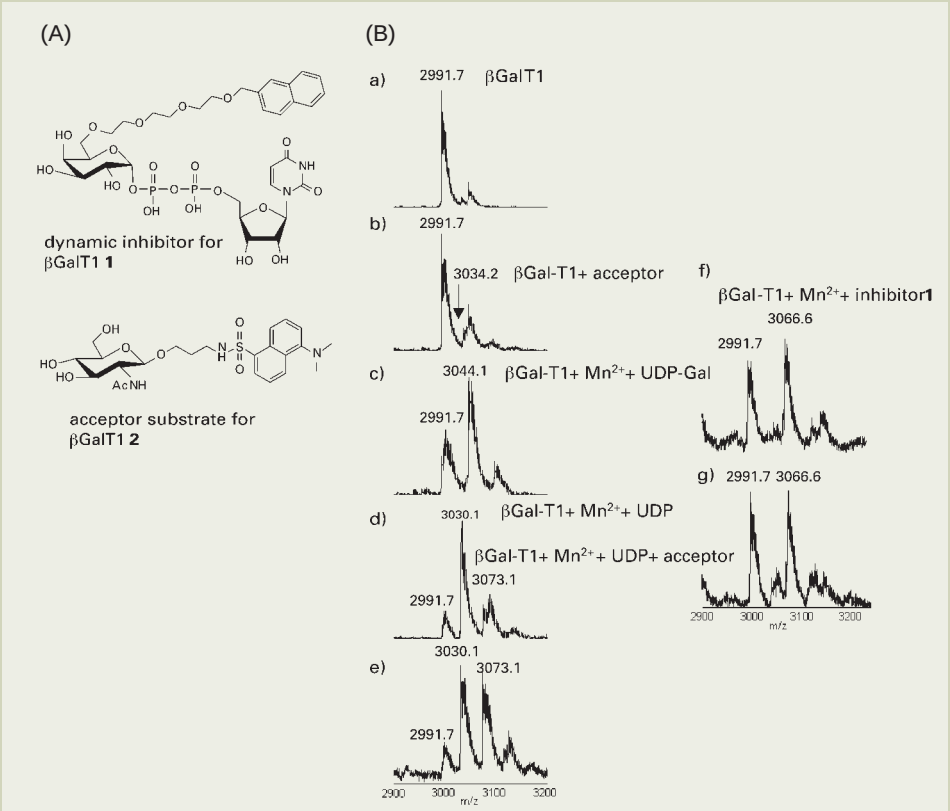

Fig. 6 Evidence of competitive inhibition by inhibitor **1** in the dynamic conformational change of β-GalT1 detected by CSI-TOF MS at 37°C.
(A) Structure of inhibitor **1** and acceptor substrate **2**.
(B) a) Ion peak at *m/z* 2991.7 shows $[M+12H]^{12+}$ of βGal-T1 (95 pmol). b) Spectrum of βGal-T1 (95pmol) in the presence of acceptor substrate **2** (450 pmol). c) Spectrum of βGal-T1(95 pmol) in the presence of UDP-Gal (400 pmol). A significant signal corresponding to the βGalT1-Mn^{2+}-UDP-Gal complex was observed at *m/z* 3044.1. d) A typical spectrum of bGal-T1 (95 pmol) obtained in the presence of both) UDP-Gal (40 pmol) and acceptor substrate **2** (450 pmol). The ion peaks due to βGalT1-Mn^{2+}-UDP (*m/z* 3030.1) and the complex of βGalT1-Mn^{2+}-UDP-acceptor substrate **2** (*m/z* 3073.1) were observed. e) A spectrum of βGal-T1 (95 pmol) in the presence of excess amount of acceptor substrate. Acceptor substrate **2** (450 pmol) was added to the complexes formed in an experiment d). The signal intensity, due to the complex of βGalT1-Mn^{2+}-UDP-acceptor substrate **2**, was drastically enhanced. f) The spectrum of bGal-T1 (95 pmol) in the presence of inhibitor **1** (400 pmol). A significant signal corresponding to the complex of GalT1-Mn^{2+}-inhibitor **1** (*m/z* 3066.6) was observed. g) The effect of the addition of an acceptor **2** (450 pmol) to the complex of GalT1-Mn^{2+}-inhibitor **1.**

Summary

We found that CSI-TOF mass spectrometry is a highly sensitive and reliable method for analyzing specific non-covalent complexes of glycoconjugates under non-disruptive conditions. The results reported herein demonstrated the ability and versatility of CSI-TOFMS for the direct monitoring and characterization of weak and specific carbohydrate-related interactions in an aqueous solution at low temperature. This novel technique provides us not only with the basic insights into the mechanism of biomolecular recognition, but also with valuable information for high throughput molecular searching for bioactive key compounds for the discovery of new drugs.

References

[1] J. B. Fenn.: *Angew. Chem. Int. Ed.*, **42**, 3871 (2003).
[2] J. B. Fenn, M. Mann, K, Meng, S. F. Wong and C. M. Whitehouse.: *Science*, **246**, 64 (1989).
[3] B. Genem, Y. T. Li and J. D. Henion.: *J. Am Chem. Soc.*, **113**, 6294 (1991).
[4] V. Katta, and B. T. Chait.: *J. Am Chem. Soc.*, **113**, 8534 (1991).
[5] M. Baca, and S. B. H. Kent.: *J. Am Chem. Soc.*, **114**, 3992 (1992).
[6] P. Kebarle and L. Tang.: *Anal. Chem.*, **65**, 972A (1993).
[7] S. Sakamoto, M. Fujita, K. Kim and K. Yamaguchi.: *Tetrahedron*, **56**, 995 (2000).
[8] K. Yamaguchi.: *J. Mass. Spectrom.*, **38**, 473 (2003).
[9] S. Sakamoto, T. Imamoto and K. Yamaguchi.: *Org. Lett.*, **3**, 1793 (2001)
[10] Y. Yamanoi, Y. Sakamoto, T. Kusukawa, M. Fujita, S. Sakamoto and K. Yamaguchi.: *J. Am Chem. Soc.*, **123**, 980 (2001).
[11] S. Sakamoto, K. Nakatani, I. Saito and K. Yamaguchi.: *Chem. Commun*. 788 (2003).
[12] S. Sakamoto and K. Yamaguchi.: *Angew. Chem. Int. Ed.*, **42**, 905 (2003).
[13] M. Kunimura, S. Sakamoto and K. Yamaguchi.: *Org. Lett.*, **4**, 347 (2002)
[14] S. -I. Nishimura, N. Nagahori, K. Takaya, Y. Tachibana, N. Miura and K. Monde.: *Angew. Chem. Int. Ed.*, **44**, 571 (2005).
[15] R. A. Dwek.: *Chem. Rev.*, **96**, 683 (1996)
[16] M. Schindler, Y. Assaf, N. Sharon and D. M. Chipman.: *Biochemistry*, **16**, 423 (1977).
[17] S. Hakomori.: *Glycoconj. J.*, **21**, 125 (2004).
[18] Y. Tachibana, G. L. Fletcher, N. Fujitani, S. Tsuda, K. Mondeand and S. -I. Nishimura.: *Angew. Chem. Int. Ed.*, **43**, 856 (2004).
[19] B. Ramakrishnan and P. K. Qasba.: *J. Mol. Biol.*, **310**, 205 (2001).
[20] K. Takaya, N. Nagahori, M. Kurogochi, T. Furuike, N. Miura, K. Monde, Y. C. Lee and S. -I. Nishimura.: *J. Med. Chem.*, **48**, 6054 (2005).

Methods of Evaluating Activity of Photocatalytic Materials Using Electron Spin Resonance (ESR) Spectroscopy

Yumi Nakai

Analytical Instruments Division, JEOL Ltd.

As the environmental-pollution problem is becoming increasingly serious, society now demands the development and application of environment-purification materials. In order to achieve this mission, a number of national research laboratories and private industries are pursuing research on these materials. Titanium dioxide (TiO_2), a typical photocatalytic material, is applied to various products as a energy-free environment-purification material. In this paper, the author introduces the progress of the method of evaluating its photocatalytic functions.

A Photocatalyst produces a free radical by irradiation, and this radical decomposes harmful substances. This reaction is applied to boards for micro-printing on electronic devices as well; therefore, TiO_2 is a useful industrial material that can be utilized for a wide range of applications. However, the evaluation of its performance is said to provide an insufficient accuracy, because the evaluation is carried out by actually measuring the oxidization rate of specific substances, such as methylene blue (MB) and nitric oxide (NO), with a long measurement time.

The Electron Spin Resonance (ESR) spectrometer is the only instrument enabling one to directly observe a free radical which is the main source of oxidization. The principle of ESR is suitable for the evaluation of photocatalysts; however previously, there were several problems with the measurements. Recent technological advancements in ESR have solved these problems, making it possible to carry out practical evaluations. That is, using ESR, one can directly quantify radical production that is an essential part of the photocatalytic mechanism. Taking advantage of this scheme, the evaluation of photocatalysts for very thin films, whose demands are expected to increase in the future, can be performed more accurately and speedily than with conventional evaluation techniques. In this paper, the author presents several examples of evaluations. By applying ESR, the development of various photocatalytic materials such as TiO_2 is expected to advance.

Introduction

TiO_2, known as a photocatalyst, was conventionally used as a white pigment for various applications. At the end of 1960s, Fujishima, Honda and co-workers discovered that when a photoelectrode reaction is performed using TiO_2, water is decomposed by an electrolysis [1, 2]. Since this discovery, new applications of TiO_2 emerged. One is a new energy supply technique which decomposes water using the solar-light energy and then convert it into the H_2 energy. Another is to decompose harmful organic substances using light, as an environment-purification material. As the awareness of ecology is increasing worldwide, photocatalysts have been attracting interest as energy-free environment-conservation materials. At present, a variety of products contain photocatalysts in the fields of water purification, decomposition of bad-odor gas and sick-house gas, removal of soil contaminants, and measures for anti-bacteria and anti-molds. Furthermore, in the future, photocatalysts are expected to extend their usage to medical care and electronics. The market for these fields reaches about 50 billion yen (as of 2004) and also, there is a prediction that this market wiexceed 100 billion yen in a few years.

Features of TiO_2

TiO_2 is a white microcrystal with high melting point. This is a chemically stable substance that dissolves only in hot concentrated sulfuric acid. In addition, TiO_2 is a semiconductor with a relatively high band gap and features a high refractive index. TiO_2 possesses three crystalline forms: rutile, anatase and brookite. Since brookite is unstable, rutile and anatase are widely used for industrial use. The band-gap energy of anatase is 3.2 eV and that of

JES-FA200 Electron Spin Resonance Spectrometer

rutile is 3.0 eV (3.2 eV for brookite). These band-gap energies correspond to the light energy of the ultraviolet (UV) range. This indicates that TiO_2 absorbs UV and enters a high-energy state, then it possesses a photocatalytic activity. Because anatase has higher band-gap energy, it is thought to be more active than rutile as a photocatalyst. This results in the fact that anatase is used mainly as a photocatalyst, whereas rutile is used in other industrial products.

Mechanism of Photocatalyst

The catalytic mechanism of photocatalyst (TiO_2) is thought to derive from the free radicals produced by TiO_2. This mechanism is illustrated in **Fig. 1**. When TiO_2 is irradiated with UV, a hole and an electron are generated. They react with water and oxygen in the environment, producing hydroxyl radical ($HO^{\bullet}$) and superoxide anion radical ($O_2^{\bullet -}$) respectively. Since $HO^{\bullet}$ is a highly reactive free radical, it oxidizes and decomposes surrounding organic materials. $O_2^{\bullet -}$ itself is less reactive, but it reacts with water in the environment and generates hydrogen peroxide (H_2O_2). Then, H_2O_2 is decomposed by UV to produce $HO^{\bullet}$. This $HO^{\bullet}$ also has the decomposition activity as $HO^{\bullet}$ generated by the hall does. Based on these processes, if the $HO^{\bullet}$ production is quantified, one can acquire the decomposition activity of TiO_2 products. This is the reason why ESR is thought to be suitable for the evaluation of photocatalytic activity.

Methods of Evaluating Photocatalytic Activity

Methods of evaluating the photocatalytic activity of TiO_2 are compared between the conventional and ESR methods, as follows.

Conventional evaluation methods

Two typical methods of evaluating photocatalysts, the MB decomposition method and the NO removal method, are presented in **Figs. 2** and **3**. The former method is applied in an aqueous solution, whereas the latter method is used in the air. Both of these methods utilize

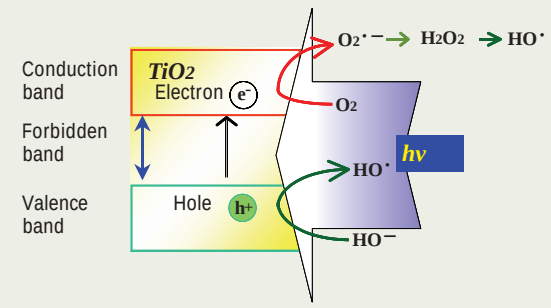

Fig. 1 Mechanism of free radical production by TiO_2 induced by ultraviolet irradiation.

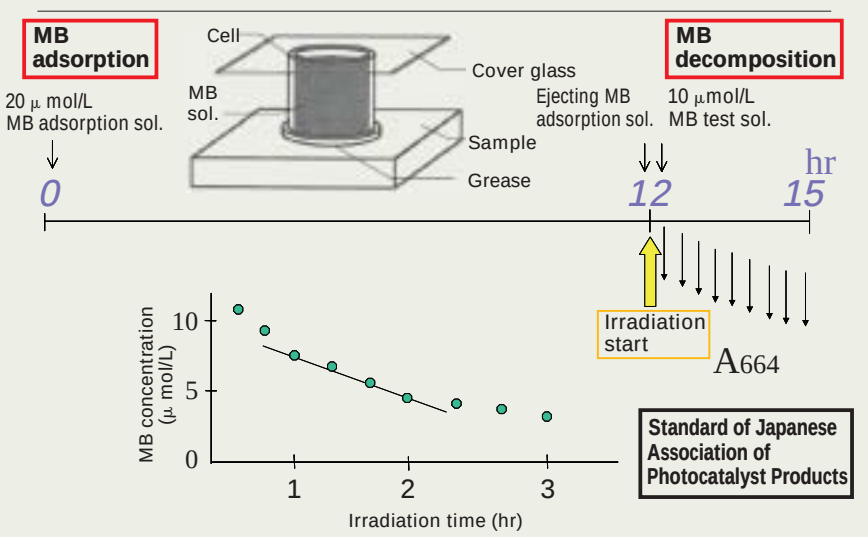

Fig. 2 Method of evaluating the photocatalytic activity of photocatalyst (1) MB decomposition method.

If MB is adsorbed to a sample, this leads to the superficial decomposition, so the adsorption must be saturated in advance. It needs a pre-treatment, a 20 μ mol/L of MB solution is introduced into the cylinder and it is left for 12 hours. After that, the MB solution is taken out and a 10 μ mol/L of new MB test solution is introduced again into the cylinder. Part of the MB test solution is taken out at intervals of 20 minutes after the start of irradiation, and A664 nm is measured using a spectrophotometer. This measurement is continued for 3 hours, then the measurement result is plotted on a graph to obtain the inclination for the 4 successive points that reflect a liner decrease in absorbance. This value is determined as the decomposition activity of the sample.

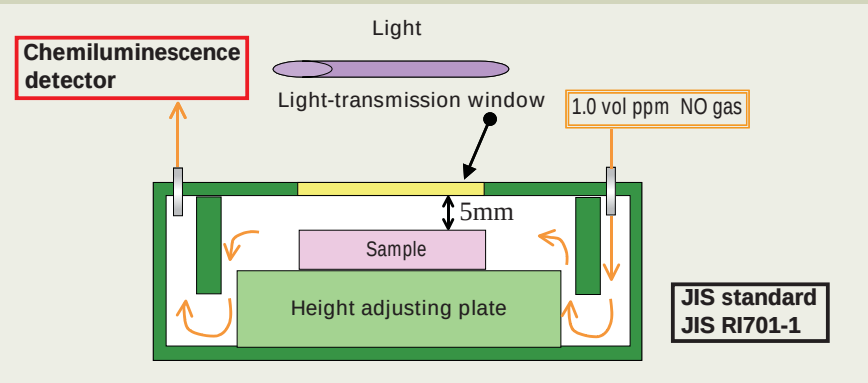

Fig. 3 Method of evaluating the photocatalytic activity of photocatalyst (2) NO removal method.

A photocatalyst product sample is placed in a chamber that has a light-transmission window on its upper surface, then NO gas of 1.0 vol ppm (air-mixed gas with a water-vapor concentration of 1.56 vol%) is continuously introduced through the inlet of the chamber. After 30 minutes of the equilibration of the sample and the NO gas, irradiation is conducted for five hours. The concentrations of NO and NO_2 that flow out from the outlet of the chamber are continuously measured using a chemiluminescence detector.

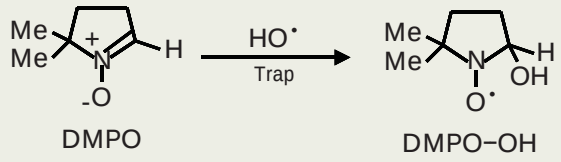

DMPO DMPO−OH

Fig. 4 ESR spectrum of DMPO-OH.

A spin-trap reaction causes the unpaired electron located in HO• are inherited to N-O in DMPO, forming a stable nitroxide radical. This is affected by the nuclear spin of an adjacent N atom and the nuclear spin of H in the β position, giving four lines of signals (intensity ratio 1 : 2 : 2 : 1). The horizontal axis indicates the strength of an external magnetic field applied to the sample, whereas the vertical axis expresses the absorption spectrum of a microwave in the deferential form by magnetic-field modulation and phase detection. Thus, the central horizontal axis is taken as a base line, providing signals upward and downward. For the quantification of DMPO-OH, the signal intensity of either one line is measured. Typical ESR measurement conditions are as follows: Microwave frequency: 9.42 GHz, Microwave power: 4 mW, Magnetic field: 335.3 ± 5 mT, Modulation width: 100 kHz - 0.2 mT, Sweep time: 4 min, Time constant: 0.3 s, Instrument: JES-FA200.

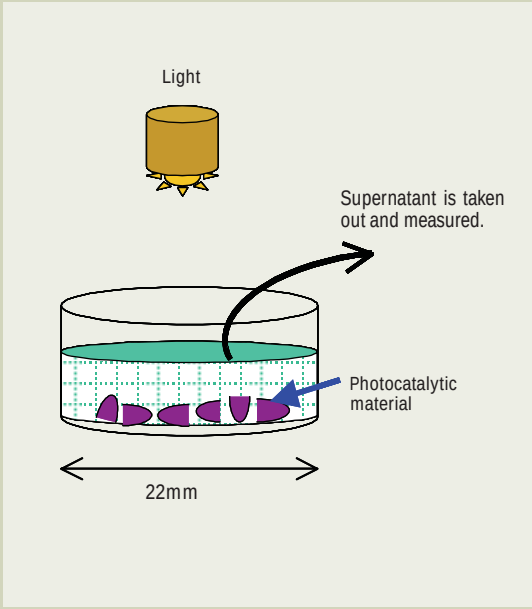

Fig. 5 (a) Immersion method.

Here, we show an example in which a 12-well micro plate is used. Only one well is shown in this figure. A photocatalytic material is cut into pieces to place the material into the well, then a DMPO aqueous solution is added. In the case of this micro plate, a volume of 1 to 1.5 mL is appropriate for this solution. The pieces of sample are irradiated from an UV lamp situated above the sample. After a certain time, the DMPO solution is taken out and measured.

the contact of specific substances to react them and measure the amount of change due to their reaction. They seem to be appropriately used depending on photocatalyst products.

In the MB method (**Fig. 2**), an acrylic cylinder or a polyethylene cylinder is mounted on a test piece, then a MB solution is introduced into the cylinder and the decomposition rate is measured. As a pre-treatment, MB adsorption is conducted for about twelve hours. Next, a new MB test solution is introduced again into the cylinder. Irradiation to the MB test solution is continued for three hours while part of the MB test solution is taken out and its absorbance is measured. From this measurement, the MB residual amount is obtained and the decomposition rate is calculated for determining the activity value of the sample. This method was established by the Japan Association of Photocatalyst Products as a standardized evaluation method [3]. The disadvantage of this method is that a sample shape is limited to a plane.

The NO removal method, which evaluates photocatalytic materials for air purification, is shown in **Fig. 3**. As shown in the figure, a photocatalyst product sample is placed in a chamber that has a light-transmission window on its upper surface and can be sealed. Then, NO gas of 1.0 vol ppm is continuously introduced through the inlet of the chamber at a flow rate of 3 L/min. After thirty minutes of introducing this gas, irradiation is conducted for the sample for five hours. During the irradiation, gas flows out from the outlet of the chamber. The concentrations of NO and nitric dioxide (NO_2) are continuously measured using a chemiluminescence method. From the result, the amount of oxidized NO is obtained and it is determined as the activity value of the product. As a method to evaluate activity of planar materials, this method is defined as one of Japanese Industrial Standards (JIS) [4].

Methods of evaluating photocatalytic activity using ESR

The conventional methods mentioned in the previous section measure reactions where specific substances are decomposed by HO• generated from photocatalysts. Since the photocatalytic activity is based on HO• generated by irradiation, the decomposition activity of materials depends on the HO• generation ability of TiO_2. Accordingly, evaluation of photocatalytic functions by the measurement of HO• production may be a more direct technique. ESR can selectively measure radicals and provide good reproducibility due to its high sensitivity; therefore, it is possible to perform faster and more efficient evaluation than with conventional methods.

However, HO• is highly reactive and its lifetime is very short, so direct measurement of HO• is difficult even with ESR. For this reason, an adduct (DMPO-OH) with a spin-trap reagent 5,5-dimethyl-1-pyrroline-N-oxide (DMPO) is normally generated and HO• measurement is performed. The reaction between DMPO and HO• is very fast; therefore, under the ordinary reaction conditions mentioned in this paper, a sufficient amount for detecting HO• can be captured. Recent technological improvements have enabled the extremely pure DMPO to become commercially available. This has made it possible for ESR to perform highly reliable measurement. In addition, from the ESR instrumental viewpoint, automated tuning and high-sensitivity capability have allowed ESR to offer sufficient functions for routine measurement of photocatalytic

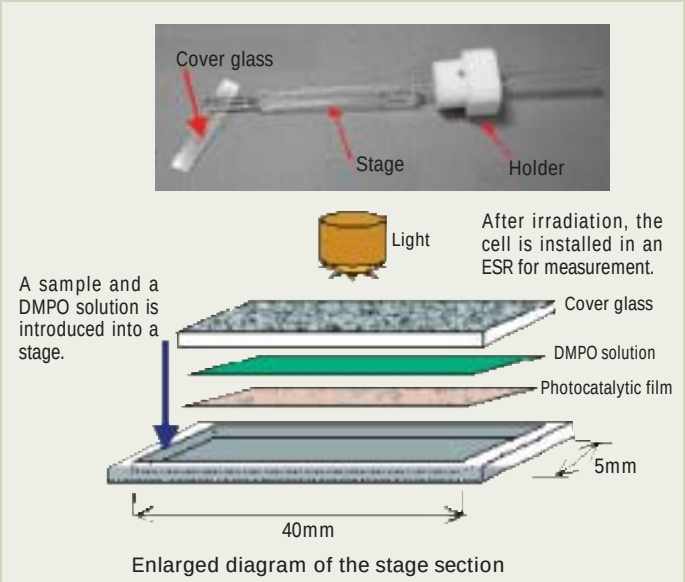

Fig. 5 (b) Tissue cell method.

This method uses a tissue cell, in order to originally measure radicals produced from a thin tissue of animal organs. The tissue cell method is suitable for a sample that floats on a DMPO solution when the immersion method is applied. A sample is cut into a rectangle approximately 4 mm×35 mm squares and placed in a tissue cell in such a way that the coated surface of photocatalyst faces upward. A 60 to 80 µL of DMPO solution is dropped onto the coated film, then the tissue cell is shielded with a cover glass around which coating of silicon grease is applied. Irradiation is started and after a certain time of the irradiation, this cell can be directly inserted into an ESR instrument for measurement.

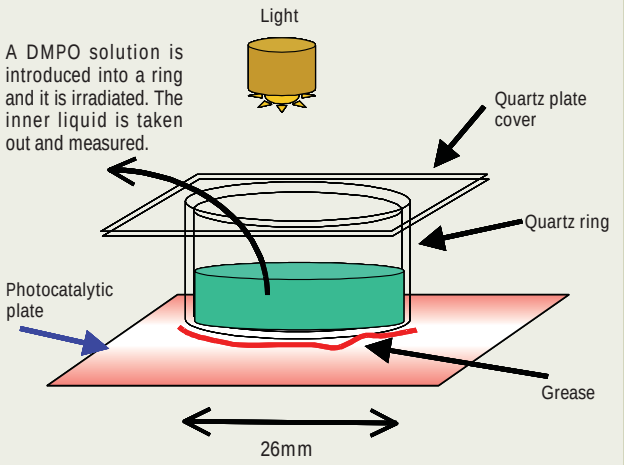

Fig. 5 (c) Ring method.

The principle of this method is similar to the conventional MB method. A cylinder is made of quartz glass (quartz ring), instead of polyethylene for the MB method. An edge of this quartz ring is coated with silicon grease and fixed on the sample surface. A 1 to 1.5 mL of DMPO solution is introduced into the ring and a quartz plate cover is mounted on the ring, then irradiation is conducted for the ring. After a certain time of the irradiation, the inner liquid is taken out and measured.

activity. Supported by these situations, methods of evaluating photocatalysts have been established.

Figure 4 shows the generation reaction of DMPO-OH and its ESR spectrum. Since the adduct shown in Fig. 4 has a long half-life of several tens of minutes, one can easily handle it.

Figures 5 (a) to **(c)** show the measurement systems of photocatalysts using ESR developed until now. All of methods make a sample contact with a DMPO aqueous solution, and measure the DMPO-OH signal intensities after a certain time. In the immersion method (**Fig. 5 (a)**) and the ring method (**Fig. 5 (c)**), a 200 µL of a DMPO aqueous solution is taken out and it is transferred to a dedicated aqueous solution cell for measurement. In the tissue cell method (**Fig. 5 (b)**), a photocatalyst sample is placed in a cell and irradiated, then it is directly measured by ESR. Depending on sample and purpose of measurement, an appropriate system is selected.

The immersion method is a most traditional evaluation method. In this method, a DMPO aqueous solution is introduced into a plate, and a sample is cut if necessary, then it is immersed. This technique can be applied to photocatalyst products with various shapes.

The tissue cell method is suitable for thin-film samples that can be easily cut. Since the cell for ESR measurement is made of synthetic quarts and has high UV transmissivity, it is possible to irradiate a sample through the cell from the light situated above this cell. Also, after a certain time of the irradiation, this cell can be directly inserted into an ESR instrument for measurement.

The ring method is suitable for planar samples. In particular, this technique is most fitted to samples that are difficult to cut, such as hard glass plates and metal plates.

In these three photocatalyst evaluation methods by ESR introduced here, an irradiation time is twenty minutes at longest. Compared to the conventional MB method, in which a sample reacts in an aqueous solution as in these three methods, the three ESR methods can provide extremely fast evaluation of photocatalytic properties, and also are suitable for screening analysis. Thus, the immersion, tissue cell, and ring methods are expected to achieve fast data feedback in the development and improvement of photocatalyst products.

Examples of Evaluation of Photocatalytic Activity Using ESR

Next, we present examples of evaluation of radicals in actual samples, using ESR. Here, samples subjected to evaluation are 1) an air-cleaning sheet that is widely used as an environment-purification product, and 2) a patterning board for micro-printing that is prevailing in the electronics field.

Evaluation of an air-cleaning sheet photocatalyst

A thin film, which holds an extremely small amount of TiO_2 (50 µg/m^2) on a resin film, was evaluated by the tissue cell method (**Fig. 5 (b)**). Three samples from this thin film were subjected to measurement. The two samples (No. 1 and 2) were produced by different techniques and their product performances were known. The third sample (No. 3) was a blank sheet. The respective cells containing the three samples were inserted into the ESR instrument and measured three times: 1) before irradia-

Fig. 6 Comparison of DMPO-OH obtained from photocatalytic film sheets produced by different techniques (together with a blank sheet).

Thee samples were cut from the same sheet and measured, and typical spectra obtained from each sheet were displayed. Three numeric values close to the right side of the three spectra are the mean ± standard deviations and c. v. values of the signal intensities obtained from each sample (the values reflect the ratios of the spectral intensities and the Mn marker intensities simultaneously measured).

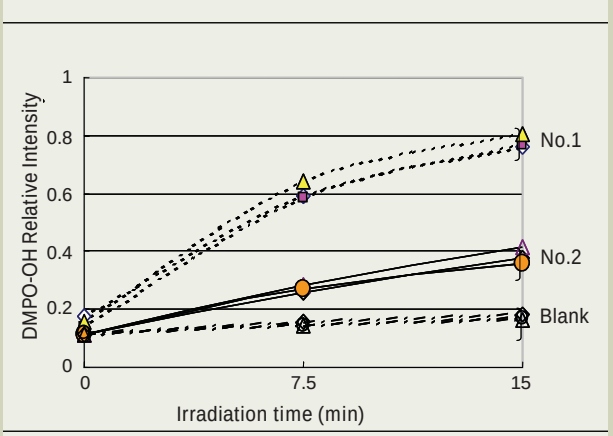

Fig. 7 Time dependency of DMPO-OH generated from each photocatalytic film.

For each sample, the generation of DMPO-OH was confirmed by irradiation. Even for the blank sheet, DMPO-OH was slightly generated. In comparison with the TiO_2 processed samples, an evident difference in relative intensity was recognized.

tion, 2) when the irradiation is temporarily stopped after 7.5 min, 3) when the irradiation is temporarily stopped after 15 min. **Figure 6** shows three ESR spectra for the case 3) (after 15-minute irradiation).

The three samples were cut into three pieces respectively and each piece was measured. Signal intensities of ★ marks and Mn marker signal intensities in the figure were obtained and analyzed. Deviation is c.v. ± 7%, indicating that the $HO^{\bullet}$ generation ability from each sample significantly differs from each other. This result showed a good correlation with the product performance already confirmed, demonstrating that ESR is a highly reliable evaluation method.

Figure 7 shows irradiation-time dependency of the DMPO-OH relative intensity. As is found from **Fig. 7**, the intensity difference between No. 1 and No. 2 is clearly visible from the beginning of the irradiation. From this result, it is demonstrated that ESR can rapidly evaluate an air-cleaning sheet photocatalyst in the prior step of its production, which is one of environment-purification products.

Evaluation of photocatalytic films for micro-printing

When a mold (pattern) that prints 10 µm fine-patterns on an electronic device is created, the decomposition mechanism of a photocatalyst is utilized. The evaluation of photocatalytic films (photocatalyst patterning board) used for creating the patterns [5, 6] was performed using ESR. The samples used for measurement were three types of TiO_2 films (No. 1, No. 2 and No. 3, film thickness of each sample = 100 nm). The TiO_2 dispersion liquid for No. 1 is different from that for No. 2 and No. 3. Whereas, No. 2 differs from No. 3 in a film-formation technique. Because the patterning board of each sample is made of glass, evaluation was performed by the ring method (**Fig. 5 (c)**). In addition, a blank sample that was not deposited by TiO_2 was measured.

Furthermore, as the purpose of comparison, the contact-angle measurement method (**Fig. 8**) was conducted for the four samples (No. 1 to 3, and blank). This method measures the contact angle between a photocatalytic thin film and a drop of water after irradiation, in order to evaluate the decomposition activity in organic substances induced by a photocatalyst. Since these film samples are very thin, when the conventional MB method was used, the amount of MB decomposition was very small and the obtained data was equivalent to the detection limit of the detector. Thus, an evaluation system employing the contact-angle measurement method was established [5, 6]. In this method, a TiO_2 film is coated with hydrophobic organic molecules and a drop of water is placed on this film, then the film is irradiated. TiO_2 is excited by light to generate radicals, decomposing the hydrophobic film. As a result, a drop of water becomes flat, directly contacting with the TiO_2 film. At this time, the contact angle between the film and the water drastically decreases. This decreased angle is used as a value for the photocatalytic activity.

Figure 9 (a) and **(b)** are the results of measurements. **Figure 9 (a)** shows the result obtained by ESR measurement and **(b)** shows the result obtained with the contact-angle measurement method. As is found from these results, in the photocatalytic activity evaluation by ESR, the order of activity was No. 2 > No. 1 > No. 3 and No. 3 showed almost no activity. In contrast, the order obtained by the contact-angle method was No. 2 > No. 1 = No. 3. The performance test data obtained from the final product was No. 2 > No. 1 > No. 3, equivalent to that obtained with ESR. Thus, as shown in Table 1, the product performance agreed well with the evaluation result obtained by ESR, indicating that the ESR method accurately reflects the photocatalytic activity of the photocatalytic thin film.

As presented above, it became clear that, compared to the contact-angle measurement method, the ESR method can perform accurate evaluation of photocatalytic activity. Also, it was demonstrated that, even when a photocatalyst product is in the material stage prior to its production, it could be rapidly evaluated with a high precision using ESR. In particular, the great advantage of ESR is that this method can

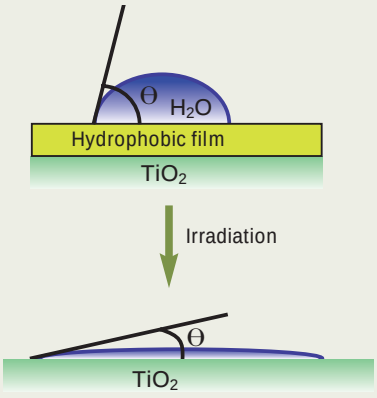

Fig. 8 Method of evaluating the activity of photocatalytic film—Contact-angle measurement method.

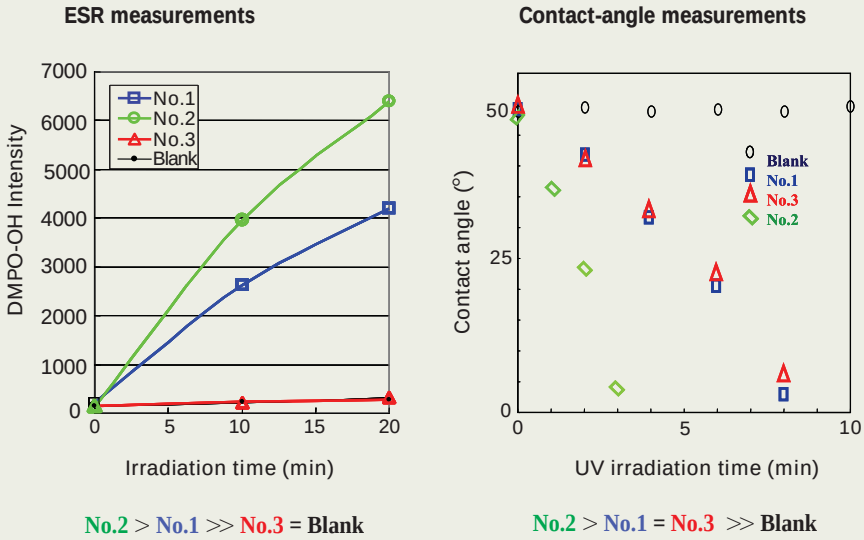

Fig. 9 Comparison of the catalytic activity of photocatalytic films for micro-printing.

Table 1 Comparison of photocatalytic activity obtained by each evaluation method.

Evaluation method	Order of performance (activity strength)
Product performance	No.2 > No.1 >> No.3
ESR method	No.2 > No.1 >> No.3
Contact-angle method	No.2 > No.1 = No.3

The TiO_2 dispersion liquid for No. 1 is different from that for No. 2 and No. 3. Whereas, No. 2 differs from No. 3 in a film-formation technique. In addition, a glass plate not coated with TiO_2 was evaluated simultaneously as a blank sample. These samples were measured by ESR and the contact-angle method, before irradiation and at specified intervals after the irradiation. For the blank film, the generation of DMPO-OH was very small at every measurement, equivalent to the background of reagent. Also, all contact-angle measurements for the blank film showed 50°. In contrast, for the three TiO_2 films, as shown in Table 1, ESR measurements showed great differences in the photocatalytic activity depending on the type of dispersion liquid or film-formation technique.

accurately evaluate samples with low reactivity, for example, very-thin photocatalytic films used in our present experiments. With the conventional MB method, these samples could not be evaluated.

It is known that the photocatalytic activity of photocatalyst products are different depending on their production techniques, even when the raw materials of anatase is used for these products. As recognized in the above experiments, ESR is an effective method since it provides higher accuracy than offered by other conventional methods which cannot distinguish the difference in the photocatalytic activity.

In addition, generally, the conventional methods evaluate the catalytic activity using the decomposition activity of one specific substance; therefore, the activity obtained by these methods holds only for limited substances. However, many contaminants in the water or air are mixtures of various substances. The great advantage of ESR is to directly measure the $HO^{\bullet}$ generation ability which is the origin of oxidizing and decomposing any substances. Thus, ESR is thought to be an efficient measurement method, since ESR can evaluate potential catalytic functions of photocatalysts and provide more reliable catalytic information than other methods.

Conclusion

The TiO_2 catalyst is a technological product developed in Japan, and it is expected to further prevail worldwide. Now, the developments of visible ray responsive photocatalysts [7] and photocatalysts employing metals except for Ti are aggressively implemented. In view of the expansion of the photocatalyst market, in March 2006, Photocatalysis Industry Association of Japan was established in association with many organizations such as the Japan Association of Photocatalyst Products. Also, the establishment of JIS for various photocatalytic evaluation is being under development. It is concluded that photocatalytic-activity evaluation using ESR will become a very useful method for efficient development of new photocatalyst products and for further development of the photocatalyst market.

Note: Patents on the ESR standard for pattern organizers using photocatalyst-containing layers were jointly applied by Dai Nippon Printing and JEOL [8].

Acknowledgement

The author is grateful for K. Ito at Optomaterial Division of Dai Nippon Printing for providing his many measurement data.

References

[1] A. Fujishima, K. Honda and S. Kikuchi.: *Kogyo Kagaku Journal*, **72**, 108 (1969) (in Japanese)
[2] A. Fujishima and K. Honda.: *Nature*, **238**, 37 (1972)
[3] Test method for wet decomposition performance of photocatalyst products, Japanese Association of Photocatalyst Products (2002) (in Japanese)
[4] JIS R1701-1, Fine ceramics (advanced ceramics, advanced technical ceramics) –Test method for air purification performance of photocatalytic materials – Part 1: Removal of nitric oxide.
[5] H. Kobayashi, K. Yamashita and Y. Uno.: *Convertech*, **4**, 106 (2005) (in Japanese)
[6] K. Ito and Y. Nakai.: Abstracts of the 44th annual meeting of the Society of Electron Spin Science and Technology, **2B**, 05 (2005) (in Japanese)
[7] Y. Nosaka and A. Nosaka.: Introduction to Photocatalysts, ed., Tokyo Tosho Co., Ltd., Tokyo, p. 210 (2004) (in Japanese)
[8] Patents pending.

Auger Analysis of Cross Sections Prepared by Cross Section Polisher

Kenichi Tsutsumi
Electron Optics Division, JEOL Ltd.

Introduction

Auger Electron Spectroscopy (AES) provides a high spatial resolution (10 to 20 nm) and can analyze nanometer-level regions from the top surface to a depth of 6 nm; therefore, AES is used for particle analysis and structural analysis of top surfaces of specimens. Also, it is applied to fine structure analysis of cross sectional samples.

However, analysis results of cross sections depend greatly on the quality of the prepared specimens. For example, if distortion or altered layers due to milling exist on a specimen surface, Ar sputtering to remove them is needed before Auger analysis. A long-time Ar sputtering increases the effects of surface roughness and preferential sputtering, making precise cross-sectional structure analysis difficult. Furthermore, to analyze cross-sectional fine structures of a shallow region near the top surface, cross sections are prepared by FIB (Focused Ion Beam). However, FIB is limited to preparing a shallow region of cross sections, a few tens of micrometers in depth from the surface and a few tens of micrometers in width. Thus, cross-section specimens that can be prepared for Auger analysis are limited.

JEOL has developed the Cross Section Polisher (CP). This cross-section specimen preparation device can easily prepare a cross section that has a few hundreds of micrometers in width and can preserve nanometer-level fine structures. CP prepares a cross section in the following way: A high-energy Ar ion beam irradiates the surface of the specimen masked by a shielding plate, from the direction perpendicular to the surface. Thus, the surface region which is not masked by the shielding plate is etched. This device provides two advantages: a) A clean cross section can be obtained, which has less distortion or altered layers due to milling than prepared by conventional mechanical polishing methods, b) A wider-region cross section can be prepared as compared to FIB. Utilizing these advantages, CP has been used as a powerful cross-section preparation tool for SEM, EPMA, and AES.

This paper briefly explains the principle and applications of CP, and focuses on the points which require care in AES, then introduces application examples of cross-section Auger analysis.

Cross Section Preparation by CP

Effectiveness of CP compared to conventional polishing methods

For cross-section preparation, the mechanical polishing method, which cuts a specimen and completes polishing by using grinding wheels and abrasives, is widely used. This method polishes a specimen by utilizing physical contact between the abrasive and the milled surface. Since the portions protruding from an uneven surface are milled selectively, it is easy to prepare some materials (specimens) into flat mirror-surfaces. Furthermore, a wide selection of grinding wheels and abrasives for various specimens allows the control of the milling time and the roughness of the milled surface, and many efficient mechanical polishing devices have been developed. Thus, this is a very effective method. However, mechanical polishing may preserve the affected layers on the polished surface and make it not clear the real interface due to the phenomenon of hard materials being covered with soft materials (called distortion due to polishing). Therefore, the quality of the polished surface largely depends on the skill of the operator, and this point is a disadvantage.

In order for anyone to easily prepare clean cross-section specimens without special skill, CP was developed. The appearance of this device is shown in **Fig. 1**. The main features of CP are as follows.

- CP can prepare a wide range of materials into flat mirror surfaces: a) Soft materials, such as copper, aluminum, gold, solder and polymer, which were difficult to prepare into flat mirror surfaces by conventional mechanical polishing, b) Hard materials, such as ceramics and glasses that are difficult to cut, c) Materials with different hardness levels.
- CP can preserve fine structures of cross sections, such as voids in the bonded interface between gold wires and aluminum pads, which otherwise are crushed by conventional mechanical polishing. This feature also enables one to check how strong the adhesion between plated layers and those of solders are.
- CP can polish wider areas than FIB can.
- Mechanical polishing requires special skill for some materials, but for polishing with CP, an operator can acquire skill in a relatively short time, making it easy to prepare a clean cross section.

For these reasons, CP is very useful for pre-treatment before cross sectional analysis with SEM, EPMA and AES. The next section briefly describes the principle and the method of milling with CP.

Principle of milling with CP

Figure 2 shows the principle of milling with CP. First, as a pre-treatment, a preliminary cross section is prepared by cutting or mechanical polishing in such a way that this section has a trimmed portion necessary for CP milling, having a thickness of 30 to 75 μm. Next, the surface of this section is covered with a shielding plate with the trimmed portion protruding beyond the edge of the shielding plate, and the section is placed on the motor-driven eucentric stage. Then, the milling time is set by a timer and this section is irradiated with a 2 to 6 keV Ar ion beam for preparing the target cross section just beneath the shielding plate.

Figure 3 shows an example of a cross section milled by CP. As shown in the figure, a half-moon shaped cross section is formed. The width and depth of the milled surface depend on the energy of the Ar ions and the irradiating time. In general, the Ar ion energy is determined by the properties of the milled specimen and the Ar ion irradiation area, whereas the irradiating time is determined by the depth and volume of the milled section.

Procedure for cross section preparation

Since the milling process with CP is automated, it is easy to prepare cross sections through unattended operation. However, actually, pre-treatment prior to CP milling is a key point. This requires cutting or polishing, and resin coating to protect the surface of specimen. The procedure for cross-section preparation with CP including the pre-treatment

Principal specifications

Ion accelerating voltage	2 to 6 kV
Ion-beam diameter	500μm (FWHM)
Milling rate	1.3μm/min (at 6kV, Si wafer)
Maximum specimen size	11mm (W)× 10mm (L)× 2mm (H)
Gas	Argon (Ar)
Back pressure	10^{-4} Pa
Evacuation system	Turbo-molecular pump, Rotary pump

Fig. 1 Appearance of the Cross Section Polisher (CP) and its specifications.

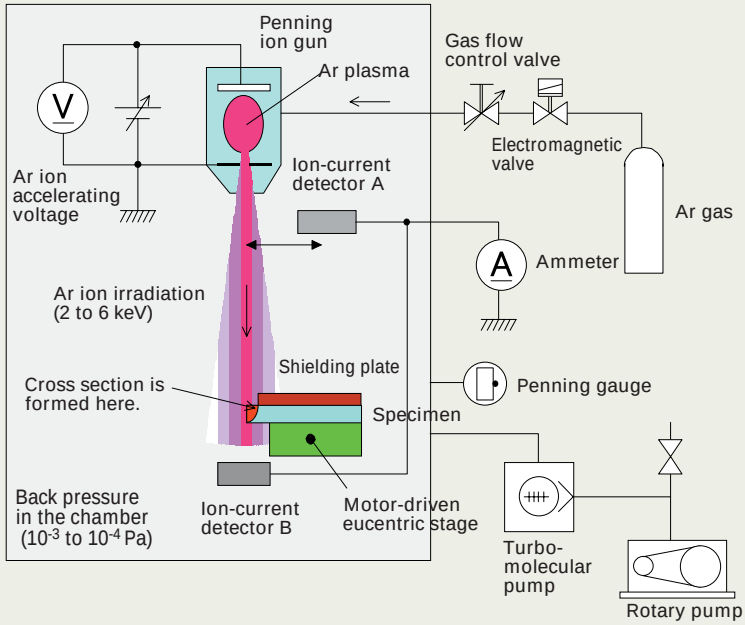

Fig. 2 Principle of milling with CP.

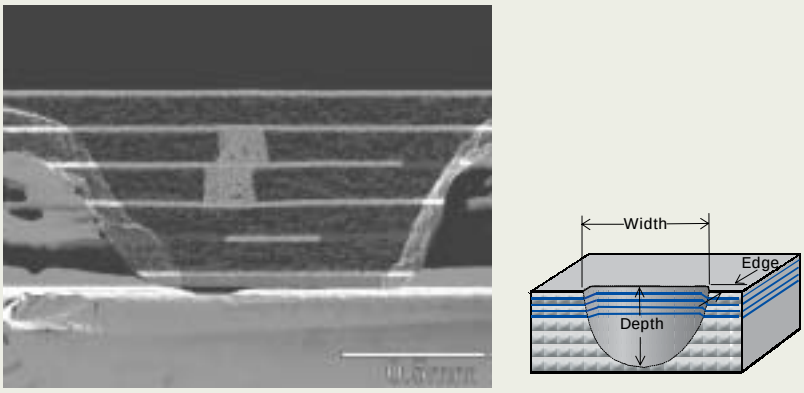

Fig. 3 Example of cross section milled by CP.

before CP milling is as follows (**Fig. 4**).

1) Select a specimen to be milled with CP.

2) Process the specimen until its size becomes appropriate for CP milling.

First, it is necessary to process the specimen to an appropriate size which the CP can accommodate. This size is 11 mm (width) × 10 mm (length) × 2 mm (thickness) or less. To obtain this size, the specimen is adjusted by cutting, slicing or polishing. In this process, it is necessary to protect the surface of the specimen. If necessary, it is better to carry out step 3 – resin-coating the surface – in advance. As mentioned earlier, since a trimmed portion with an edge distance of 30 to 75 μm from the target is needed to be prepared into a cross section, care should also be exercised in this step.

3) Resin coating to protect the surface

Since CP irradiates the specimen surface with Ar ions from the vertical direction, the top surface of the specimen is directly etched, altering its original morphology. Also, as shown in **Fig. 5**, even when the top surface is uneven, etching (milling) goes on over the entire surface with its altered morphology preserved. As a result, vertical streaks due to the unevenness appear on the milled cross section. To reduce these effects, it is necessary to carry out pre-treatment, which coats the specimen surface with resin and hardens it on glass for preparing a flat-surface specimen.

4) Cross sectional milling with CP

When steps 1 to 3 are completed, it is time to automatically prepare a cross section with CP.

Specimens appropriate for CP

Generally, in etching with Ar ions, it should be noted the following two points: a) the etching rate is different depending on the properties of materials (for a material with the same properties, the etching rate is the same), b) even when etching is applied to a material with the same property, if the material has an alloy phase, preferential sputtering arises and a phase different from that in the bulk state appears on the surface, causing surface roughness to occur.

Preferential sputtering is a phenomenon that

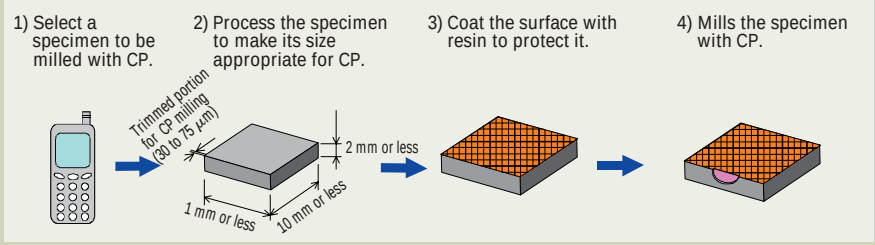

Fig. 4 Procedure for cross-section preparation with CP including the pre-treatment before CP milling.

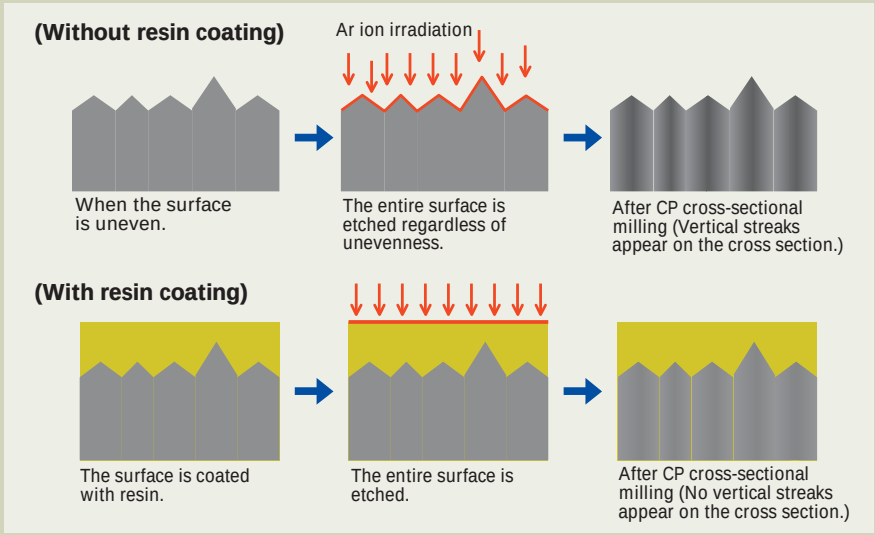

Fig. 5 Difference of milled cross section with and without resin coating.

occurs when Ar ion etching is applied to the surface of an alloy phase comprised of two or more elements. A specific element is preferentially sputtered and the atomic concentration of the surface becomes different from that in the bulk state. For example, for InP, since P is sputtered faster than In due to preferential sputtering, surface roughness occurs and the atomic concentration ratio between In and P of the top surface is different from that in the bulk state [1], [2]. To reduce the effect of preferential sputtering, it was reported that decreasing the incidence angle to the surface is a good solution [3], [4]. In CP, Ar ions irradiate the surface of the cross section in parallel, drastically reducing the preferential sputtering effect even for a material containing various elements, and preparing a flat cross section.

However, in CP, milling to remove a trimmed portion is performed prior to milling for cross-section preparation, as mentioned before. In this process, Ar ions irradiate the specimen surface from the vertical direction. This means that preferential sputtering may arise, degrading the advantage of CP. To perform efficient CP milling, it is necessary to prepare the trimmed portion as small as possible.

For a specimen susceptible to heat, sometimes a long-time CP milling is required since the accelerating voltage and the Ar ion beam current are kept low. Depending on the purpose of the analysis, only cutting or conventional mechanical polishing is applied prior to CP milling for cross-section preparation.

In summary, CP is a useful tool for preparing cross sections; however, some specimens are appropriate for CP milling and some specimens are not. It is necessary to select specimens for cross-section preparation with CP, taking into account the purpose of the analysis, the properties of the material and the milling time.

Auger Analysis of Cross Sections Prepared by CP

AES provides high spatial resolution analysis of the surface of the specimen, with a lateral resolution of 10 to 20 nm and a depth of approximately 6 nm. This feature makes it possible to clearly distinguish nanometer-sized defects and particles in cross-sectional analysis. However, if impurities adhere to a cross section, or if any layer covers another layer on an interface, this phenomenon greatly degrades the accuracy of the high spatial-resolution, surface analysis. To prevent this in cross-sectional Auger analysis, conventionally, a cross section prepared by mechanical polishing was subject to a long-time Ar ion sputtering to remove the impurities from the surface or a distorted layer due to polishing. But as mentioned in the previous section, long-time sputtering induces preferential sputtering, causing surface roughness or changes the chemical composition on the surface.

CP, developed to overcome these problems, reduces distortion due to polishing and enables one to analyze fine structures of an interface, which was difficult to find from the cross section prepared by mechanical polishing. Furthermore, CP allows a clean cross section with few impurities. These advantages imply that CP, as well as FIB, can be utilized as a powerful sampling tool for Auger analysis. In this section, various cross sections prepared by CP are evaluated to discuss whether they are appropriate for Auger analysis, and the results of evaluation are summarized.

Impurities on cross sections milled by CP

We examined to what extent clean cross sections can be obtained using Auger analysis.

First, a Si wafer was cleaved without its surface having been resin-coated, and the cleaved surface was milled by CP. **Figure 6** shows secondary-electron images of the milled cross section and **Fig. 7** shows Auger spectra obtained from six points on it.

In **Fig. 7**, it is found that C, O and Ar are detected at all points 1 to 6. The peak intensities of C and O are very small, suggesting that C and O are impurities adhering to the wafer when it was exposed to the air or during its transfer. These impurities are considered not to be produced by CP milling. For Ar, it is more detected from a region where CP milling is going on (points 5 and 6) than where CP milling has ended (points 1 to 4).

This milled wafer was then subjected to the time variation examination of impurities adhering to the cross section for 18 minutes (**Fig. 8**). In conclusion, from the Auger spectra in **Fig. 8**, it is found that although the wafer was irradiated with a 10 kV, 40 nA electron beam, the peak intensity of C does not increase, and to the contrary, the oxidized Si is reduced, decreasing the peak intensity of O. From this result, the cross section of the cleaved wafer prepared by CP milling is found to be clean. In addition, the Si LVV peak shapes at 0 min and 18 min in **Fig. 8** were compared (**Fig. 9**). It is found that the reduction reaction due to the electron-beam irradiation altered an oxide peak to a metal peak. Using the fact that the intensity of the Si LVV peak at 0 min is half that of the standard Si spectrum, and utilizing the escape depth of Auger electrons, we could estimate that the thickness of the oxide on the cross section milled by CP is 1 to 2 nm from its surface, and approximately 50% of Si is oxidized.

Next, a Si wafer, which was resin-coated to protect its surface, was milled by CP and the amount of impurities on its cross section was examined. The epoxy G-2 (supplied by JEOL DATUM) was used for resin coating. In the experiment, the surface of the Si wafer was thinly coated with G-2 resin and hardened. Following this process, as in the previous experiment, the Si wafer was cleaved and CP milling was conducted for the cleaved surface. **Figure 10** shows secondary electron images of the milled cross section and **Fig. 11** Auger spectra obtained from six points on it.

In **Fig. 11**, it is found that C, O and Ar are detected at all points 1 to 6, as in **Fig. 7** (without G-2 resin coating). The peak intensities of C and O are very small, suggesting that C and O are impurities adhering to the wafer when it was exposed to the air or during its transfer. These impurities are considered not to be contaminants caused by G-2 resin. For Ar, as well as in **Fig. 7**, it is more detected from a region where CP milling is going on (points 5 and 6) than where CP milling has ended (points 1 to 4).

This milled wafer was then subjected to the

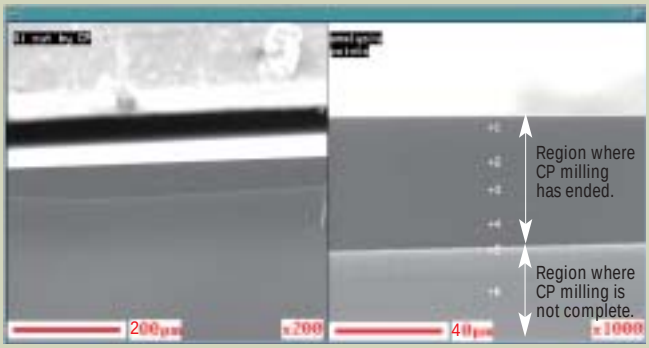

Fig. 6 Cross section of a Si wafer milled by CP without resin coating (irradiation conditions: 10 kV, 40 nA).

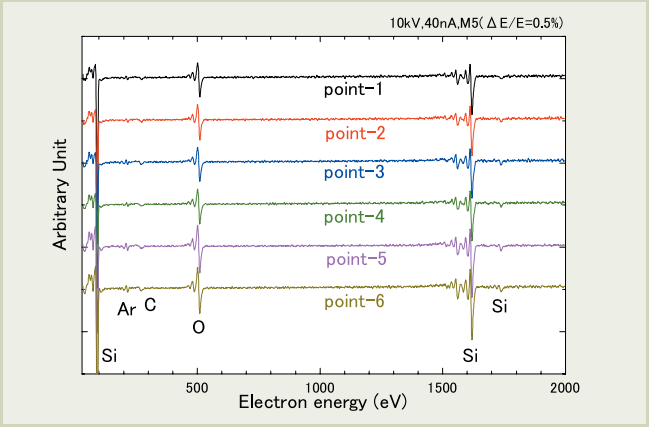

Fig. 7 Auger spectra obtained from the cross section milled by CP without resin coating.

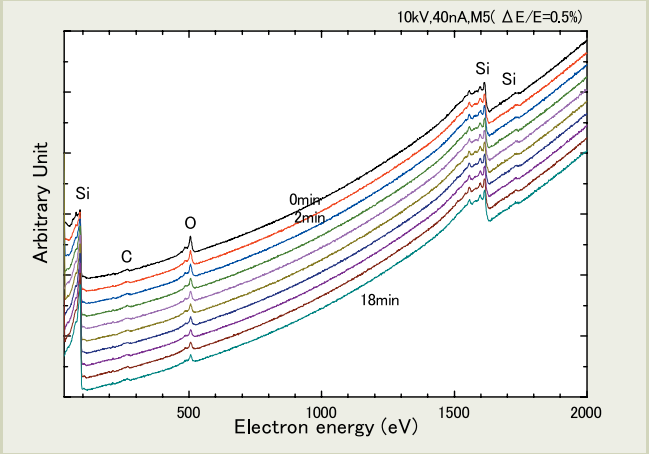

Fig. 8 Time variation of Auger spectra for 18 min electron-beam irradiation, obtained from the cross section milled by CP without resin coating (irradiation conditions: 10 kV, 40 nA, spectra acquisition at 2 min-intervals).

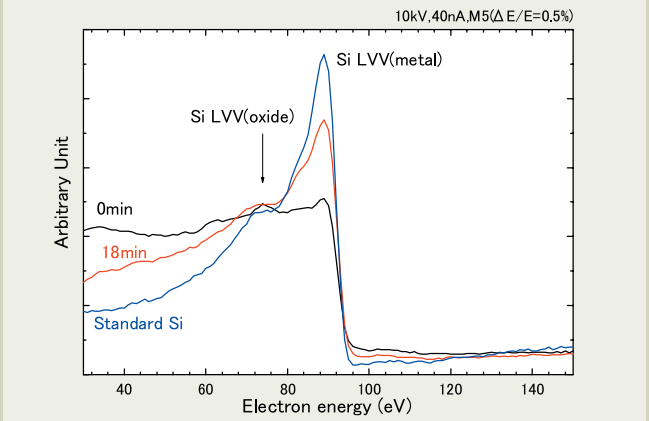

Fig. 9 Change of shape of Si LVV peaks caused by the reduction reaction due to the electron-beam irradiation (at 0 min and 18 min).

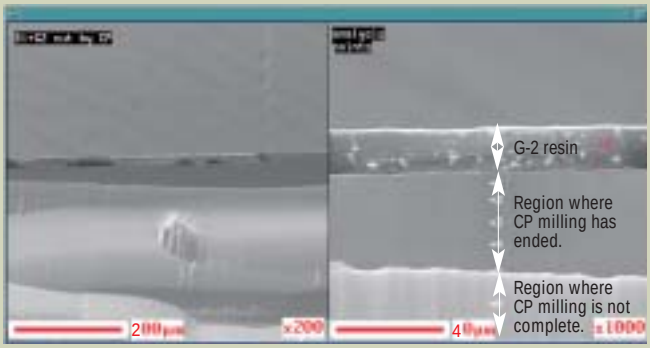

Fig. 10 Cross section of a Si wafer milled by CP with G-2 resin coating (irradiation conditions: 10 kV, 40 nA).

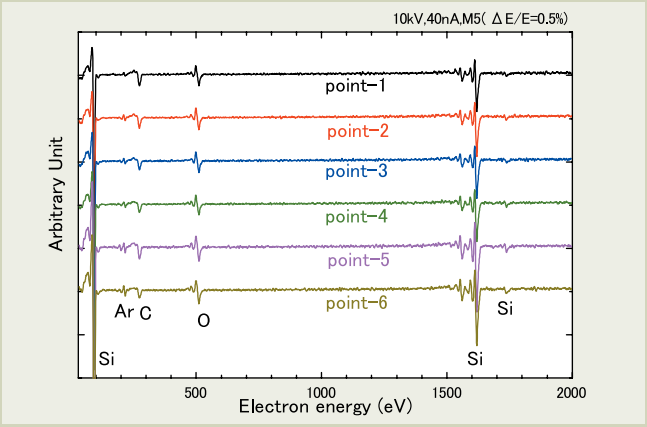

Fig. 11 Auger spectra obtained from the cross section milled by CP with G-2 resin coating.

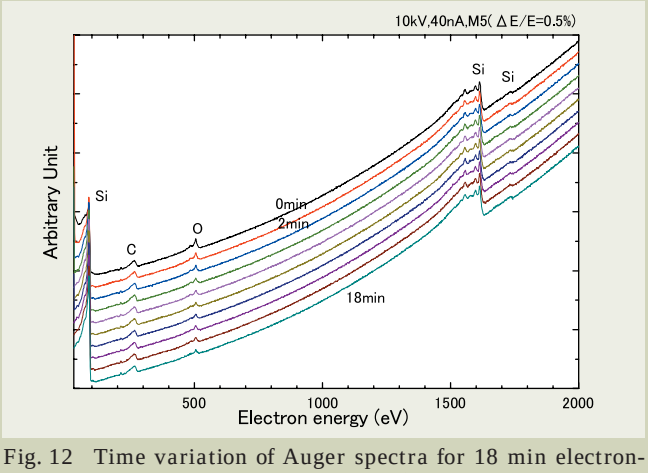

Fig. 12 Time variation of Auger spectra for 18 min electron-beam irradiation, obtained from the cross section milled by CP with G-2 resin coating (irradiation conditions: 10 kV, 40 nA, spectra acquisition at 2 min-intervals).

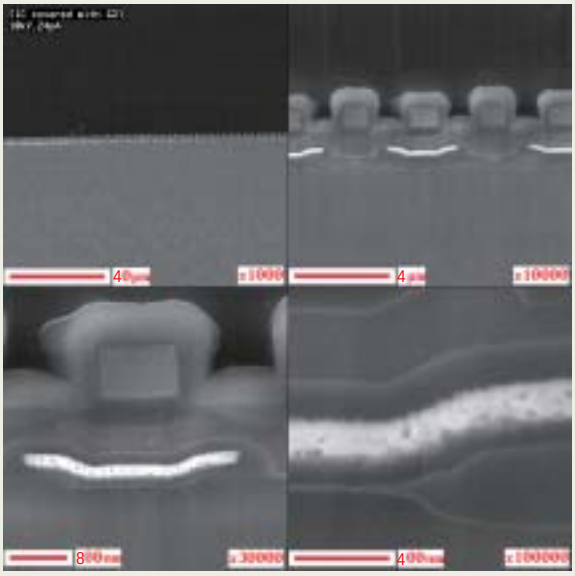

(a) Cross section prepared by CP with G-2 resin coating

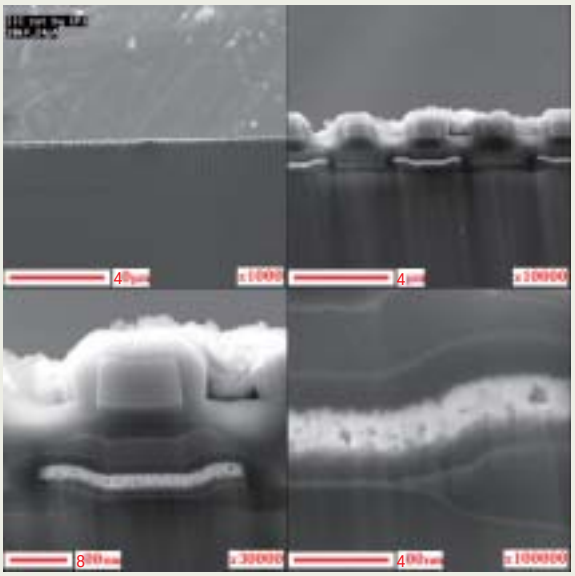

(b) Cross section prepared by CP without G-2 resin coating

Fig. 13 Comparison of SEM images of cross sections prepared by CP with and without resin coating (specimen: IC, irradiation conditions: 10 kV, 24 pA).

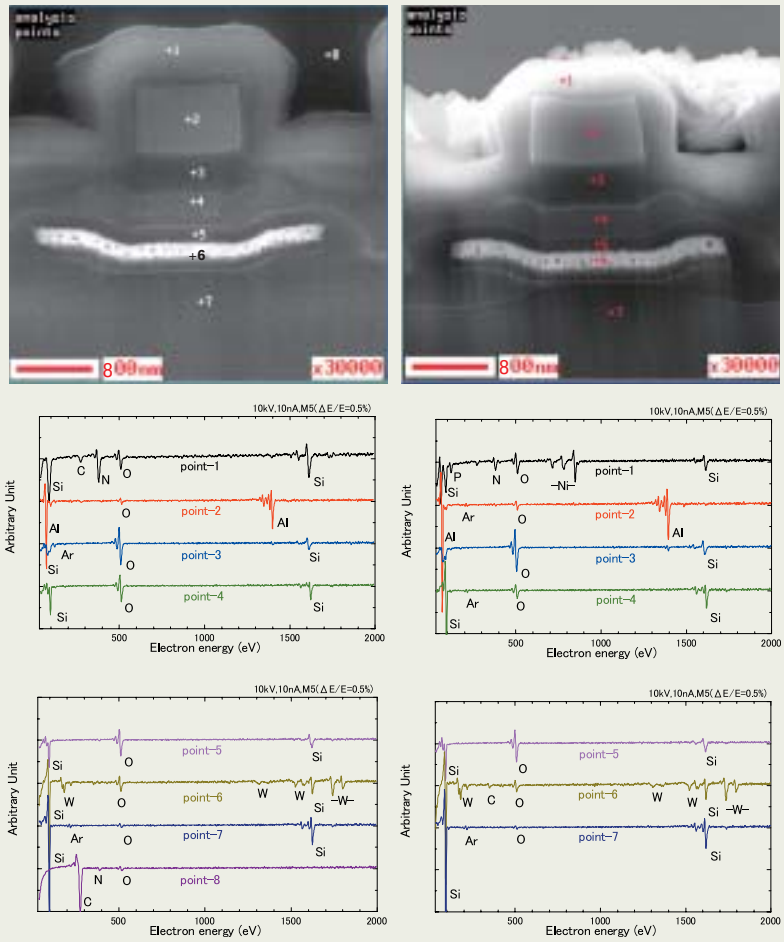

(a) With G-2 resin coating (b) Without G-2 resin coating

Fig. 14 Comparison of Auger spectra with and without resin coating.

time variation examination of impurities adhering to the cross section for 18 minutes (**Fig. 12**). As in the previous experiment, from the Auger spectra in **Fig. 12**, it is found that although the wafer was irradiated with a 10 kV, 40 nA electron beam, the peak intensity of C does not increase, and to the contrary, the oxidized Si is reduced, decreasing the peak intensity of O. From this result, it is found that although G-2 resin was used to protect the surface, it generated impurities and the use of the resin is suitable in samples for Auger analysis.

Differences of cross sections milled by CP with and without resin coating

In the last section, we demonstrated that even when G-2 resin coating is applied to the surface of specimen, a clean cross section is prepared by CP milling without impurities adhering to its surface, causing almost no problem for Auger analysis. However, in Auger analysis, it is necessary to eliminate the possibility of contaminating the surface as much as possible, and to pursue the analysis of the specimen surface with its native state preserved. Two specimens with and without G-2 resin coating their surfaces were prepared, and they were milled by CP, then subjected to Auger analysis.

Figure 13 compares SEM images of cross sectional specimens of an IC having an unevenness of approximately 1 μm, with and without G-2 resin coating. It is found that fine structures can be observed for both specimens at a magnification of $\times$100,000, implying that clean cross sections were prepared from both specimens. However, on the cross section without G-2 resin coating, vertical streaks left by the beam due to the unevenness of the top surface remain. In addition, when the top surfaces of the two specimens are viewed from the direction of the cross section, it is found that for the specimen without G-2 resin coating, CP milling somewhat altered the morphology of its top surface; to the contrary, for the specimen with G-2 resin coating, its top surface is protected with the morphology preserved.

Next, **Fig. 14** compares Auger spectra of the two specimens. The Auger spectra were obtained from seven to eight points. Almost no difference is seen at points 2 to 7 on both specimens; however, at point 1 on the Si_3N_4 layer of the top surface, the detected elements are greatly different. This is due to the fact that when CP milling is conducted without resin coating, since there is a gap between the shielding plate and the specimen, Ni and P that are the constituent elements of the shielding plate are implanted in the layer of the top surface, induced by Ar etching by CP. It is concluded that when preparing cross sections by CP milling without resin coating, Ar etching influences the top surface and may change its morphology and chemical composition; therefore, care should be exercised.

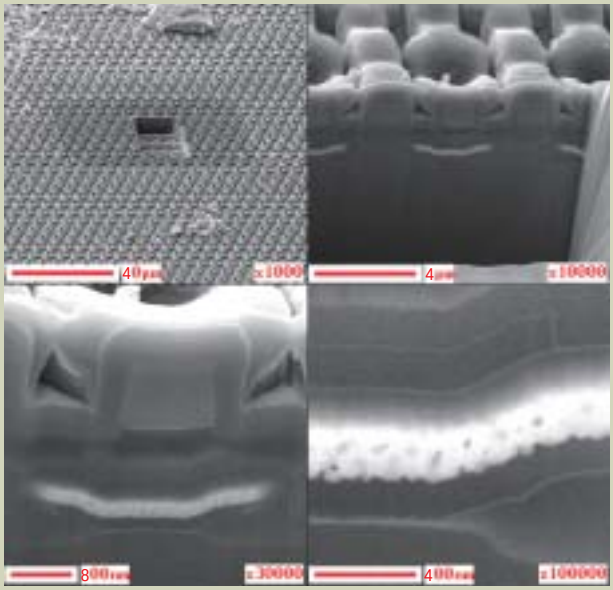

Fig. 15 SEM images of a cross section of an IC prepared by FIB (specimen: IC, irradiation conditions: 10 kV, 24 pA).

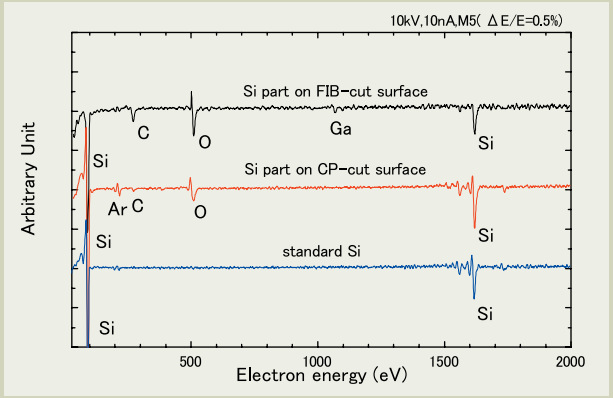

Fig. 16 Comparison of Auger spectra of Si parts on cross sections milled by FIB and CP (specimen: IC, irradiation conditions: 10 kV, 10 nA).

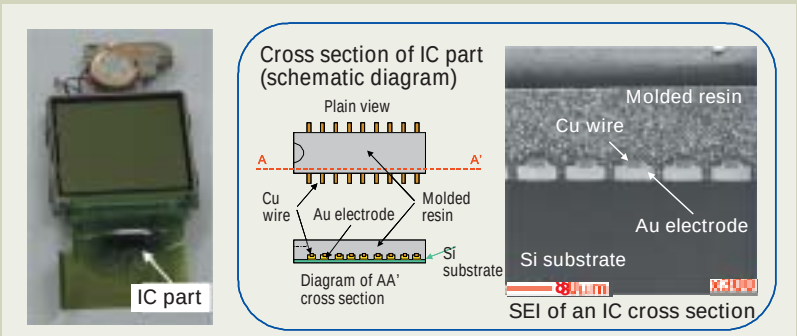

Fig. 17 Photograph of the IC part of the same type used for the experiment and the schematic diagram of the portion of the cross section prepared by CP.

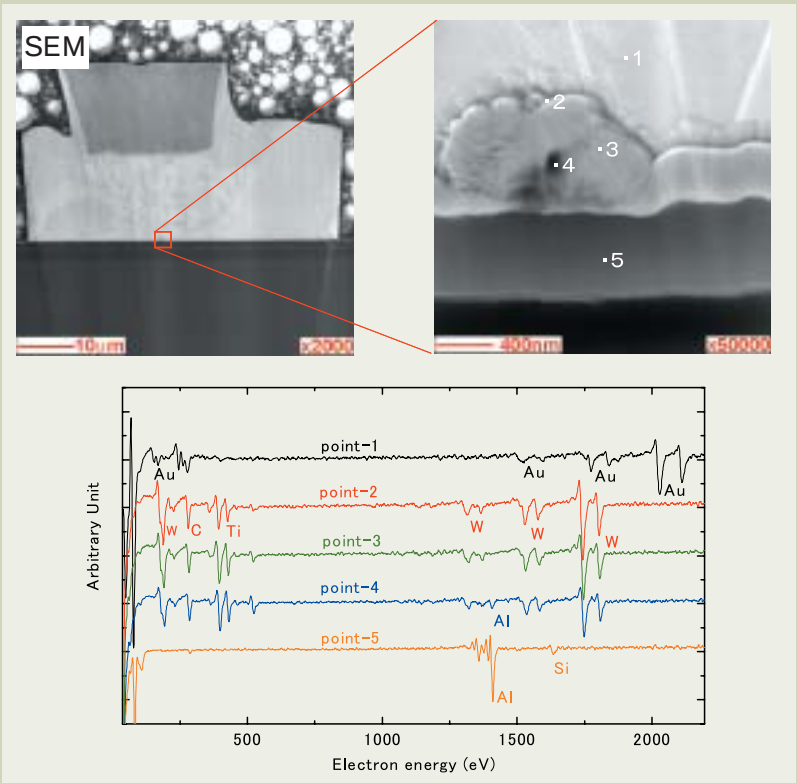

Fig. 18 Auger analysis of a defect part on the interface between the Si substrate and an Au electrode (irradiation conditions: 10 kV, 10 nA).

Problem of charging of resin on the specimen

The effect of charging when G-2 resin is used is discussed. Since AES analyzes the top surface of the specimen, even when a specimen that causes charging is used, it cannot be coated with a conductive thin film, unlike in the analysis using SEM-EDS or EPMA. Thus, when the specimen contains an insulating material, this portion is covered with an aluminum foil or an indium sheet so that it is not irradiated with the electron beam as much as possible. However, when CP milling is applied, since the top surface of the specimen is frequently resin-coated before cross-section preparation by CP, whether G-2 resin is charged or not is a crucial problem that influences the results of Auger analysis.

In principle, G-2 resin becomes charged because it is insulating material. In fact, various factors, such as the state and chemical composition of the specimen, and the thickness and the extent of adhesion of resin coating, seem to determine whether the resin is charged or not. For example, in **Fig. 14 (a)**, the Auger spectrum obtained from point 8 (on G-2 resin) is not disturbed by resin coating, revealing the constituent elements to be C, N and O. On the other hand, in **Fig. 10**, the secondary-electron image of the Si wafer elucidates that the same G-2 resin was charged greatly. Thus, depending on the specimen, G-2 resin is sometimes charged and sometimes not. The reason for it is not known. In actual experiments, even when the G-2 resin part on the specimen surface is charged, a charge-neutralizing gun irradiates the surface with Ar ions, suppressing the effect of charging. Thus, Auger analysis can be performed regardless of specimen charging.

Differences of cross sections prepared by FIB and by CP

Conventionally, when a specimen has a fine structure 1 μm or less in size, FIB was used to prepare a cross section containing this structure before Auger analysis. CP which was developed by JEOL can preserve a clean, fine cross-sectional structure. We considered differences of cross sections prepared by FIB and by CP for Auger analysis.

First, the differences are considered in terms of SEM image. **Figure 15** shows SEM images of a cross section of an IC prepared by FIB. This IC is the same as those used in the previous sections (in **Figs. 13** and **14**). These images were taken with the same magnification (× 100,000) as that in **Figs. 13**; however, the SEM images in **Figs. 13** and **14** are slightly different due to the cross section tilt in SEM vs. FIB. From these images, it is found that both FIB and CP can prepare high-quality cross sections, which provide good sharpness and contrast in SEM images.

Next, the differences of two cross sections prepared by FIB and by CP are considered in terms of Auger spectrum. **Figure 16** compares three Auger spectra of Si. The top and middle

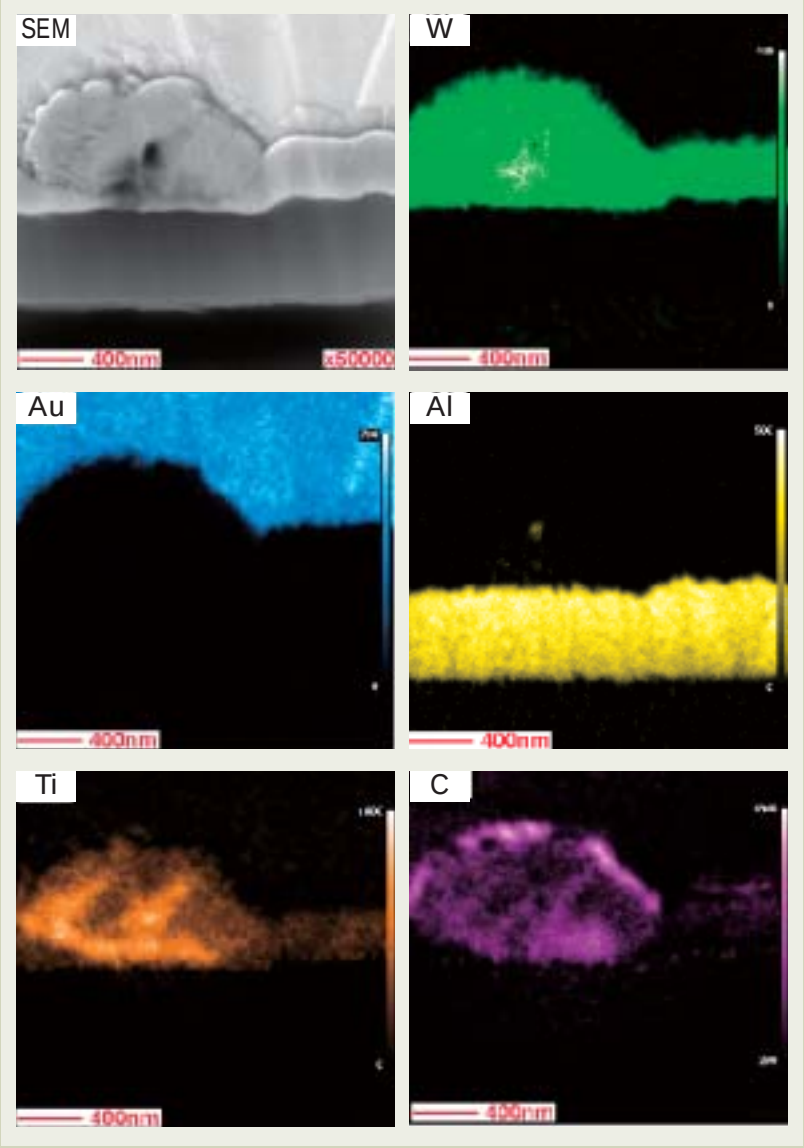

Fig. 19 Auger mapping result of the defect part on the interface between the Si substrate and an Au electrode (irradiation conditions: 10 kV, 10 nA, magnification: × 50,000).

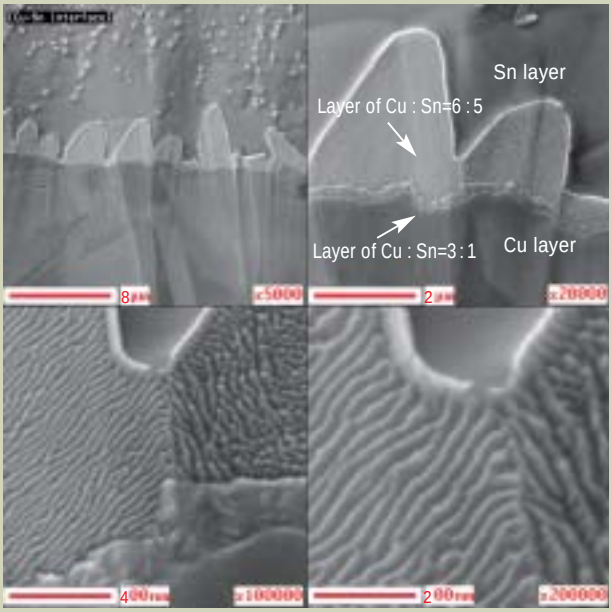

Fig. 20 SEM images of the bonded interface of Cu and Sn (Ar etching was performed after CP cross-section preparation) (irradiation conditions: 10 kV, 24 pA).

spectra were obtained from the Si parts of both cross sections, immediately after FIB and CP milling. The bottom spectrum is the standard Si spectrum. Ga was detected from the cross section milled by FIB and Ar by CP. Both elements seem to be mixed into the cross sections during the etching. The other detected elements, C, O and Si are the same for the two cross sections. However, the peak intensities of C and O obtained from the FIB-milled cross section are higher than those from the CP-milled section. In addition, the Si spectrum from the FIB-milled section has a shape of combined spectra of pure Si and oxidized Si. These facts indicate that when FIB is used to prepare a cross section, carbon impurities are easier to adhere to the cross section and it is more susceptible to oxidization than when CP is used.

C and O adhered to both cross sections prepared by FIB and by CP when the cross sections were exposed to the air for approximately five minutes during their transfer. The adsorption speed and reaction speed of C and O are slower on the CP-milled section than on the FIB-milled section. The difference of the speeds may be due to the presence of altered layers or Ga inclusions, but a clear reason is not known. Study will have to be conducted in the near future. In actual Auger experiments, however, the cross section is subjected to surface cleaning with Ar ions before FIB or CP milling. Thus, Auger analysis can be performed on such samples without introducing artifacts.

As mentioned above, we found that high-quality cross sections for Auger analysis can be prepared by both FIB and CP. FIB prepares a cross section with an accuracy of a few tens of nanometers while controlling a region a few tens of micrometers in width. On the other hand, since CP uses an optical microscope to align the target portion to be prepared, it mills a region a few hundreds of micrometers in width, with an accuracy of approximately 10 micrometers. Thus, the accuracies of the portions milled by FIB and CP are significantly different. We may conclude that, for Auger analysis, the appropriate tool for cross-section preparation depends on the state or the size of the target specimen.

Application Examples of Auger Analysis of Cross Sections Prepared by CP

We demonstrated that CP is very useful for Auger analysis of cross sections. In this section, two application examples of Auger analysis of cross sections prepared by CP are presented.

Auger analysis of a cross section containing insulating material (a wire junction in an IC part)

In an Auger experiment of a cross-sectional specimen containing insulating material, a

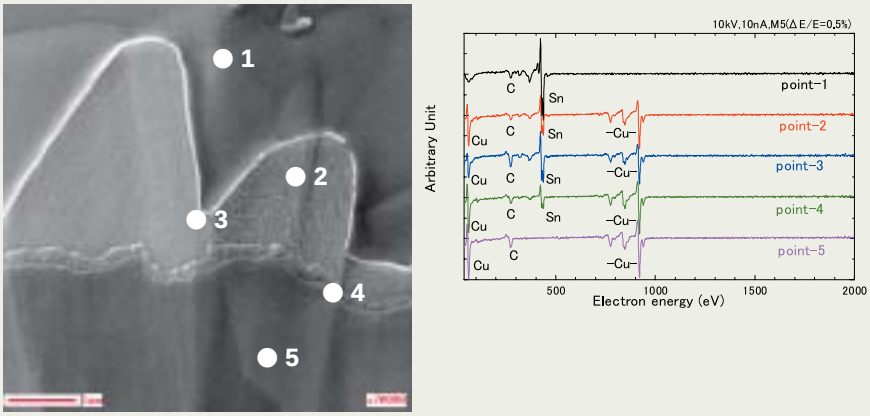

Fig. 21 Auger analysis result of the interface between Cu and Sn (irradiation conditions: 10 kV, 10 nA).

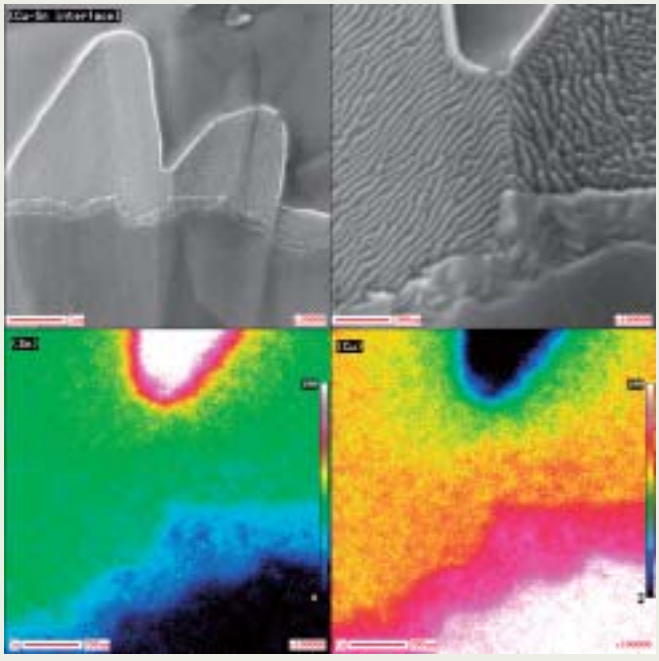

Fig. 22 Auger mapping result of the interface between Cu and Sn (irradiation conditions: 10 kV, 10 nA, magnification: ×100,000).

cross section was prepared from a molded IC part that controls a liquid-crystal display of a cellular phone. **Figure 17** shows the photograph of the IC part of the same type used for the experiment and the schematic diagram of the portion of the cross section prepared by CP (together with a secondary-electron image of an IC cross section). CP can prepare the cross section with the native state of the molded IC preserved while not peeling off the molded resin. In this experiment, an interface between the Si substrate and an Au electrode was subjected to cross-sectional Auger analysis.

Figure 18 shows the result of Auger analysis. It is found that high-intensity W and Ti are detected from a defect part, whereas Al is detected at a central black point (point 4) in the defect part. **Figure 19** shows the result of Auger mapping of the defect part for C, Al, Ti, W and Au, respectively. This mapping was conducted over the field of view with a magnification of ×50,000. Although the black point is very small, approximately 100 nm in size, high spatial resolution provided by Auger analysis enables micro-defects to be clearly distinguished.

Cross-sectional Auger analysis of a bonded interface of soft material (a bonded interface of Sn and Cu)

In an Auger experiment of a bonded interface of soft materials, the bonded interface of Sn and Cu was subjected to cross-sectional Auger analysis. It is known that on this interface, two thin layers of different atomic concentrations, which are Cu:Sn = 3:1 and 6:5, respectively, are formed. If the quality of the prepared cross section is low, it is difficult to observe the fine structures of these layers. To prepare a high-quality cross section, CP milling was conducted for the layers and they were subjected to cross-sectional Auger analysis.

The procedure of this Auger analysis is as follows: Sn was placed on a heated Cu substrate and Sn reacted with Cu, then natural cooling was applied to this specimen. After the specimen was cooled, it was subjected to CP milling for cross-section preparation. Ar ion sputtering was performed for the prepared cross section in an ultrahigh vacuum. Then, C and O were removed from this section to make its surface clean. Finally, Auger analysis was conducted for it.

Figure 20 shows SEM images of the bonded interface of Cu and Sn. It is found that, from the bottom to the top of the specimen, four different layers are formed in the following order: a Cu layer, a layer of Cu:Sn = 3:1, a layer of Cu:Sn = 6:5, and a Sn layer. However, another layer appears to form on the interface between the layer of Cu:Sn = 6:5 and the Sn layer. For more study, Auger spectra were obtained from this interface. The result of the Auger measurement is shown in **Fig. 21**.

When the Auger spectra of points 2 and 3 are compared, the peak intensity of Cu at point 3 is higher than that at point 2, whereas the intensity of Sn is lower at point 3 than at point 2. To understand this phenomenon, Auger mapping was conducted for Cu and Sn. This result is shown in **Fig. 22**. The Auger maps indicate that another layer exists between the layer of Cu:Sn = 6:5 and the Sn layer.

Conclusion

Since Auger analysis provides a high resolution and can analyze nanometer-level regions from the top surface to a depth of 6 nm, it is applied to fine structure analysis of cross sections, as well as to top surface analysis. The method of preparing cross sections is very important because the results of cross-sectional Auger analysis depend greatly on the quality of the prepared cross sections. Using the Cross Section Polisher (CP) developed by JEOL, we evaluated whether cross sections prepared by the CP can be used for Auger analysis.

The following results were found: a) CP can prepare high-quality cross sections that preserve fine structures, as FIB can, b) The surface of the cross section prepared by CP is sufficiently clean for Auger analysis, c) This clean cross section can be prepared over a wide region of a few hundreds of micrometers in width.

This powerful cross-section preparation tool, CP, will be applied to various analytical fields, as it complements the size of the cross sections prepared by conventional mechanical polishing and by FIB (The cross sections prepared by CP are smaller than those prepared with mechanical polishing and wider than with FIB).

References

[1] T. Hagiwara, K. Yoshida and S. Tanuma.: Surface Analysis Society of Japan, Summary of Practical Surface Analysis Seminar, **72** (1997)

[2] T. Hagiwara, K. Yoshida and S. Tanuma.: *J. Surface Analysis* **3** (1997) 646.

[3] J. B. Malherbe.: *Applied Surface Science* **70/71** (1993) 322.

[4] J. Zemek, O. A. Baschenko, M. A. Tyzykhov and P. Jiricek.: *Surface Science* **318** (1994) 421.

Development of a New Environmental Scanning Probe Microscope : JSPM-5400

Hideo Kojima, Keiichi Nakamoto, Yoshihiro Imashige, Hiroshi Tajima, Yoshihiro Takeda and Shinich Kitamura

Electron Optics Division, JEOL Ltd.

Introduction

The Scanning Probe Microscope (SPM), including the Atomic Force Microscope (AFM) and the Scanning Tunneling Microscope (STM), is widely used as a powerful tool to measure a topographic shape of a sample with nanometer-scale resolution.

Recently, applications of the SPM to study of material properties have been increasing. The reason for this is that in addition to the original topographic-measurement capability, the SPM has provided increasingly versatile capabilities, such as visco-elasticity atomic-force microscopy (VE-AFM), lateral-modulation friction force microscopy (LM-FFM) and scanning Kelvin probe microscopy (SKPM), which enable one to obtain mechanical or electrical properties of the sample with its topography.

Most of the modern SPM instruments are used at ordinary temperatures and pressure. There are, however, strong demands to use SPM in actual environments, such as at low or high temperatures, in controlled atmospheres and in vacuum, in which observed samples are practically used as industrial products. This situation has necessitated the development of a SPM in which sample environments can flexibly be controlled.

To satisfy the demand, JEOL has developed a new environmental SPM: the JSPM-5400. This innovative SPM is aimed at achieving multi-functional measurements and flexible sample environment control as well as providing high-resolution imaging.

Features of JSPM-5400

Figure 1 shows the external appearance of the JSPM-5400. The JSPM-5400 has been developed on the basis of the following three main concepts.

High-resolution imaging without damage using Non-contact AFM (NC-AFM)

Usually, the AFM has been used with amplitude detection. As for this detection method, the cantilever is scanned with intermittent contact on the sample surface. Therefore, there is always a possibility for the cantilever to damage it, especially when the soft sample is measured.

JEOL SPMs are equipped with a Non-contact AFM (NC-AFM) that employs a constant excitation amplitude FM (frequency modulation) detection method (JEOL patent). The main feature of the NC-AFM is to provide a high-resolution topographic image without contact between the apex of the cantilever and the sample surface. The sensitivity of this FM detection has further been improved due to the employment of a digital PLL (Phase-Locked Loop) for a new amplifier, which enables high-stability imaging with atomic-level resolution. This robust capability is demonstrated in a topographic image of mica obtained with the NC-AFM (**Fig.2**). Because an auto gain control (AGC) circuit is incorporated in the new amplifier with a constant amplitude mode, the JSPM-5400 enables us to observe a dissipation image of a sample, which displays energy dissipation in the sample.

Figure 3 is an example of NC-AFM, which shows the surface of a DVD-RAM under vacuum in the NC mode of SKPM. **Fig. 3 (a)** and **(b)** respectively show a topographic image of the DVD-RAM and a surface-potential image in the same area as that in (a). Differences in surface potential clearly reveal the writing state of the DVD.

Because we can obtain a surface-potential image with NC-AFM under the restriction of charge transfer between the probe and the sample, we can state that NC-AFM is a very useful technique. Furthermore, under a vacuum environment, a vibration peak of resonant cantilever becomes sharper so that better frequency resolution can be obtained in the FM detection method.

Environmental control for versatile imaging

To achieve versatile imaging under diverse sample environments controlled by the JSPM-5400, drastic improvements of capabilities and extension of optional accessories have been made.

●Flexible environmental control

The vacuum quality has increased due to the

Fig. 1 External appearance of a new environmental SPM, the JSPM-5400.

improvement of the structure of the SPM head and the employment of an optional cold trap system. By the use of the cold trap system, the vacuum pressure around the sample reaches down to 8.5×10^{-6} Pa, when the pressure is approximately 2.0×10^{-5} Pa with ordinary pumping. Thus, gas adsorption on the sample can be reduced to a minimum, maintaining a clean sample surface. Because optical-axis alignments of the laser and photo detector are designed to be performed from the outside of the vacuum, the JSPM-5400 provides optimal imaging for any cantilever.

●Extension of optional accessories

The JSPM-5400 can be equipped with extended optional accessories for multi-purpose, multi-functional measurements, including heating/cooling holders, a temperature controller for stable observation of heated/cooled samples and an airlock sample exchanger that enables a sample to be changed while maintaining the vacuum.

New technologies for safety and easy operation

The JSPM-5400 has served extended new functions, such as shortening measurement and approach time, and preventing collision between the sample and the cantilever.

●Safety high-speed approach

In a conventional SPM, the cantilever approaches the sample at a constant speed and stops at a specified position (**Fig. 4(b)**). Thus, when the distance between the cantilever and the sample is far, approaching requires a long time.

To shorten the approach time, the JSPM-5400 uses a two-step, safety high-speed approach: high-speed approach and fine approach (**Fig.4 (a)**). The former detects weak attractive force from a far field, whereas the latter detects the distance between the cantilever and the sample while finely controlling the sample position; therefore, the cantilever can approach the sample in a shorter time. **Figure 5** shows a comparison of the approach time with the conventional constant-speed approach and with that with the safety high-speed approach, indicating that the safety high-

Fig. 2 NC-AFM topographic image of mica.
(scan size : 10 nm × 10 nm)

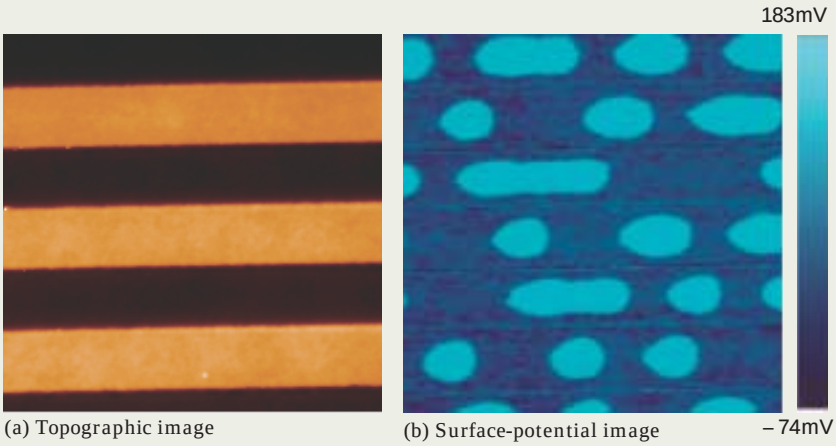

Fig. 3 Surface imaging of a DVD-RAM obtained with SKPM
(scan size : 3.5 μm × 3.5 μm).

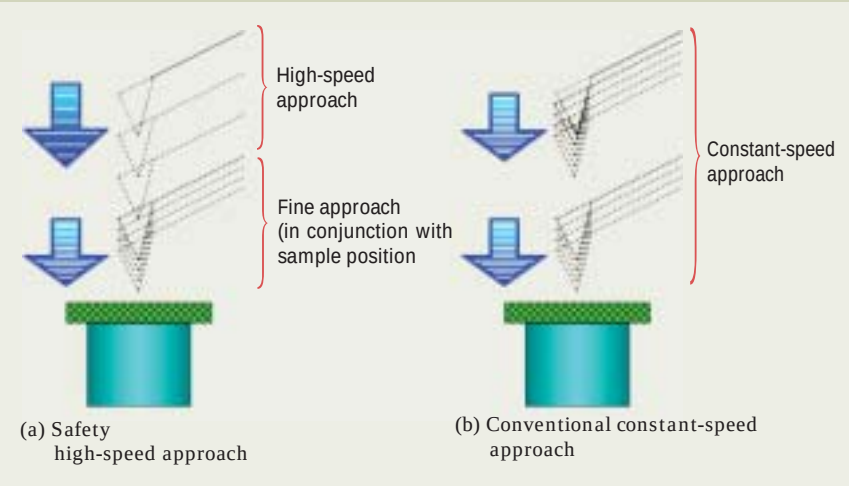

Fig. 4 Schematic diagram of safety high-speed approach and conventional constant-speed approach.

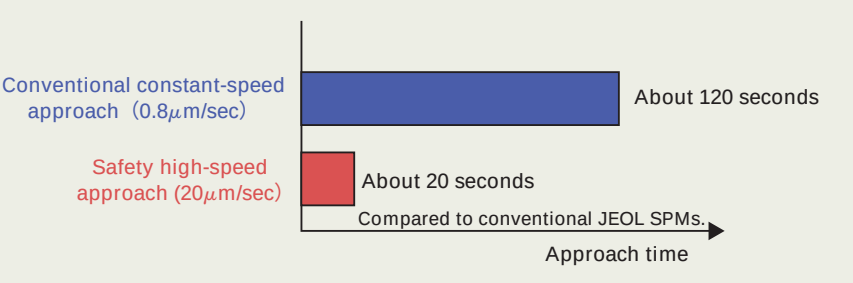

Fig. 5 Time required for approaching sample when the distance between the cantilever and sample is 100 μm.

speed approach shortens the approach time by about one sixth compared to the conventional constant-speed approach.

The safety high-speed approach is effective for highly light scattering samples and transparent samples, which are difficult to know the actual distance between their surfaces and the cantilever.

●Damage-less scan control

Damage-less scan control is used to operate the probe within a limited area (distance L in **Fig. 6**) with respect to a reference height (point A in **Fig.6**). In the observation of the edge of cross sections, which is difficult for the conventional SPM, the probe can be safely scanned without collision of the apex of the cantilever with the edge. In addition, the damage-less scan control incorporates a reference-height automatic renewing function. This function automatically renews the reference height in the upper direction of a concave portion even for a sample with steep concavity (patent applied for). Thus, the JSPM-5400 can measure samples with unknown topographic shapes, without damage.

Figure 7 shows a topographic image of a multi-layer optical film using the damage-less scan control. The layer structures of the multi-layer optical film can be observed successfully even around the edge.

●Fast and simple positioning

A sample of a polymer mixture tends to have components with different diameters, causing steep unevenness of the surface of the sample. This may lead to the situation that the cantilever collides with the sample surface and fast observation to obtain its entire image is difficult.

Combined use of the skip-scan function and damage-less scan control incorporated in the JSPM-5400 enables us to rapidly observe the entire image of the sample having an unknown topographic shape, without the collision between the cantilever and the sample. **Figure 8** shows a topographic images of glue made of a polymer mixture, obtained by a combination of the skip-scan and the damage-less scan control. In addition, use of a zoom function for the field of interest, which allows us to arbitrarily specify the ratio of horizontal and vertical sizes and rotations, can dramatically shorten useless scan time.

●Probe auto tracking

This function automatically corrects the vertical drift caused by thermal expansion or contraction of the sample during observation with heating or cooling, preventing the apex of the probe from crushing or getting away from the sample surface over a long period of time. **Figure 9** shows images of a polyester-based compound resinous film, sequentially obtained using probe auto tracking. Topographic and phase images were acquired through temperature variations where the sample was heated in steps of 1°C per minute.

No change is seen in the topographic image, but significant changes are detected in the phase images of the surface. The phase images reveal the change of the sample state, which becomes uniform by heating.

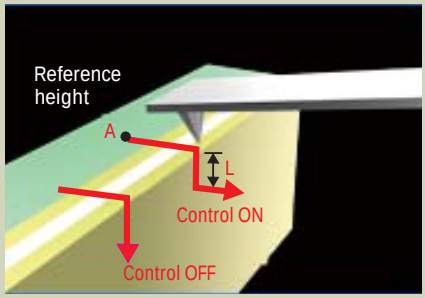

Fig. 6 Schematic diagram of the principle of damage-less scan control.

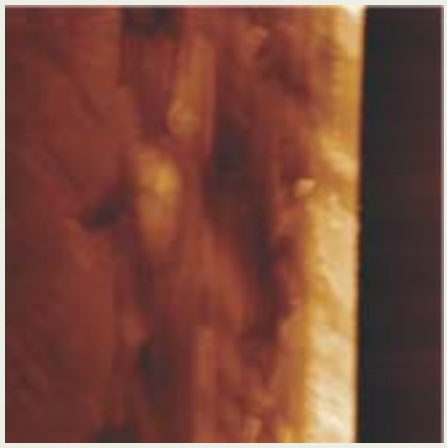

Fig. 7 AFM image of a cross section of a multi-layer optical film.
(scan size : 4 μm × 4 μm)

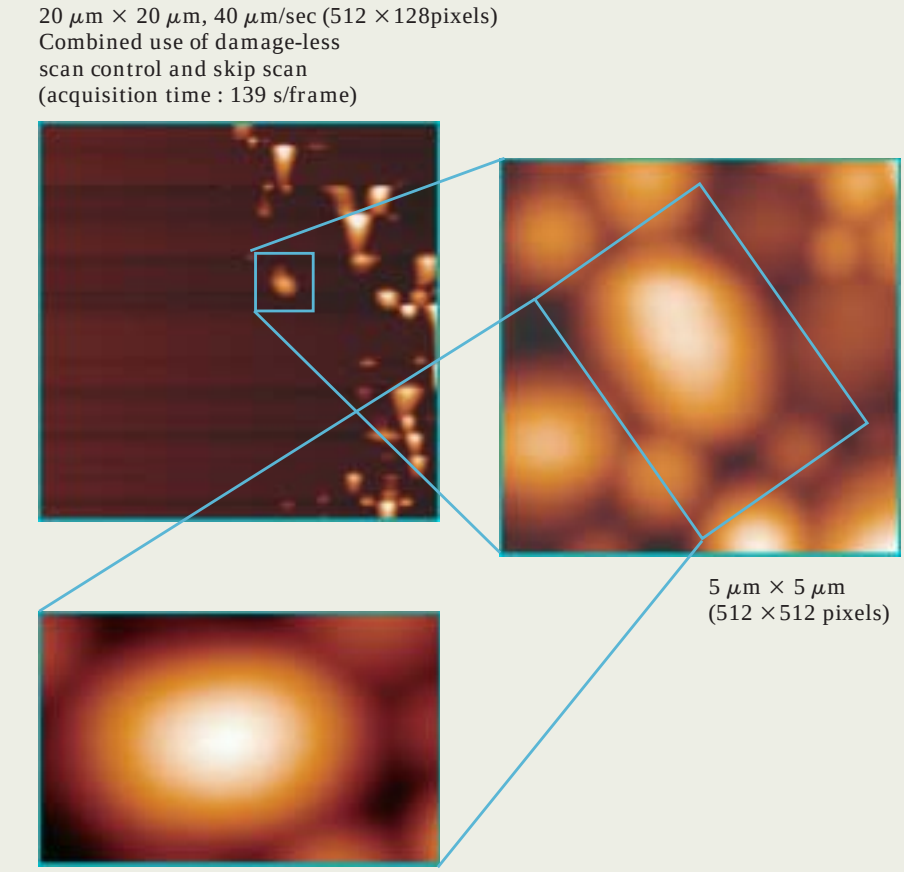

Fig. 8 Topographic images of glue.

●Digital zoom

Up to 2048× 2048 pixels are provided for images, allowing images to be simultaneously displayed for up to 5 channels.

Figure 10 shows phase images of a two-component wax mixture, which are displayed with maximum pixels. Since the phase image contains information on physical properties of materials, it is frequently utilized simultaneously with the topographic image. From images acquired with maximum pixels, we can easily pick up enlarged images on areas of interest in digital zoom.

Summary

This paper has introduced the JSPM-5400, which achieves flexible environmental control, high-resolution imaging and ease of use. This versatile environmental SPM is especially suited for high-resolution observations of polymer samples, which will give deeper insights for various fields including the development of new products.

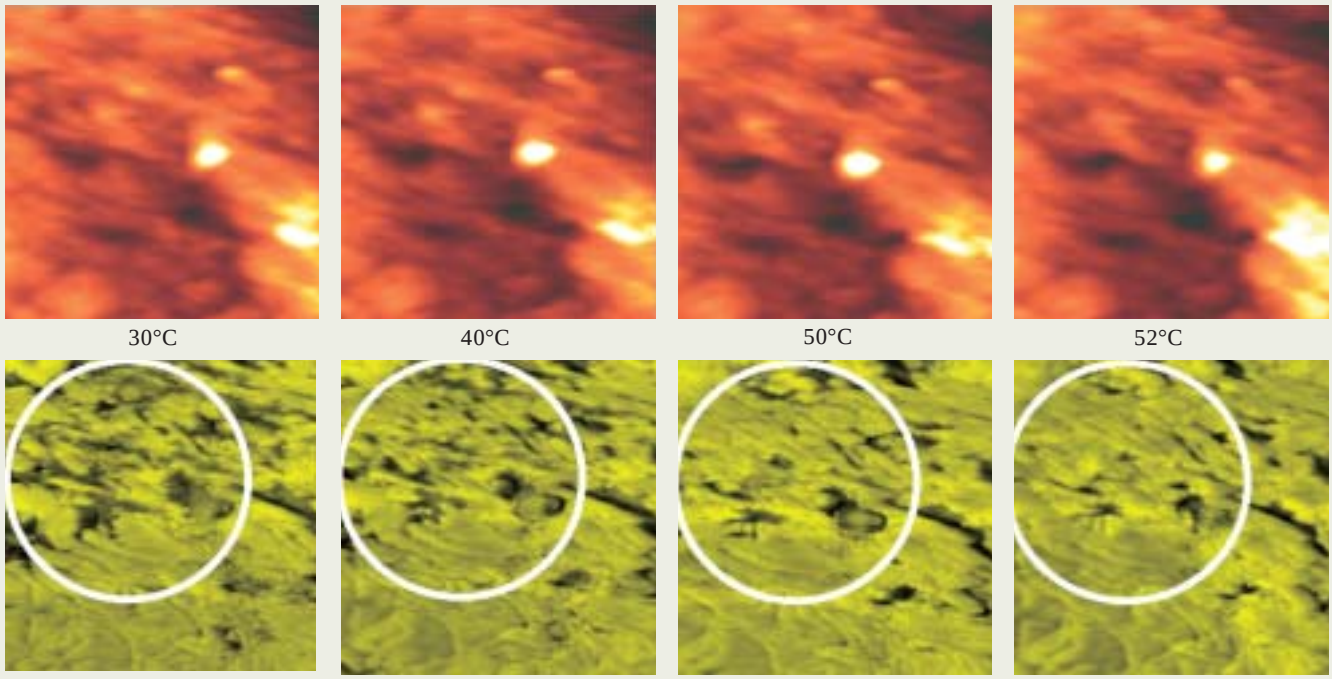

Fig. 9 Topographic images (upper) and phase images (lower) of a polyester-based compound resinous film through temperature variations (scan size : 2 μm × 2 μm).

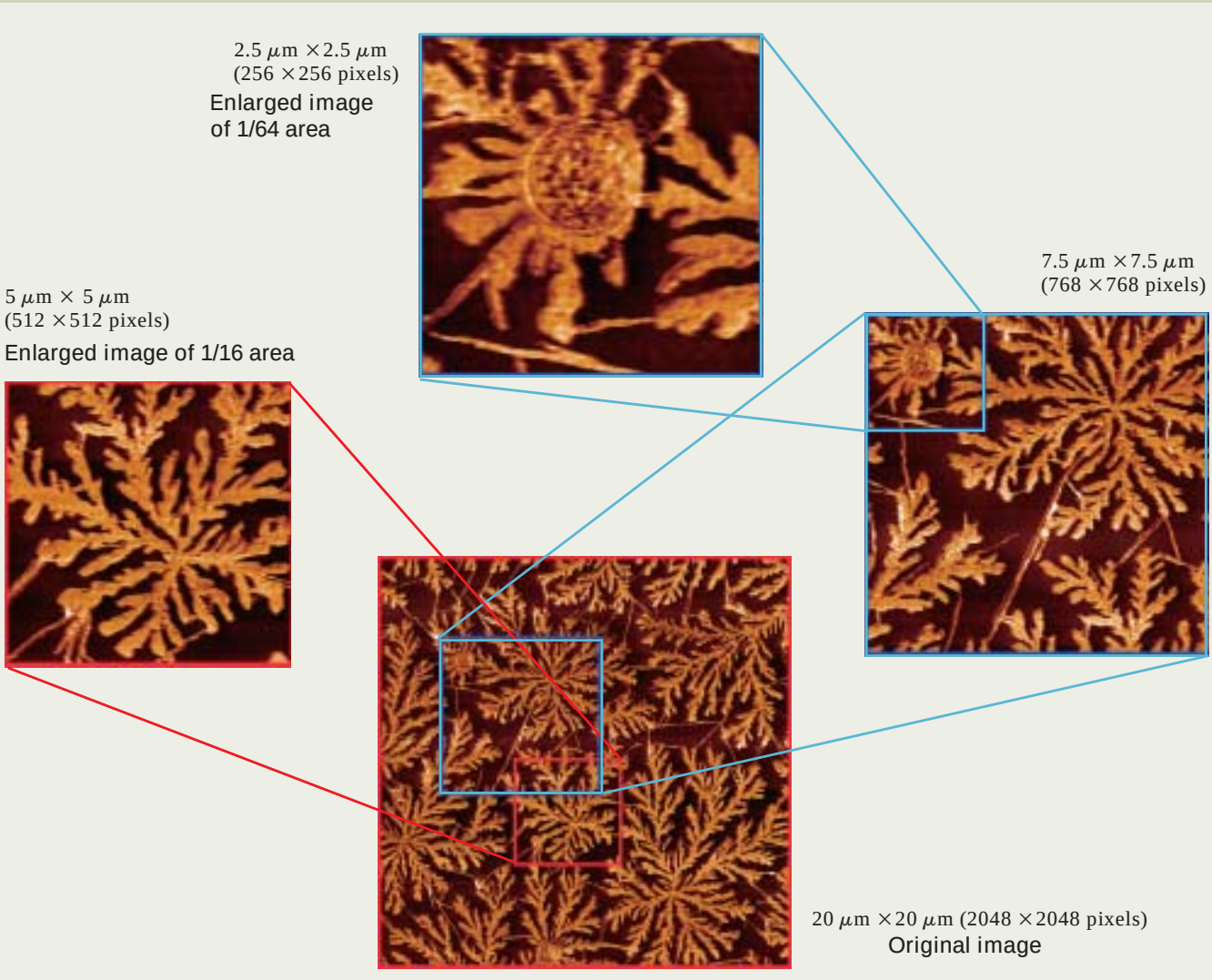

Fig. 10 Phase images of a two-component wax mixture.

Field Emission Electron Microscope
JEM-3100F

For evaluation of materials in the fields of nanoscience and nanomaterials science, TEM is required to provide resolution and analytical capabilities that can directly distinguish atoms.
The JEM-3100F, a superb analytical TEM, can achieve sub-nanometer resolution for structural and compositional analyses. Its sophisticated electron optical system allows a clear image with 0.1 nm resolution to be obtained. In addition, its improved mechanical and electrical stability provides a stable electron beam for a 0.14 nm probe. These features make the JEM-3100F a suitable tool for analyzing materials at the atomic and molecular level.

Main performance (in UHR configuration)

- Accelerating voltage — Up to 300 kV
- Electron gun — ZrO/W (100) Schottky emitter
- TEM resolution — 0.17 nm
- STEM resolution — 0.14 nm
- Probe current — 0.5 nA at 1 nm-probe
- Specimen tilt angle — ±25°

Information limit

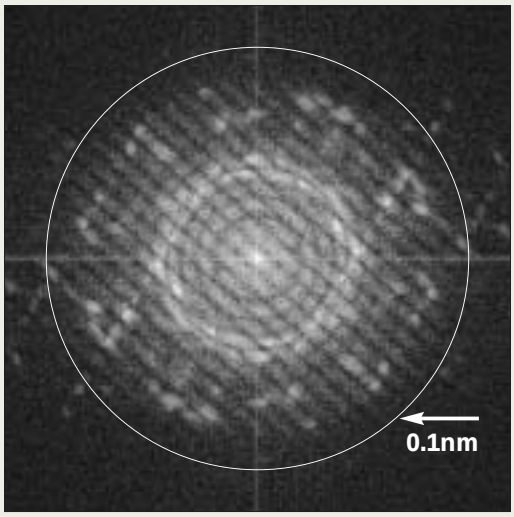

Young fringe pattern taken from a TEM image of an amorphous Ge foil with Au particles. The circle indicates a 0.1 nm resolution line. This pattern verifies an information limit better than 0.1 nm.

High-resolution STEM-HAADF image

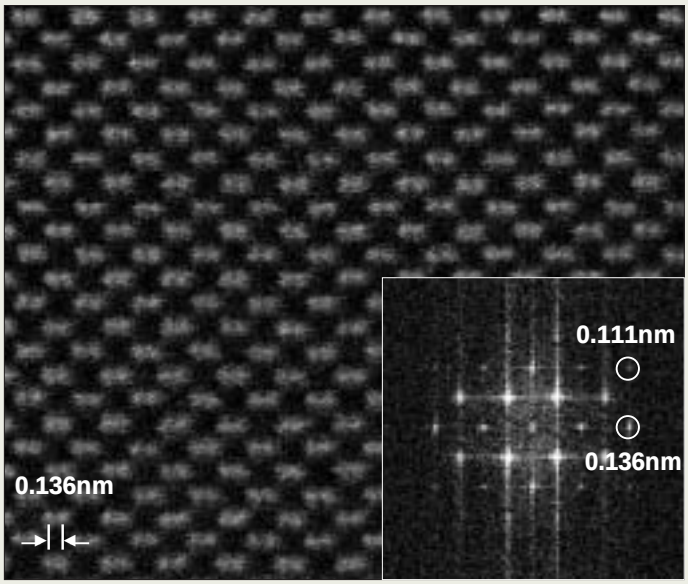

STEM-HAADF image of a Si [110] single crystal. An atomic spacing of for the (400) plane of Si is clearly resolved, together with a FFT pattern containing a spot corresponding to an atomic spacing of 0.111 nm. This indicates that a probe diameter less than 0.111 nm can be obtained with the JEM-3100F.

Electron Microscope
JEM-1400

The JEM-1400 is a 120 kV TEM that provides outstanding results for beginners and experts alike.

Electron optical system for high contrast
An electron optical system that provides high-contrast TEM images is essential in all medical and biological investigations. The JEM-1400 incorporates newly designed objective lenses for high-contrast, high-resolution imaging.

Computer-controlled high-performance goniometer stage
The JEM-1400 features a high-performance, side-entry goniometer stage with 5-axis computer-control (X, Y, Z, and Tilt X and Tilt Y). A new piezoelectric drive system provides the ultimate in accuracy and performance. This stage automatically sets the minimum stage movement steps for each magnification. In addition, the eucentric stage has a high-tilt capability, optimized for tomography.

Digital CCD camera
The JEM-1400 is designed on the concept, "unity of camera and column". A newly developed special-purpose digital CCD camera, optimized for the JEM-1400, is integrated through the TEM Center GUI. Images acquired with this CCD camera are directly stored in digital format.

Efficient operation environment utilizing advanced techniques (TEM Center)
The **TEM Center** framework, developed for an efficient operation environment for the JEM-1400, fully utilizes advanced Windows techniques. Digital-camera TEM images appear in the **TEM Center** GUI screens. The screens for routine operations are compactly arranged, enabling beginners to use the software easily. Furthermore, expert operators can use sophisticated GUI screens that facilitate direct control of the main elements of the TEM, such as lenses and deflector coils.

TEM Navigation system Jenie
The JEM-1400 incorporates a TEM Navigation System, *Jenie* (JEOL Electron microscope Navigation Interactive Engine). The operator can learn the procedure for operating the instrument while viewing easy-to-understand videos.
Jenie offers special operating procedures for tasks such as axis alignment after replacing the electron-gun filament, as well as for routine operation. Thus, *Jenie* is useful for not only beginners but also administrators. In addition, *Jenie* enables the operator to add and edit procedures, making it possible to customize a navigation file for each user, as an education program or a routine data collection sequence.

A unified GUI, a wealth of optional accessories
The control system of the JEM-1400 is the same as those of JEOL's performance-winning 200 kV TEMs: JEM-2100, JEM-2100F, JEM-2200FS. A wealth of optional accessories, including STEM, an EDS system, TEM Tomography software, cryo-blades and a variety of specimen holders, are available.

Integrated Framework TEM Center

TEM Navigation System Jenie

Introduction of New Products

Ultra High Resolution FE SEM
JSM-7500F/JSM-7500FA

The JSM-7500F is an ultra high resolution FE SEM, which has been developed to satisfy the most demanding researchers in nano technology and related research fields. The SEM is equipped with the high brightness conical FE gun and the low aberration conical semi in-lens objective lens. The improved overall stability of the JSM-7500F enables you to readily observe your specimen at magnifications up to 1,000,000x with the guaranteed resolution of 1 nm at 15 kV. The guaranteed resolution at 1 kV is 1.4 nm. The extremely low electron energy of as low as 0.1 keV can be utilized to reveal fine surface structures of a specimen. The specimen chamber is large enough to accommodate a 200 mm diameter specimen. The unique one action specimen exchange airlock chamber lets you introduce a specimen quickly without breaking the high vacuum in the specimen chamber. The specimen stage has all five axes motorized and controlled by the PC for comfortable and efficient operation. The specimen chamber is pumped by the TMP with the magnetic bearing in order to keep the clean environment in the specimen chamber.

Glass (no coating) ***0.1 kV***

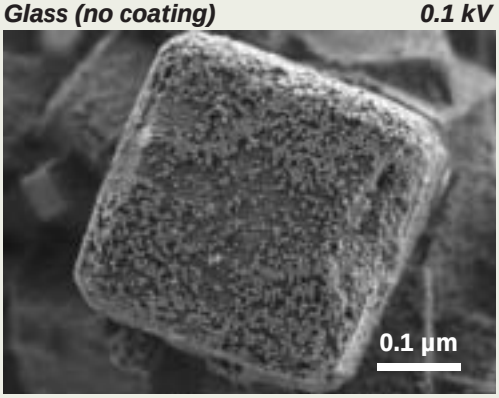

The JSM-7500FA is the ultra high resolution analytical FE SEM with the JEOL EDS embedded. The operation GUI has the buttons to change the operation mode quickly from the observation mode to the elemental analysis mode. The JSM-7500FA allows a quick start of elemental analysis on the SEM image showing fine surface structures. The user-friendly operation GUI displays the SEM image and the elemental analysis results on the same monitor. The specimen chamber is provided with many accessory ports to accept a variety of detectors including the EBSD for crystal orientation analysis.

Ultra High Resolution FE SEM
JSM-6701F

The JSM-6701F is the ultra high resolution FE SEM suitable for observation of fine structures such as multi-layered structures and nano particles. The SEM has the guaranteed resolution of 1 nm at 15 kV and 2.2 nm at 1 kV. The lower electron energies are effective in observation of fine surface structures. The electron optics is completely automated so that the electron energy and the probe current can be changed and the observation condition can be optimized quickly to suit for a variety of specimens. The specimen chamber is large enough to accommodate a 200 mm diameter specimen. The unique one action specimen exchange airlock chamber lets you introduce a specimen quickly. The specimen stage has X, Y, and rotation axes motorized and controlled by the PC for comfortable and efficient operation. The unique aperture angle optimizing lens lets you use the maximum probe current of 2 nA even at a very high magnification. The higher probe current is effective for the elemental analysis with the optional EDS.

Introduction of New Products

High-Performance General-Purpose SEM with a large specimen chamber

JSM-6490 series

The JSM-6490 series SEM is a flexible multi-purpose SEM. Multiple users can customize the operation GUI for efficient operations with optimum performance. The well-accepted user-friendly GUI has been upgraded to be more compatible with the multiple user environment. A unique addition is SmileShot, which sets the SEM for the optimum conditions by simply selecting the conditions of a specimen. In addition, JEOL has added new features: multiple live image display, signal mixing, full-screen live image and movies (AVI files).
The large specimen chamber and the five-axis motor controlled specimen stage with large movements can readily handle a large variety of specimens. The JSM-6490LV, which has a low vacuum mode built-in, can observe and analyze non-conductive specimens without any conductive coating.
The JSM-6490A and JSM-6490LA are the analytical scanning electron microscopes with a JEOL EDS elemental analyzer embedded. These compact SEM systems offer comfortable seamless operation from observation to elemental analysis.

- Resolution: 3.0 nm (HV mode), 4.0 nm (LV mode)
- Accelerating voltage: 0.3 to 30 kV (56 steps)
- Magnification: × 5 to 300,000
- Specimen size: Up to 203 mm diameter
- Specimen stage: X=125 mm, Y=100 mm, Z=5 to 80 mm
  T=–10 to 90°, R=360°

Yogurt bacteria ***3 kV***

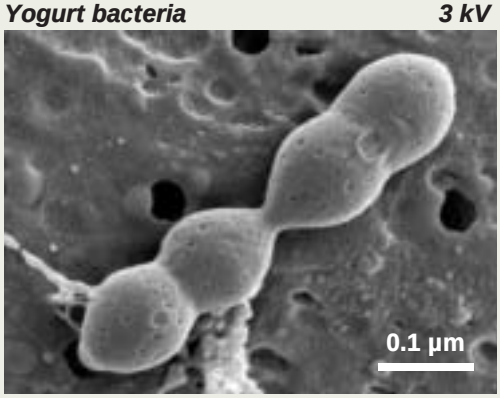

High-Performance General-Purpose SEM

JSM-6390 series

The JSM-6390 series SEM is a user-friendly high-performance general-purpose scanning electron microscope composed of the fully automated high-performance electron optics and the newly developed multi-user compatible operation software with the new features, live image display, signal mixing, full-screen live image and movies (AVI files). The JSM-6390LV, which has the low vacuum mode built-in, can observe and analyze non-conductive specimens without any conductive coating. The JSM-6390A and JSM-6390LA are the analytical scanning electron microscopes with a JEOL EDS elemental analyzer embedded. These compact SEM systems offer comfortable seamless operation from observation to elemental analysis.

- Resolution: 3.0 nm (HV mode), 4.0 nm (LV mode)
- Accelerating voltage: 0.5 to 30 kV (53 steps)
- Magnification: × 5 to 300,000
- Specimen size: Up to 150 mm diameter
- Specimen stage: X=80 mm, Y=40 mm, Z=5 to 48 mm
  T=–10 to 90°, R=360°

High-Performance Single-Beam FIB with a large ion-beam current

JEM-9320FIB

The JEM-9320FIB is the latest high-performance single-beam FIB with the high-speed milling, high resolution, and high beam current in a simple, compact design. This FIB can prepare thin-film from local areas of STEM/TEM specimens and achieves precise, fast milling for SEM cross section specimens.

High-speed, high-precision milling, high-resolution observation

High-speed milling with a large ion-beam current (at 30 kV, 30 nA or larger) reduces the rough-milling time significantly.
The improved ion optical system enables one to observe a high-resolution SIM image (6 nm, 30 kV).

Space-saving, energy-saving

The JEM-9320FIB can be installed even in a space smaller than 3 m × 3 m because of its small footprint.
The JEM-9320FIB has an energy-saving (beam-saver) mode to reduce power consumption.

Twin stage

The JEM-9320FIB can be equipped with a side-entry goniometer stage and a bulk specimen eucentric stage at same time or with just one stage to meet to your applications.

Improved GUI

The JEM-9320FIB has an improved graphical user interface with new functions for easy operation and stable processing.

Automatic processing software (optional)

Automatic processing software enables one to preprocess STEM/TEM specimens and SEM cross section specimens automatically.
This software continuously processes multiple points while automatically correcting the beam positions. Its recipe allows automatic processing up to 300 points with a maximum processing width of 100 µm.

● Ion source	Ga liquid metal ion source
● Accelerating voltage	5 to 30 kV (in 5 kV steps)
● Magnification	× 50 (field search), × 150 to 300,000
● Image resolution	6 nm (at 30 kV)
● Maximum beam current	30 nA (at 30 kV)
● Specimen size	28 mm diameter (13 mm thick) 50 mm diameter (2 mm thick)

Side-entry goniometer stage

Bulk specimen eucentric stage

Electron Beam Lithography System

JBX-6300FS

The JBX-6300FS is a Spot-type Electron Beam Lithography System, which can meet a wide range of needs for research, prototype manufacturing and production, including nano-molecular devices, photonic crystal devices, quantum-effect devices, optical devices, communication devices and MEMS devices.

- A thermal field emission electron gun enables the accelerating voltage to be selected and switched from 100 kV, 50 kV and 25 kV.
- Its electron optical system produces a small probe down to 2 nm in diameter at the maximum accelerating voltage of 100 kV, calculated with optical simulation. In addition, the JBX-6300FS employs a 19 bit DAC for beam positioning that allows high-precision lithography, achieving a minimum line width of 8 nm (at the center of lithography fields).
- The step-and-repeat method is used for stage movement. The stage position is controlled by the measurement of a laser interferometer with a reading accuracy of 0.62 nm. Thus, the JBX-6300FS achieves high field-stitching accuracy and high overlay accuracy.
- A workstation running under a UNIX operating system is used as a calculation system. Combined use of this workstation with GUI (graphical user interface) provides high operability.

Main Specifications

Electron gun emitter	ZrO/W TFE
Accelerating voltage	100 / 50 / 25 kV
Minimum beam diameter	2 nm [1]
Scanning type	Vector scanning
Beam-positioning DAC	19 bits
Beam-scanning DAC	12 bits
Beam-scanning speed	Up to 12 MHz
Laser resolution	0.62 nm (λ/1024)
Field size	2000 µm, 1000 µm, 500 µm, 250 µm, 125 µm, 62.5 µm squares
Field-stitching accuracy	±25 nm
Overlay accuracy	±20 nm
Workpiece dimension	Up to 200 mm in diameter

[1]: Calculated with optical simulation.

Examples of Lithography Patterns

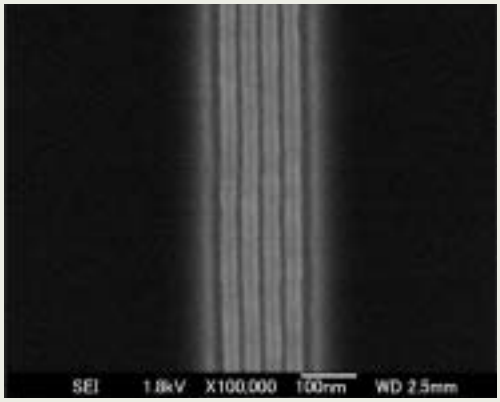

Line and space Line: 8 nm, Pitch: 40 nm

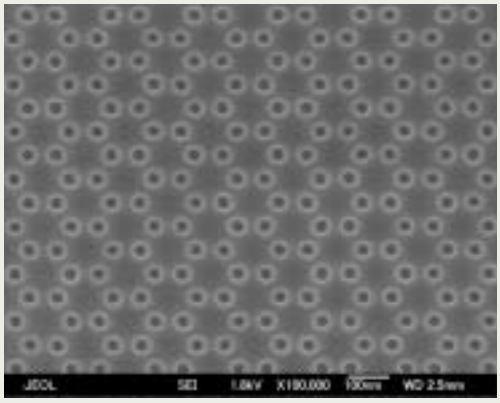

Photonic Dot: 30 nm, Pitch: 70 nm

JEOL ISO 9001 & ISO 14001 Certificated

Certain products in this brochure are controlled under the "Foreign Exchange and Foreign Trade Law" of Japan in compliance with international security export control. JEOL Ltd. must provide the Japanese Government with "End-user's Statement of Assurance" and "End-use Certificate" in order to obtain the export license needed for export from Japan. If the product to be exported is in this category, the end user will be asked to fill in these certificate forms.

http://www.jeol.com/

JEOL JEOL Ltd. 1-2 Musashino 3-chome Akishima Tokyo 196-8558 Japan Sales Division ☎(042)528-3381 FAX(042)528-3386

ARGENTINA
COASIN S. A. C. I. yF.

Virrey del Pino 4071, 1430 Buenos Aires, Argentina
Telephone: 54-11-4552-3185
Facsimile: 54-11-4555-3321

AUSTRALIA & NEW ZEALAND
JEOL (AUSTRALASIA) Pty. Ltd.

Unit 9/750-752 Pittwater Road
Brookvale, NSW 2100, Australia
Telephone: 61-2-9905-8255
Facsimile: 61-2-9905-8286

AUSTRIA
LABCO GmbH

Dr.-Tritremmel-Gasse 8, A-3013 Pressbaum, Austria
Telephone: 43-2233-53838
Facsimile: 43-2233-53176

BANGLADESH
A.Q. CHOWDHURY & CO. PVT. Ltd.

Baridhara Central Plaza 87, Suhrawardy Avenue
2nd Floor Baridhara, Dhaka-1212 Bangradesh
Telephone: 880-2-9862272, 9894533
Facsimile: 880-2-8854428

BELGIUM
JEOL (EUROPE) B. V.

Planet II, Building B Leuvensesteenweg 542,
B-1930 Zaventem, Belgium
Telephone: 32-2-720-0560
Facsimile: 32-2-720-6134

BRAZIL
FUGIWARA ENTERPRISES
INSTRUMENTOS CIENTIFICOS LTDA.

Avenida Itaberaba,3563
02739-000 Sao Paulo, SPI Brazil
Telephone: 55-11-3983-8144
Facsimile: 55-11-3983-8140

CANADA
JEOL CANADA, INC.
(Represented by Soquelec, Ltd.)

5757 Cavendish Boulevard, Suite 540,
Montreal, Quebec H4W 2W8, Canada
Telephone: 1-514-482-6427
Facsimile: 1-514-482-1929

CHILE
TECSIS LTDA.

Avenida Holanda 1248,
Casilla 50/9 Correo 9, Providencia, Santiago, Chile
Telephone: 56-2-205-1313
Facsimile: 56-2-225-0759

CHINA
JEOL LTD., Beijing Office

Room B2308A, Vantone New World Plaza, No. 2 Fuwai Street, Xicheng District,Beijing, 100037, P.R. China
Telephone: 86-10-68046321/6322/6323
Facsimile: 86-10-68046324

JEOL LTD., Shanghai Office

11 F2, Sanhe Building, No. 121 Yan Ping Road,
Shanghai 200042, P.R. China
Telephone: 86-21-62462353, 55
Facsimile: 86-21-62462836

JEOL LTD., Guangzhou Office

S2204, World Trade Center Building 371-375, Huan Shi East-Road, Guangzhou, 510095 P.R. China
Telephone: 86-20-87787848/87618986
Facsimile: 86-20-8778-4268

JEOL LTD., Wuhan Office

Room 3216, World Trading Bldg., 686 Jiefang Street,
Hankou, Wuhan, Hubei 430032 P.R. China
Telephone: 86-27-85448953
Facsimile: 86-27-85448695

JEOL LTD., Chengdu Office

1807A Zongfu Bld., No. 45 Zhongfu Road Chengdu,
Sichuan, P. R. China
Telephone: 86-28-86622554
Facsimile: 86-28-86622564

FARMING LTD.

Unit 1009, 10/F., MLC Millennia Plaza,
663 King's Road, North Point, Hong Kong
Telephone: 852-281-57299
Facsimile: 852-2581-4635

CYPRUS
MESLO LTD.

Scientific & Laboraty Division,
P. O. Box 27709, Nicosia Cyprus
Telephone: 357-2-666070
Facsimile: 357-2-660355

EGYPT
JEOL SERVICE BUREAU

3rd Fl. Nile Center Bldg.,
Nawal Street, Dokki, (Cairo), Egypt
Telephone: 20-2-335-7220
Facsimile: 20-2-338-4186

FRANCE
JEOL (EUROPE) SAS

Espace Claude Monet, 1 Allee de Giverny 78290
Croissy-sur-Seine, France
Telephone: 33-13015-3737
Facsimile: 33-13015-3747

GERMANY
JEOL (GERMANY) GmbH

Oskar-Von-Miller-Strasse 1, 85386 Eching Germany
Telephone: 49-8165-77346
Facsimile: 49-8165-77512

GREAT BRITAIN & IRELAND
JEOL (U.K.) LTD.

JEOL House, Silver Court, Watchmead,
Welwyn, Garden City, Herts AL7 1LT., U. K.
Telephone: 44-1707-377117
Facsimile: 44-1707-373254

GREECE
N. ASTERIADIS S. A.

56-58, S. Trikoupi Str. P.O.Box 26140
GR-10022 Athens, Greece
Telephone: 30-1-823-5383
Facsimile: 30-1-823-9567

INDIA
Blue Star LTD. (HQ)
Analytical Instruments Department

'Sahas'414/2 Veer Savarkar Marg,
Prabhadery Mumbai 400 025, India
Telephone: 91-22-5666-4068
Facsimile: 91-22-5666-4001

Blue Star LTD. (Haryana Delhi)
Analytical Instruments Department

E-44/12 Okhla Industrial Area,
Phase-11, New Delhi 110 020, India
Telephone: 91-11-5149-4000
Facsimile: 91-11-5149-4004

Blue Star LTD. (Calcutta)
Analytical Instruments Department

7, Hare Street Calcutta 700 001, India
Telephone: 91-33-2213-4000
Facsimile: 91-33-2213-4102/4103

Blue Star LTD. (Chennai)
Analytical Instruments Department

Garuda Building, Cathedral Road
Chennai 600 086, India
Telephone: 91-44-5244-7210
Facsimile: 91-44-5244-4190

INDONESIA
PT. TEKNOLABindo Penta Perkasa

J1. Gading BukitRaya,
Komplek Gading Bukit Indah Blok I/11,
Kelapa Gading Jakarta 14240, Indonesia
Telephone: 62-21-45847057/58/59
Facsimile: 62-21)-45842729

ITALY
JEOL (ITALIA) S.p.A.

Centro Direzionale Green Office Via Dei Tulipani,
1, 20090 Pieve, Emanuele (MI), Italy
Telephone: 39-2-9041431
Facsimile: 39-2-90414353

KOREA
JEOL KOREA LTD.

Sunmin Bldg. 6th F1.,218-16, Nonhyun-Dong,
Kangnam-Ku, Seoul, 135-010, Korea
Telephone: 82-2-511-5501
Facsimile: 82-2-511-2635

KUWAIT
YUSUF I. AL-GHANIM & CO. (YIACO)

P. O. Box 435, 13005 - Safat, Kuwait
Telephone: 965-4832600/4814358
Facsimile: 965-4844954/4833612

MALAYSIA
JEOL (MALAYSIA) SDN. BHD. (359011-M)

205, Block A, Mezzanine Floor, Kelana Business Center97,
Jalan SS 7/2, Kelana Jaya,
47301 Petaling Jaya, Selangor, Malaysia
Telephone: 60-3-7492-7722
Facsimile: 60-3-7492-7723

MEXICO
JEOL DE MEXICO S.A. DE C.V.

Av. Amsterdam #46 DEPS. 402
Col. Hipodromo, 06100 Mexico D.F. Mexico
Telephone: 52-5-55-211-4511
Facsimile: 52-5-55-211-0720

PAKISTAN
Analytical Measuring System (Pvt.) Limited. AMS House

AMS House Plot # 14C, Main Sehar Commercial Avenue,
Commercial Lane 4 Khayaban-Sehar, D. H. A Phase 7
Karachi, Pakistan
Telephone: 92-21-5345581/5340747
Facsimile: 92-21-5345582

PANAMA
PROMED S.A.

Parque Industrial Costa del Este Urbanizacion Costa del

Este Apartado 6281, Panama, Panama
Telephone: 507-269-0044
Facsimile: 507-263-5622

PHILIPPINES
PHILAB INDUSTRIES, INC.

7487 Bagtikan Street, SAV Makati, 1203 Metro,
Manila Philippines
Telephone: 63-2-896-7218
Facsimile: 63-2-897-7732

PORTUGAL
Izasa. Portugal Lda.

R. do Proletariado 1, 2790-138 CARNAXIDE Portugal
Telephone: 351-21-424-7300
Facsimile: 351-21-418-6020

RUSSIA
JEOL LTD Moscow Office

Prospect Mira 72,418 Moscow 129119, Russia
Telephone: 7-495-641-11-14
Facsimile: 7-495-641-28-63

SAUDI ARABIA
ABDULREHMAN ALGOSAIBI G. T.B.

Algosaibi Bldg., Airport Rd., P. O. Box 215,
Riyadh 11411, Saudi Arabia
Telephone: 966-1-479-3000
Facsimile: 966-1-477-1374

SCANDINAVIA
JEOL (SKANDINAVISKA) A.B.

Hammarbacken 6 A, Box 716, 191 27 Sollentuna, Sweden
Telephone: 46-8-28-2800
Facsimile: 46-8-29-1647

SERVICE & INFORMATION OFFICE
JEOL NORWAY

Ole Deviks vei 28, N-0614 Oslo, Norway
Telephone: 47-2-2-64-7930
Facsimile: 47-2-2-65-0619

JEOL FINLAND

Ylakaupinkuja 2, FIN-02360 Espoo, Finland
Telephone: 358-9-8129-0350
Facsimile: 358-9-8129-0351

JEOL DENMARK

Naverland 2, DK-2600 Glostrup, Denmak
Telephone: 45-4345-3434
Facsimile: 45-4345-3433

SINGAPORE
JEOL ASIA PTE. LTD.

29 International Business Park,
#04-02A Acer Building,
Tower B Singapore 609923
Telephone: 65-6565-9989
Facsimile: 65-6565-7552

SOUTH AFRICA
ADI Scientific (Pty) Ltd.

109 Blandford Road, North Riding,Randburg
(PO box 71295 Bryanston 2021)
Republic of South Africa
Telephone: 27-11-462-1363
Facsimile: 27-11-462-1466

SPAIN
IZASA. S.A.

Aragoneses, 13,
28100 Alcobendas,
(Polígono Industrial) Madrid, Spain
Telephone: 34-91-663-0500
Facsimile: 34-91-663-0545

SWITZERLAND
JEOL(GERMANY)GmbH

Oskar-Von-Miller Strasse 1,
85386 Eching Germany
Telephone: 49-8165-77346
Facsimile: 49-8165-77512

TAIWAN
JIE DONG CO., LTD.

7th, F1, 112, Chung Hsiao East Road, Section 1,
Taipei, Taiwan 10023, Republic of China
Telephone: 886-2-2395-2978
Facsimile: 886-2-2322-4655

JEOL TAIWAN SEMICONDUCTORS LTD.

11F, No. 346, Pei-Ta Road, Hsin-Chu City 300,
Taiwan Republic of China
Telephone: 886-3-523-8490
Facsimile: 886-2-523-8503

THAILAND
BECTHAI BANGKOK EQUIPMENT
& CHEMICAL CO., LTD.

300 Phaholyothin Rd. Phayathai,
Bangkok 10400, Thailand
Telephone: 66-2-615-2929
Facsimile: 66-2-615-2350/2351

THE NETHERLANDS
JEOL (EUROPE) B.V.

Lireweg 4, NL-2153 PH Nieuw-Vennep,
The Netherlands
Telephone: 31-252-623500
Facsimile: 31-252-623501

TURKEY
TEKSER LTD. STI.

Acibadem Cad. Erdem Sok. Baver Art. 6/1
34660 Uskudar/Istanbul-Turkey
Telephone: 90-216-3274041
Facsimile: 90-216-3274046

UAE
Business Communications LLC.

P. O. Box 233, Dubai UAE
Telephone: 971-4-2220186
Facsimile: 971-4-22236193

USA
JEOL USA, INC.

11 Dearborn Road, Peabody, MA. 01960, U. S. A.
Telephone: 1-978-535-5900
Facsimile: 1-978-536-2205/2206

JEO USA, INC. WEST OFFICE

5653 Stoneridge Drive Suite
#110 Pleasanton, CA. 94588 U. S. A.
Tel: 1-925-737-1740
Fax: 1-925-737-1749

VENEZUELA
MITSUBISHI VENEZOLANA C. A.

Avenida Francisco de Miranda Edificio Parque Canaima,
Piso 2 Los Palos Grandes, Caracas, Venezuela
Telephone: 58-212-209-7402
Facsimile: 58-212-209-7496

VIETNAM
TECHNICAL MATERIALS AND RESOURCES
IMPORT-EXPORT COMPANY (REXCO)
HANOI BRANCH

157 Lang Ha Road, Hanoi, Vietnam
Telephone: 84-4-562-0516
Facsimile: 84-4-853-2511

(Ser. No. 124)

No. 01001G637A Printed in Japan, Kp